NASA

Technical Memorandum 82056

Submillimeter Wave Survey of the Galactic Plane

L. H. Cheung

DECEMBER 1980

National Aeronautics and
Space Administration

Goddard Space Flight Center
Greenbelt, Maryland 20771

SUBMILLIMETER WAVE SURVEY OF THE GALACTIC PLANE

Lim Hung Cheung

Submitted in partial fulfillment of
the requirements for the
Degree of Doctor of Philosophy
in the Department of Physics and Astronomy
University of Maryland

1980

Submillimeter Wave Survey of the Galactic Plane

Lim Hung Cheung
Department of Physics and Astronomy
University of Maryland

ABSTRACT

This thesis presents the technical development and the first scientific results of a systematic survey of the Galactic plane ($|b| < 3°$) in three submillimeter continuum wavelength bands. The primary objective of the survey is to measure over virtually the entire Galactic plane the distribution and basic physical conditions of the coolest dust component of the interstellar medium. The instrument, designed for observations of extended, low surface brightness continuum emission, consists of a balloon-borne, gyro-stablized, 1.2-meter Cassegrain telescope and a liquid-helium cooled photometer with short wavelength limits of 100, 230, and 270 μm. The first two flights of the system yielded 10 arcmin resolution maps of about half of the Galactic plane region extending to ± 3 degrees in latitude, as well as fields totaling 300 square degrees around the Orion/Rosette molecular cloud complex, the L134 and Ophiuchus dark clouds. The design, integration, tests and flight operation of the survey observatory are presented, together with a discussion of the data analysis technique. Photometric maps of the submillimeter wave emission from the Galactic plane region between $\ell = 8°$ to $\ell = 44°$ in three wavelength bands are analyzed and compared with observations at other wavelengths. The results have contributed new information both on a list of specific interstellar clouds and on the distribution of mass and luminosity on a Galactic scale.

ACKNOWLEDGMENTS

It is a pleasure to thank my advisors, Drs. Frank McDonald and Michael Hauser, for their hospitality and for providing the opportunity for my research at Goddard Space Flight Center. Dr. McDonald had the foresight in initiating this low energy program within his high energy astrophysics laboratory. I am grateful to Dr. Michael Hauser not only for his guidance in this thesis project, but also for his support in other areas including the 1.0-mm observation program at CTIO and NASA IRTF.

I thank my collaborators, Drs. Daniel Gezari, Tom Kelsall, John Mather, and Robert Silverberg, who contributed their individual expertise in various aspects leading to the flawless performance of the instrument in the first flight. This thesis would have been more difficult if the balloon flight had not been so successful. I also thank Dr. Mark Stier who provided and modified part of the data processing software used in this thesis.

I am grateful to Professors Frank Kerr, Glenn Mason, Frank McDonald, David Zipoy, Ben Zuckerman, and Dr. Floyd Stecker for their valuable comments and suggestions on the first draft of this thesis. I am particularly thankful to Professor Frank Kerr, Drs. Michael Hauser, Tom Kelsall, and Robert Silverberg for carefully reading the manuscript and pointing out many errors in the text.

My thanks also go to Drs. Richard Cohen, Tom Dame, and Patrick Thaddeus of Columbia University for providing the pre-published data of their CO survey. I benefited much from discussions of CO observations with Dr. Gordon Chin, who also generously afforded me access to his versatile micro-computer system.

The engineering and technical personnel at Goddard Space Flight Center contributed much to the development of the instrument. In particular, I acknowledge the valuable help from Tony Flanick, David Walser, Jesse Smith, Tom Skillman, and Alan Silver. I also thank Jim Heaney for his help with the Nicolet spectrometer. The personnel at the National Scientific Balloon Facility in Palestine, Texas contributed their valuable expertise in the launch and recovery of the survey instrument. They have also provided us with an excellent working environment during the final preparation of the observatory.

Last but not least, I am grateful to members of my family for their constant encouragement. In particular, I am indebted to my sister, Suk-ming, for her unselfish support during an earlier phase of my education, and to my wife, Carol, for putting up with me during the time when this thesis was being written.

TABLE OF CONTENTS

CHAPTER 1 INTRODUCTION

1.1 GENERAL BACKGROUND

Cosmic infrared radiation and the relative paucity of stars in certain directions in the sky were observed at least as early as the eighteenth century by F. W. Herschel. It was not until the last few decades that these two phenomena were studied in more detail, with important contributions to our understanding of the interstellar medium and our Galaxy. Careful photographic observations beginning about 50 years ago, notably by E. E. Barnard, have produced evidence that the paucity of stars in some directions is due to extinction by intervening dust and not to a real deficiency in stellar population. Because of dust obscuration, the overall appearance of our Galaxy was largely unknown, although many external galaxies were observed to possess regular spiral structures. The advances in radio astronomy beginning 30 years ago have since enabled us to see through the dust obscuration, obtaining observational information of gaseous processes in the inner and far side of the Galaxy. Only in the last ten years have we been able to observe the relatively cool interstellar dust directly in emission at far infrared and submillimeter wavelengths. This opens up a new observational window for

probing the distribution and physical conditions of an important ingredient of the Galaxy.

Interstellar dust, although constituting only a minor fraction (≈ 1 %) by mass, plays a highly significant role in affecting the physical and chemical properties of the interstellar medium. A collection of dust grains, with relatively large absorption cross section, efficiently absorbs short wavelength, energetic photons and re-radiates the energy at long infrared wavelengths. This process undoubtedly has a fundemental influence on the radiation field in the diffuse interstellar medium and in the immediate vicinity of luminous objects, with important effects on the cooling of dense clouds from which stars are formed. It now appears well established that molecular hydrogen, the most abundant molecule in the Galaxy, forms on dust grain surfaces and is protected from photo-dissociation inside high opacity clouds. Dust emission at long infrared wavelengths therefore contains information not only on the distribution and structure of relatively cool interstellar clouds, but also on the energetics of the interstellar medium including sites of star formation.

Observations at far infrared and submillimeter wavelengths became feasible only a few years ago when advances in instrumentation were made. Severe atmospheric

absorption does not permit observations with ground-based facilities in the spectral region between 30 and 1000 μm except at a few narrow and low transmission windows at 350 and 1000 μm. Since the thermal blackbody emissivity is proportional to the 4th power of source temperature, very sensitive long wavelength detectors are needed to detect radiation from sources with temperature of only a few tens kelvin. Moreover, the telescope surface at ambient temperature and the residual atmosphere even at high altitude are several orders of magnitude brighter than the astrophysical sources of interest, a condition analogous to doing faint optical photometry in the daytime. These difficulties were gradually overcome in the last ten years with the development of sensitive composite bolometers and airborne observatories carried to high altitude by rockets, balloons and aircraft. These advances have allowed detailed study of processes in the early phases of star formation, the spatial structure of interstellar clouds, the distribution of cool matter in the Galaxy, and extragalactic and cosmic background radiation.

1.2 SUBMILLIMETER SURVEY OBJECTIVE

The Submillimeter Wave Survey that is currently being undertaken by the Goddard Infrared Group is a program to obtain high sensitivity, low spatial resolution photometric maps of the sky at wavelengths longer than 100 μm. The primary objective of this survey is to conduct an unbiased, systematic measurement of extended emission from the Galactic plane. The survey is specifically designed to reveal the distribution and basic physical conditions of the coolest ($T < 30$ K) solid phase component of the interstellar medium, and in doing so provides a homogeneous data base of relevance to many current areas of astrophysical research. For example, the Submillimeter Sky Survey will provide spatial and broad-band spectral information to address major research problems in the following areas:

1) Properties of Discrete Interstellar Clouds

The Submillimeter Sky Survey provides a uniform set of measurements of discrete Galactic sources, and may reveal cold, dense regions not previously observed. Of particular importance is the identification of star formation regions and determination of their physical properties. There is evidence that prestellar objects occur in a hierarchy of temperature and density conditions. Infrared observations

at high spatial resolution (< 1 aromin) permit study of the small-scale structure of these sources, but differential sky chopping makes them insensitive to extended, low gradient sources. A submillimeter wavelength survey with moderate spatial resolution (≈ 10 aromin) is particularly well suited to detection of large scale features and of extended sources, e.g., giant molecular clouds (Stark and Blitz 1978) and HII/molecular cloud complexes (Cheung et al., 1978). In sources where infrared emission arises mainly from cool (T < 50 K) dust grains, submillimeter observations in three spectral bands provide a relatively unambiguous determination of both the dust temperature and a power law index for the grain emissivity. The combination of submillimeter continuum data with CO molecular line data provides both the dust-to-gas mass ratio and relative dust and gas temperatures. This information is necessary for understanding the radiative characteristics of extended interstellar clouds (e.g. Goldreich and Kwan, 1974; Leung, 1976).

It should be emphasized that the advantage of submillimeter wavelength observations for conducting such studies arises from two general properties of dense interstellar dust clouds: 1) most of the luminosity of the coolest dust component emerges at wavelengths longer than 100 μm; and 2) the dense clouds tend to become optically

thin at wavelengths longer than 100 μm. A three channel submillimeter photometer can be expected to reveal the dust temperature, grain emissivity law spectral index, and total cloud luminosity. Figure 1 in Appendix A illustrates how the color-color diagram for the three wavelength bands of the Submillimeter Sky Survey instrument developed in this investigation can be used to determine both the source temperature and grain emissivity law spectral index. Since the clouds are optically thin, the submillimeter observations reveal directly the dust column density in the line of sight, providing information on both the mass distribution as well as the total mass.

The effect of dust on the apparent HeII/HII ratio in the interstellar medium is of considerable importance in cosmology. The submillimeter sky survey bears on this problem in providing information on the physical conditions around ionized regions. This information is needed to determine whether variations in the HeII/HII ratio are due to differential absorption of ionizing photons by dust (Emerson & Jennings 1978; Panagia and Smith 1978) or to stimulated radiation effects in ionized media (Churchwell et al., 1974). A large homogeneous data base would allow a determination of whether systematic trends exist or whether the conditions in well-studied regions prevail on a Galactic scale.

2) The Diffuse Far Infrared Emission and Distribution of Dust in the Galaxy

A major effort is now under way to map the large scale distribution of Galactic constituents. Much of the present knowledge of the structure and kinematic characteristics of the Galaxy was obtained by observing tracers such as HI (Westerhout 1976), CO (Gordon and Burton, 1976; Scoville and Solomon, 1975; Cohen et al., 1980), and ionized gas (Hart and Pedlar; 1976, Altenhoff et al., 1978). The submillimeter sky survey complements these observations in providing additional information on the structure of our Galaxy, particularly the distribution of dust and its relationship to the distribution of gas and stars.

An important focus in this area is the far-infrared diffuse radiation from the Galaxy. Several groups in addition to our own have scanned portions of the Galactic plane at far-infrared and submillimeter wavelengths using balloon telescopes (e.g., Hoffmann et al., 1971, Low et al., 1977, Serra et al., 1978, Maihara et al., 1979, Owens et al., 1979, Campbell et al., 1980, Nishimura et al., 1980). Most of these observations are in the first quadrant of Galactic longitude , where the diffuse far infrared emission increases slowly with increasing longitude (outside the Galactic center region) up to a maximum at $\ell \approx 30°$, and then

decreases rapidly beyond 45°. Many essential characteristics of this diffuse emission, such as luminosity, source temperature, and overall relative distribution remain to be firmly established. This submillimeter survey will extend existing results by providing much more comprehensive spatial and spectral characterization of the diffuse galactic emission. In particular, previous surveys in this spectral range have not included sufficiently many nor sufficiently long wavelength photometric bands to provide significant temperature discrimination for solid phase sources colder than about 30 K. These measurements provided little information about interstellar dust which is not closely associated with high luminosity sources. The submillimeter sky survey undertaken in this thesis is specifically designed to map the emission of the coldest dust component and to discriminate temperatures down to about 10 K. This information is essential for a critical evaluation of the theoretical calculations on heating mechanism and energy balance (Mezger 1978; Drapatz, 1979), the galactic star formation rate (Ryter and Puget 1977), and the correlation between the diffuse far infrared and CO emission (Fazio and Stecker 1976). Finally, mapping of the emission of our Galaxy is needed so that comparison can be made with the observed properties of infrared and molecular line emission in external galaxies (e.g., Telesco and Harper, 1980; Richard et al., 1977; Morris and Lo 1978).

1.3 SCOPE AND ORGANIZATION OF THESIS

This thesis presents the technical development and first scientific results of a systematic survey of the Galactic plane ($|b| < 3°$) in three submillimeter continuum wavelength bands. The thesis is based on the results of a group project with Dr. Michael Hauser as the principal investigator. I have been associated with this project since 1975 when it was in an early phase of conception. This project also involves a number of people mentioned earlier in the acknowledgments section.

In Chapter 2 I present a description of the survey observatory. I was mainly responsible for the design, fabrication, and testing of the submillimeter photometer system. I also participated in the design, integration, and testing of other instrument subsystems of the observatory.

In Chapter 3 I describe the preparations for the survey and the demonstrated performance of the instrument. A sky map showing the region surveyed in the first two flights of the instrument is presented. I was responsible for formulating the flight plans for the first two flights.

In Chapter 4 I discuss the data processing procedures. Flow charts of the data reduction software, including the

parts that I developed, are shown and explained in detail.

In Chapter 5 I describe the photometric calibration procedures based on in-flight calibrations using Jupiter as the photometric standard. I also discuss the sources of statistical and systematic uncertainties.

In Chapter 6 I present the first scientific results of the submillimeter wave sky survey. My analysis is confined within the region along the Galactic plane from $\ell = 8°$ to $\ell = 44°$. I catalogue a list of bright submillimeter source peaks for further study. I also discuss the large scale submillimeter emission from the Galaxy, and compare the results with survey observations at other wavelengths.

CHAPTER 2 INSTRUMENTATION

The Goddard Submillimeter Survey was carried out using a balloon-borne observatory specifically built for this purpose. The observatory is designed to function remotely under ground command from time of launch and during observations taken at the nominal altitude of 29 kilometers. The main design parameters of this observatory are listed in Table 2.1. The major components of this observatory include a gondola frame housing a 1.2 meter, inertially guided Cassegrain telescope, a liquid helium cooled photometer, a momentum wheel, elevation drive motors, control electronics and telemetry system. The instrument parameters are listed in Table 2.2. The entire instrument weighs about 1800 kg and is launched by a 0.25 million cubic meters helium balloon at the National Scientific Balloon Facility in Palestine, Texas. Data are transmitted in real time to a ground station where it is displayed and recorded. The payload is parachuted to ground and recovered after each flight. As of this writing in Fall 1980, the observatory has been launched and recovered successfully twice; the first flight occuring in November, 1979 and the second in August, 1980. A total of 17 hours of useful scientific data was obtained. Details of the major instrument subsystems are described in the following sections.

2.1 TELESCOPE SYSTEM

Figure 2.1 shows a schematic diagram of the Cassegrain telescope and the submillimeter photometer. A summary of the design parameters of the telescope optics is given in Figure 2.2. The design of Cassegrain telescopes has been discussed in detail by a number of authors (e.g. Jones, 1954; Born and Wolf, 1970). The telescope optics and gondola system was built around a 1.22 meter parabolic dish originally fabricated for CO observations at 2.6 mm. A notable feature of the primary mirror is the small focal ratio of 0.375 which allows for an extremely compact optical design despite its large aperture. The initial mirror, though adequate for CO observations, was not well suited for the shorter wavelength submillimeter survey because of a poor surface finish which contained numerous clearly concentric grooves and microscopic porous holes. Because of these limitations, an improved mirror of identical optical design was fabricated. The new primary mirror was machined out of a single piece of rolled-aluminium and finished to provide diffraction limited imagery at 100 μm. The surface was given a moderate polish to reduce scattering at visual wavelengths so that the visible image quality at the focal plane is acceptable for aspect information using a large aperture silicon photodiode star sensor.

The hyperbolic secondary mirror was also machined out of aluminium and given a fine polish. It is slightly undersize so as to prevent the detector from seeing the infrared background emission from and beyond the edge of the primary mirror at the extreme end of the chopper cycle. The secondary mirror is mounted on a mechanical wobbling mechanism which is connected to the telescope cage by a four-armed thin rib structure. Two linear push-pull drivers (Ling Electronics, Anaheim, California) are used to oscillate the secondary mirror in the cross-elevation direction. Movement of the mirror is servo-controlled to produce an efficient square wave cycle having a 10 millisecond transition. The ripple on the flat part of the square wave is typically less than 1% of the full chopper amplitude, corresponding to less than 0.3 arcmin on the sky. The mirror drive is supported by flex pivots on a counter rotating platform assembly, which is dynamically balanced so that very little vibration is transmitted to the telescope structure. This is done to miminize any synchronously induced microphonic noise in the detector. The amplitude of the wobbling secondary mirror is adjustable to produce a beam separation up to about 35 arcmin on the sky at 10 Hz. The amplitude was set conservatively at 25 arcmin in the first flight.

The primary mirror, secondary mirror, and the support

structure are all machined out of the same type of aluminium alloy so that focus shift is minimal as the system cools from 30 C on the ground to -60 C at altitude. The primary mirror and the secondary support cage are mounted on a flat strongback plate reinforced with honeycomb panel. Preliminary alignment of the secondary mirror is achieved by a mechanical alignment tool referenced to a set of bolt holes concentric and co-planar with the primary mirror mounting flange. The alignment tool, when fastened to the strongback and mated to a receptacle at the center of the secondary mirror, defines the axial and radial positions of the secondary mirror. At that point, the secondary mirror support spider arms are firmly attached to the support cage. Finer positional adjustment of the secondary mirror is done with a focus mechanism, which consists of four spring loaded gears which can be adjusted individually to change the tilt or simultaneously to change the axial displacement of the secondary mirror.

The focal plane of the telescope is visually located by pointing the mirror at an astronomical object such as the Moon. The position of the focal plane is a very sensitive function of the axial position of the secondary mirror. A small axial displacement of the secondary mirror produces a shift in the position of the focal plane magnified by a factor of $1+A^2$, where A=10.7 is the magnification of the

telescope. Scattering at visual wavelengths is rather severe so that only a rough outline of the moon is discernible. The focal plane of the telescope is empirically determined by observing the position at which the fuzzy image of the Moon appears to be clearest. Additional measurements referenced to the alignment tool are made to ensure that the primary to secondary mirror distance remains constant with telescope elevation angle.

Confirmation of the telescope focus at submillimeter wavelengths in the laboratory is difficult because of severe atmospheric absorption. An attempt was made to measure the infrared beam profile of the instrument at a wavelength of 1.0-mm where the atmosphere is moderately transparent. The Sun was the only far-field object that was detectable at this wavelength on the ground. Scans of the solar disk indicated that the 1.0-mm beam was not grossly out of focus. It was not until the first flight of the instrument that we were able to confirm the focus at submillimeter wavelengths by scanning across Jupiter.

2.2 SUBMILLIMETER PHOTOMETER SYSTEM

The submillimeter photometer module is a nitrogen-jacketted liquid helium cryostat containing an array of three composite bolometers with associated field optics and spectral filters. A schematic diagram of the inside of the photometer is shown in Figure 2.3. The liquid helium is vented to the atmosphere, so that at balloon float altitude of 29 kilometers, the detectors are cooled down to approximately 1.7 kelvin. At this temperature, the bolometers have an electrical NEP (noise-equivalent-power) of about 3×10^{-14} W $Hz^{-1/2}$. Each detector has a liquid helium cooled, low-pass spectral filter manufactured by Infrared Laboratories of Tuscon, Arizona. The full 3 filter set permits the determination of color temperature and cosmic dust emissive properties for low temperature sources. The three channels have designed cut-on wavelengths of 100, 150, and 300 μm respectively. Additional rejection of radiation shortward of 100 μm is achieved by use of a combination of diamond-dust-coated crystal quartz filters and a black polyethylene sheet on the liquid nitrogen shield, and by an ambient temperature polyethylene window on the dewar cover. The long wavelength response of the instrument extends to a wavelength of about 2 mm, where diffraction cuts off the radiation. Rapidly falling source spectra at long wavelengths cause the effective long

wavelength limit to be substantially less than that allowed by the diffraction limit of the field optics. Additional details of the composite bolometers, field optics, and spectral response are presented in the following sections.

2.2.1 COMPOSITE BOLOMETER

The sensors in the submillimeter photometer consists of low temperature composite germanium bolometers fabricated by myself. The bolometers are heat sensitive devices that consist of two main functional parts, a radiation absorber and a thermometer, connected through a controlled thermal heat path to a heat sink.

In conventional bolometers for infrared observations (Low 1961), incident radiation is absorbed in the bulk of a tiny ($< 1 \times 1$ mm^2) piece of heavily doped germanium (N_d = a few $\times 10^{16}$ cm^{-3}), which also serves as the thermometer. Absorption of radiation causes a rise in temperature which causes a change in the bulk resistance. The absorption efficiency can often be increased by painting the bolometer surface black using paint such as 3M Velvet Black. This type of bolometer is effective up to a wavelength of about 100 μm, and has been used extensively for infrared observations at medium and far infrared wavelengths. At submillimeter wavelengths (>100 μm), the sensitivity of conventional bolometers begins to degrade. This is because the volume of the bolometer must be increased for efficient operation. The thickness of the bolometer material (germanium and/or black paint) is increased to provide sufficient opacity at longer wavelengths. The surface area

required for efficient capture of incident radiation increases with the square of the wavelength to be well matched to the enlarged image size with wavelength (the Airy disc diameter grows as 2.44 $f\lambda$, where f is the focal ratio of the telescope). As the bolometer signal response depends on a rise in temperature, the heat capacity (hence volume) of the bolometer should be as small as possible. At a fixed temperature and time constant, the responsivity of a bolometer varies inversely as the square root of the heat capacity. It is the increase in heat capacity and decrase in opacity that degrade the sensitivity of conventional bolometers at submillimeter wavelengths.

Composite bolometers, in contrast, utilize a compound structure that separates the radiation absorption and thermometer functions of the bolometer. A very tiny piece of doped Ge chip still serves as the thermometer, but the radiation absorbing function is provided by a material with a much lower heat capacity than the corresponding volume of Ge. The absorbing element developed for our composite bolometers is a thin resistive film of bismuth or nichrome coated on the back side of a thin sheet of sapphire or diamond. The resistance of the metallic film is adjusted to impedence match the incoming radiation. Bismuth or nichrome is chosen because of the low electrical conductivity which makes it easy to apply a finite film thickness to obtain the

required resistance. Sapphire or diamond is chosen for low heat capacity, high transparency, high thermal diffusivity, and almost frequency-independent dielectric constant at submillimeter wavelengths. Diamond, with about 1/6 of the specific heat capacity of sapphire, is a better choice with respect to heat capacity.

A schematic of the composite bolometer is shown in Figure 2.4. The size of the germanium chip is about 0.5 x 0.5 x 0.075 mm^3. The size of the sapphire substrate is about 2 x 2 x 0.125 mm^3. The germanium chip is doped with indium and compensated with antimony. Two brass wires, typically about 5 mm long and 12 μm in diameter, provide the electrical contacts as well as a restricted thermal leak to the heat sink. The wire and the Ge chip are etched in a mixture of HNO_3, HF, HCOOH, and HBr acid immediately before being soldered together with indium. The resistance of the bolometer at T_o = 1.8 K is typically about 10-20 megohms with very little background radiation and bias current, and about 5 megohms under typical operating conditions. At a temperature of 1.8 kelvin, the material has a temperature coefficient of resistance 1/R dR/dT of about 6 K^{-1}.

The composite bolometer may be represented in an electrical and a thermal circuit as shown in Figure 2.5. The relevant equations for the system are

Electrical : $dV/dR = I\ R_1/(R+R_1)$ (1)

Thermal : $\alpha = 1/R\ dR/dT_1$ (2)

$P_{in} = C_2\ dT_2/dt + G_2(T_2-T_1)$ (3)

$x\ V = C_1\ dT_1/dt - G_2(T_2-T_1) + G_1(T_1-T_0)$ (4)

where the symbols are defined in Figure 2.5. Assume the incoming radiative power consists of a DC term and a slowly varying AC term :

$P_{in} = P_0 + dP\ e^{i\omega t}$ (5)

so that $T_1 = T_{10} + dT_1\ e^{i\omega t}$ (6)

$T_2 = T_{20} + dT_2\ e^{i\omega t}$ (7)

The responsivity $S = dV/dP_{in}$ may be solved from the above equations. Using a small signal approximation, I get :

$$S = dV/dT\ dT/dP_{in}$$
$$= dV/dT\ 1/(G_1+G_r)\ 1/((1+i\omega\tau_a)(1+i\omega\tau_b)) \quad (8)$$

where $dV/dT = \alpha\ R_1/(R+R_1)\ V$ (9)

$G_r = -\alpha\ P_e\ (R_1-R)/(R_1+R)$ (10)

$P_e = I\ V$ (11)

$\tau_a + \tau_b = G_1/(G_1+G_r)\ \tau_1 + (1 + G_2/(G_1+G_2))\ \tau_2$ (12)

$$\tau_a \times \tau_b = G_1/(G_1+G_r)\ \tau_1 \times \tau_2 \quad (13)$$

$$\tau_1 = C_1/G_1 \quad (14)$$

$$\tau_2 = C_2/G_2. \quad (15)$$

The absorbing element is usually efficiently thermally coupled to the thermometer, i.e., $G_2 >> G_1$ or $\tau_1 << \tau_2$. This condition leads to:

$$S = dV/dT\ 1/((G_1+G_r)(1+i\omega\tau_a))$$
$$= \alpha\ R_1/(R+R_1)\ (G_1(T_1-T_0)R)^{1/2}/((G_1+G_r)(1+i\omega\tau_a)) \quad (16)$$

$\tau_a = C_1/(G_1+G_r)$ is the effective time constant of the bolometer

Under the simplifying assumption that $R_1 >> R$, $\alpha = -A/T$, and $G_r = -\alpha\ G(T-T_0)$, one could reduce equation 16 to (Low 1961):

$$S = (R_0/T_0G)^{1/2}\ /(1+i\omega\tau_a) \quad (17)$$

In practice, R is often not much smaller than R_1, especially in low background and low bias conditions, so that the sensitivity is reduced due to shunting by the load resistor. The signal-to-noise ratio, however, is not affected as the noise is also attenuated by the same amount.

The fundamental noise sources that limit the sensitivity of the composite bolometers are Johnson noise, phonon noise, photon noise, and other less well understood noise sources. The amplitude of these noise sources are listed below (Smith, Jones and Chasmer, 1958):

$$\text{Johnson noise} : V_J^2 = 4kTR\,df \tag{18}$$

$$\text{Phonon noise} : W_p^2 = 4kT^2G\,df \tag{19}$$

$$\text{Photon noise} : W_\nu^2 = 2kT\epsilon P_B \tag{20}$$

$$\text{Other(I,1/f)} : V^2 = AI^m/f^n\,df \quad m,n=1,2 \tag{21}$$

where V stands for voltage and W for power, k is Boltzmann's constant, T is the temperature of the bolometer, df is the electrical bandwidth of the measurement, ϵ is the emissivity of the emission surface, and P_B is the background blackbody radiative power in the spectral band of the photometer. The photon noise depends largely on the optical and spectral design of the instrument and the current or 1/f noise is an unpredictable quantity in the fabrication of the detectors. The noise-equivalent-power, experimentally determined by the total noise voltage divided by the responsivity, can be expressed as :

$$NEP = V_n/S\,\Delta f^{-1/2} \tag{22}$$

The thermal conductance G, heat capacity C, and the

effective time constant τ are important parameters in the optimization of bolometers. It is usual for τ to be set by the requirement of the observations. It should be kept as long as permitted by the characteristic time constant of the incoming radiation(e.g. chopper frequency). In high background applications, background infrared radiation loading can rapidly degrade the sensitivity of the bolometer, so G should be kept as high as possible to maintain the bolometer temperature close to the thermal bath temperature. In low background observations, the dominant noise sources are phonon and Johnson noise. Under this condition, $G = C/\tau$ should be kept as small as possible to maximize the responsivity and minimize the phonon noise. It is therefore advantageous to minimize the heat capacity of the bolometer material.

The absorptive efficiency of the resistive film coated on the dielectric substrate of a composite bolometer can be evaluated using a transmission line theory. For normal incidence, the transmission and reflection coefficients at the front surface from vacuum to dielectric are given by :

$$t_1 = 4n/(n+1)^2 \qquad (23)$$

$$r_1 = (n-1)^2/(n+1)^2 \qquad (25)$$

where n is the dielectric constant of the substrate

material. At the second surface, the transmission, reflection and absorption coefficients are:

$$t_2 = 4n/(n+1+Z_o/Z)^2$$
$$r2 = (1-n+Z_o/Z)^2/(1+n+Z_o/Z)^2$$
$$a2 = (4nZ_o/Z)/(1+n+Z_o/Z)^2$$

where $Z_o = 377$ Ω/□ is the wave impedance of free space and Z is the surface impedance of the resistive film.

The overall transmission, reflection and absorption coefficients are:

$$t = t_1t_2/(1+r_1r_2+2(r_1r_2)^{1/2}\cos\delta)$$
$$r = (r_1+r_2-2(r_1r_2)^{1/2}\cos\delta)/(1+r_1r_2+2(r_1r_2)^{1/2}\cos\delta)$$
$$a = t_1(1-t_2-r_2)/(1+r_1r_2+2(r_1r_2)^{1/2}\cos\delta)$$

where $\delta = 2\pi n\lambda/d$ is the optical thickness of the dielectric. These coefficients as a function of optical thickness δ for a substrate with index of refraction n=3 and thickness d are shown in Figure 2.6 (Hauser and Notarys 1975). In the particular case $Z_o/Z = n-1$, $R_2 = 0$ and one gets a flat spectral response independent of wavelength λ and optical thickness δ. With sapphire, this condition is met when $Z_o = 377/(3.2-1)$ Ω/□ $= 172$ Ω/□. For other values of Z, one generally gets Fabry-Perot fringes due to multiple

reflections. This effect has been utilized to construct bolometers that have peak spectral response at 300 and 1000 μm.

2.2.2 BOLOMETER ELECTRONICS

A functional block diagram of the bolometer circuit is shown in Figure 2.7. The circuit diagram of the bolometer signal amplifier with the bolometer DC voltage monitor and the regulated power supply is shown in Figure 2.8. The front end of the amplifier circuit is a JFET source follower inside the helium cryostat. By passive thermal technique its temperature is kept to 50-100 K. The source follower, close to the bolometer with all connecting wires firmly anchored, is used to reduce the output impedence as seen by the electronics exterior to the cryostat to the order of several hundred ohms. Therefore the wire connection to the front end of the preamplifier is less susceptible to microphonic vibration associated with flight operation. This is particularly important for reducing the pickup from the 10 Hz chopper vibration, which is naturally phase synchronous with the infrared signal. Laboratory tests indicate that this source follower provides effective immunity from vibration induced noise, and is quiet even upon physically tapping on the photometer.

The first stage of the amplifier provides a gain of about 100, and is followed by a four-pole-low-pass-filter with a corner frequency at about 30 Hz. The final gain of the amplifier is either 50 or 5, selectable by ground

commands. This gain changing stage provides a means to increase the dynamic range of the photometer by a factor of 10. The gain choice were driven by observational requirements. For observing source with a low flux level, it is desirable to have a gain high enough so that the wide band noise is resolvable by at least two bits in the analog-to-digital converter. With a 13 bit, +10 volt ADC and a wide band noise of 1 microvolt, the gain should then be about 5000. This gain, however, limits the dynamic range to about 2000. With a noise equivalent flux density of about 100 Jy, the brightest source that can be observed is about 2×10^5 Jy, marginally acceptable for observations of bright sources such as the Moon or Jupiter. With the low gain stage, the overall dynamic range is then increased to about 2×10^4.

The output of the amplifier is sampled 16 times per chopper cycle or 160 Hz, with the sampling synchronised to both the chopper drive signal and the on-board clock. The minimum sampling rate for a 10 Hz sine wave signal is 20 Hz. The reason for sampling at a rate higher than 20 Hz is that the bolometer signal contains higher frequency components and that it is desirable to provide additional phase information so that the chopper waveform can be utilised as the input reference signal for post-flight phase synchronous demodulation. The performance of the chopper waveform may

also be evaluated after flight. Sample aliassing of higher frequency detector noise into the signal frequency band of interest is minimized by the 30 Hz low-pass filter in the amplifier. A normalised gain versus frequency plot of the bolometer amplifier is shown in Figure 2.9.

2.2.3 FIELD OPTICS

In the Submillimeter Survey photometer, parabolic light cones (Harper et al. 1976) are used as field optics. The light cone is used to concentrate the radiation within the 14mm field aperture (10 arc min) onto a bolometer of size 2mm square. In addition, the field optics also provides a means of matching the field of view of the bolometer to the focal ratio of the telescope, thereby rejecting undesirable out-of-field background radiation. To increase the absorptive efficiency, the bolometers are placed inside a cylindrical integrating cavity. This cavity is located at the exit aperture of the light cone so that radiation not absorbed in the first pass through the bolometer is eventually absorbed after multiple reflections within the cavity.

The light cones are fabricated by electro-forming nickel onto a negative mold, which is a precisely machined aluminum mandril. The surface curvature of the light cones is that of an axially symmetric paraboloid with the focus at a diametrically opposite edge at the exit aperture (see Figure 2.10), and an axis inclined at an angle θ_1 relative to the optical axis. Rays coming in at an angle $\theta < \theta_1$ are reflected into the exit aperture; otherwise the rays are multiply reflected back out of the cone. The effective

focal ratio of the light cone is 0.5. The entendue, $A\Omega$, is conserved in the entire optical system. Square-aperture field stops are placed at the focal plane and over the entrance aperture to the cones to define the beam shape on the sky. Laboratory as well as ground based observational tests with the 4-meter telescope at the Cerro Tololo Inter-American Observatory have verified that these parabolic cones perform better than conventional field lens systems in optical efficiency and in out-of-field rejection at a wavelength of 1.0 mm. The signal measured from a point-source laboratory blackbody increases by about a factor of two over the same configuration using a KBr field lens. The improvement in optical efficiency is probably due to the elimination of reflective and absorptive losses in the field lens system. The measured beam profile of the photometer with the parabolic cones is shown in Figure 2.11.

2.2.4 SPECTRAL COVERAGE

The spectral bands of the submillimeter instrument are defined by long-wave pass filters cooled to a temperature of about 2 K. These filters, supplied by Infrared Laboratories Tuscon, Arizona (described by Armstrong & Low 1973), use a combination of scattering by diamond dust and absorption by crystal quartz, CsI, KBr, and CsBr to define the cut on wavelengths (50 % point) at about 120, 170 and 270 μm in the three spectral bands. Except for crystal quartz, the transmission and absorption properties of these crystals are dependent on temperature. Additional blocking of far infrared background radiation at wavelenghths shortward of 100 μm is provided by a diamond-dusted crystal quartz scattering filter and a 120 μm thick piece of black polyethylene at the liquid nitrogen shield, and a 1.5 mm thick polyethylene window on the dewar wall. This window is at ambient temperature. The long wavelength response is limited by diffraction at wavelengths longer than $\lambda_1 > r/(1.22\ f_F) \approx 2$ mm, where $r = 1.225$ mm is the exit aperture of the light cone, and $f_F = 0.5$ is the effective focal ratio of the light cone optics.

The spectral response of the photometer in the three channels was measured using a Nicolet 7000 Fourier transform spectrometer. The measurements were referenced to another

bolometer system which is assumed to have a flat spectral response at wavelengths longer than 100 μm. A room temperature pyroelectric infrared detector (TGS cell) provides another independent means of checking the flatness of the reference bolometer up to a wavelength of about 250 μm. The measured spectral responses of the three photometric bands are shown in Figure 2.12. These spectral responses have been measured repeatedly with good reproducibility. The variations in the relative transmittance for the different measurements are typically less than 5 %.

The measured spectral response for the middle wavelength band (Channel 2) of the photometer indicates that the cut-on wavelength is much longer than the design goal of about 150 μm. The result is attributed to a manufacturering error in making of the filter where a CsI crystal was used instead of the desired CsBr cystal. This error was not discovered until after the first flight, when the spectrometer was first available. The effective cut-on wavelength of this channel is judged to be so close to the longer wavelength channel (Channel 3) so that it is difficult to extract independent information out of these two channels. This filter error was remedied for the second flight of the survey photometer.

2.3 ASPECT SYSTEM

The Submillimeter Survey instrument contains two levels of aspect determination capability: a real time, coarse positional display and an in-storage, accurate star field record.

During flight operation, aspect information is derived from a null magnetometer and an elevation angle encoder. The telescope attitude is transmitted to and displayed at the ground station in real time, enabling the observers to remotely control and verify the telescope pointing. The absolute pointing accuracy is about 1/2 degree, adequate for pointing of the telescope in a survey observation.

Post-flight analysis of the data requires pointing reconstruction with fractional field-of-view accuracy. For this purpose data is used from the output of a silicon photodiode placed at the telescope focal plane to record transit of stars brighter than about 5th magnitude. As our survey is in the region of the Galactic plane, such stars will typically pass through the field-of-view of the photodiode every few minutes. The photodiode signal is sampled at 40 Hz and telemetered to the ground station where it is recorded. The relative alignment between the photodiode star sensor and the submillimeter beam is

determined by in-flight observations of planets which are both visual and submillimeter sources. This star sensor provides the primary means of aspect determination in the data analysis.

An additional means for more accurate aspect determination and for continuous monitoring of the pointing system performance is provided by an aspect camera co-aligned with the telescope on the telescope cage. This 35-mm camera (Robot with a 35mm f2.8 lens) uses a 200-ft roll of high speed Kodak 2475 recording film, permitting the recording of 4th magnitude stars during the night while scanning. Each film frame is annotated with a fiducial grid imposed directly at the camera focal plane and a frame number counter, which is the image of an external LED display. The frame number is also entered in the telemetry at the time of exposure. During scanning of a single raster line the shutter is opened and closed so that bright stars appear as a segmented streak pattern. At the end of a raster line the frame is advanced by one and a new picture begin for the next raster line. Under normal circumstances, it is expected that occasional sampling of the photographs for verification of the photodiode information would suffice.

2.4 GONDOLA AND POINTING SYSTEM

The gondola and pointing system have been previously described (Silverberg et al., 1979). In this section an updated version from this reference is given. Table 2.1 contains a summary of the pointing system requirement. A photograph of the complete gondola with the telescope mounted is shown in Figure 2.13. In this photograph, starting from the top, one can see a weighted inertia bar, the telescope with the secondary mirror, and a reaction wheel just below the telescope. The overall gondola structure is about 4.3 m high and 3.4 m in diameter, and weighs approximately 1800 kilograms fully loaded for flight.

An important design requirement for the gondola is to provide adequate protection for the instrument so that the system can sustain repeated launch and recovery operations with a minimum amount of damage and need for major refurbishment. This requirement is met by having soft, crushable and easily replaceable outer crash rings surrounding a sturdy inner frame fabricated out of heavy aluminum tubing. The sturdy inner frame is designed to be able to preserve the alignment between the two telescope elevation bearings under repeated landing stress. This gondola construction has proven to provide adequate protection on two landings, the first one without any

significant damage. On the second landing, after the flight in August 1980, the payload was dragged by an undetached parachute for about 500 m. The outer crash rings sustained extensive damage, but the inner frame and the optics system remained intact.

The telescope is guided and stablized in an altitude-azimuth mount. This simple telescope mount is sufficient for our modest pointing requirements in a survey mode (see Table 2.1). The elevation drive consists of either or both of two DC motors mounted on the elevation axis. The elevation angle is sensed by a 13-bit shaft angle encoder. The azimuth is controlled by torquing a heavy reaction wheel which moves the entire payload. The wheel has a moment of inertia of about 1/25 that of the entire payload. It is driven by a DC torque motor. The azimuth position is sensed by a null magnetometer which is read out via a 12 bit encoder. A cross magnetometer serves as a back-up azimuth sensor. The balloon is coupled to the gondola through an active double race payload support bearing (Hoffmann, 1972, and Hazen et al., 1974), which isolates the gondola from balloon rotations and also permits angular momentum to be dumped to the balloon. The outer race of this bearing is driven sinusoidally at 7 Hz so that bearing static friction is not seen. The inertia bar mounted above the payload support shaft is present to assure

bearing breakaway. Should the azimuth reaction wheel acquire too much rotational speed due to external torques, the excessive momentum is dumped to the balloon by applying a DC offset to the support bearing sinusoidal drive. This feedback is provided by a proportional control circuit referenced to the reaction wheel tachometer. The system has a narrow bandwidth so as not to dump momentum quickly and wind up the cable connecting the gondola to the balloon.

The telescope may be pointed and maneuvered in two modes. In either mode, both axes are servo-controlled, with references dependent on the telescope control mode. The first mode, under inertial guidance, was the primary mode of operation in the first two flights of the package. In this inertial mode, the servo system takes the references from a gyro which senses the rotation rate about two axes orthogonal to the telescope optical axis. An electronic integrator provides the position reference to the servosystem. When the inertial mode is entered, the integrator is first reset and released. Subsequently the gyro rate outputs, governed by the Earth's rotation rate, are being integrated to produce position error signals. The servo-system moves the telescope in such a direction as to null this position error signal, thereby providing continuous tracking of the sky rotation. The bandwidths of the servo-system are about 1 Hz in the azimuth axis and 1.5

Hz in the elevation axis. Positioning of the telescope from one field to another is achieved by electronically offseting the gyro rate by a fixed voltage, so that slewing is kept at a contant rate. During source acquisition, the telescope slews at a constant rate of 1 deg/sec. An electronic raster generator provides the necessary signal sequence to execute a raster pattern of 6 degrees x 6 degrees on the sky. Each scan line of the raster pattern is 6 degrees long along the cross elevation direction. At the end of each line, the telescope is commanded to step 8 arcmin down in elevation and scan backward in cross elevation. A complete raster box is filled by 43 separate scan lines.

The second mode is a backup mode in case the gyroscope fails. In this case the servo-system derives its reference signals from the reaction wheel and elevation axis tachometers. Again, the rate information is electronically integrated to provide a position reference. This mode does not compensate for sky motion or for any external torque due to atmospheric turbulence or balloon interaction. Control in both axes is therefore rather unpredictable under normal circumstances. There is no electronic raster generator in this mode. Surveying the sky in this mode therefore requires extensive interaction from the ground control personnel. There was no need to use this mode in either the first or second flight.

TABLE 2.1

SUBMILLIMETER SURVEY OBSERVATORY PARAMETERS

In-Flight Pointing Accuracy	1/2 degree
Aspect (post flight)	3 arcmin
Pointing Stability	5 arcmin p-p(1-2min)
Controlled axes	Azimuth, Elevation
Elevation range	-10° to +60°
Azimuth range	0° to 360°
Raster parameters	
Size	6° x 6°
Scan rate (cross elevation)	20 arcmin/sec
Line spacing (elevation)	8 arcmin
Slew rate (non-raster)	1 deg/sec
Data rate	20.5 K bps
Total payload weight at launch	1800 kg

TABLE 2.2

SUBMILLIMETER SURVEY INSTRUMENT PARAMETERS

Telescope configuration			Cassegrain
Primary Diameter			1.2 m
Primary Focal Ratio			0.375
Effective Focal Ratio			4
Chopper: Waveform			square
Frequency			10 Hz
Throw			20 arcmin
Field-of-view		10 arcmin x 10 arcmin	
Photometer	Band 1	Band 2	Band 3
Cut-on λ(μm) (50%)	106	238	270
Effective λ(μm) (125 K)	152	281	334
NEFD(Preliminary) (Jy $Hz^{-1/2}$)	350	270	190
NER(Preliminary) (w cm^{-2} sr^{-1} $Hz^{-1/2}$)	5.6×10^{-11}	2.4×10^{-11}	1.6×10^{-11}

FIGURE CAPTIONS

Figure 2.1: Schematic diagram of the optical system showing the 1.2 meter primary mirror, the secondary mirror with the wobbling mechanism, the photodiode star sensor, and the liquid helium cooled photometer. A dichroic mirror in front of the focal plane reflects the infrared beam onto the photometer.

Figure 2.2: Schematic diagram showing the Cassegrain telescope design parameters.

Figure 2.3: Detailed layout of the interior of the photometer showing the bolometer array with the associated light cones optics and long-wave pass filters. The assembly is cooled to a temperature of about 1.7 K at a float altitude of 29 km by the liquid helium bath in pressure equilibrium with the atmosphere.

Figure 2.4: Schematic drawing of a composite bolometer. The size of the Ge thermometer is about 0.5 x 0.5 mm^2. The thermometer is attached to a radiation absorber which is a dielectric substrate coated with a resistive film on the back side. The composite bolometer is suspended by two thin wires, which provide restricted

thermal conduction paths to a heat sink and the electrical connection to a preamplifier.

Figure 2.5: Electrical and thermal circuit representation of a composite bolometer.

Figure 2.6: Reflection, transmission, and absorption coefficients of the resistive film coated dielectric substrate of a composite bolometer.

Figure 2.7: Functional block diagram of the bolometer electronics, showing the cooled JFET source follower inside the liquid helium dewar, a front stage high gain amplifier, a 4-pole 30-Hz low pass filter, and a remotely commandable gain changing stage.

Figure 2.8: Circuit diagram of the bolometer signal amplifier, low pass filter, gain switching stage, the bolometer DC voltage monitor, and the regulated power supply.

Figure 2.9: Frequency response of the bolometer signal amplifier. The low frequency roll-off is set by AC coupling capacitors. The attenuation at high frequencies is set by the 30-Hz low pass filter.

Figure 2.10: Schematic and design parameters of the off-axis parabolic light cone field optics. θ_1 defines the angle of acceptance of the light cone optics.

Figure 2.11: Relative beam profile of the light cone optics at submillimeter wavelengths.

Figure 2.12: Relative transmission spectrum of the three spectral bands of the photometer measured with a Fourier transform spectrometer.

Figure 2.13: Photograph of the Submillimeter Wave Survey observatory.

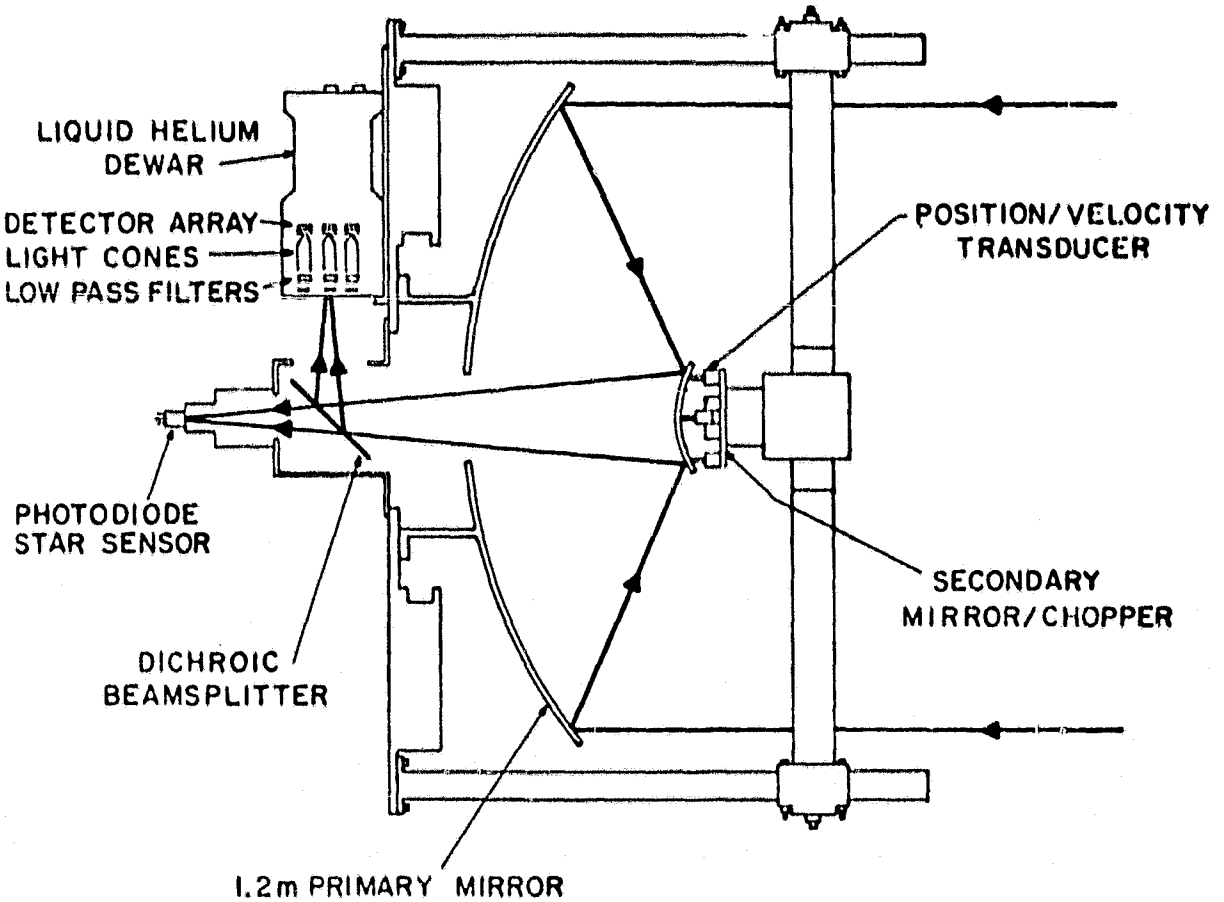
LIQUID HELIUM
DEWAR
DETECTOR ARRAY
LIGHT CONES
LOW PASS FILTERS
POSITION/VELOCITY
TRANSDUCER
PHOTODIODE
STAR SENSOR
SECONDARY
MIRROR/CHOPPER
DICHROIC
BEAMSPLITTER
1.2m PRIMARY MIRROR

FIGURE 2.1

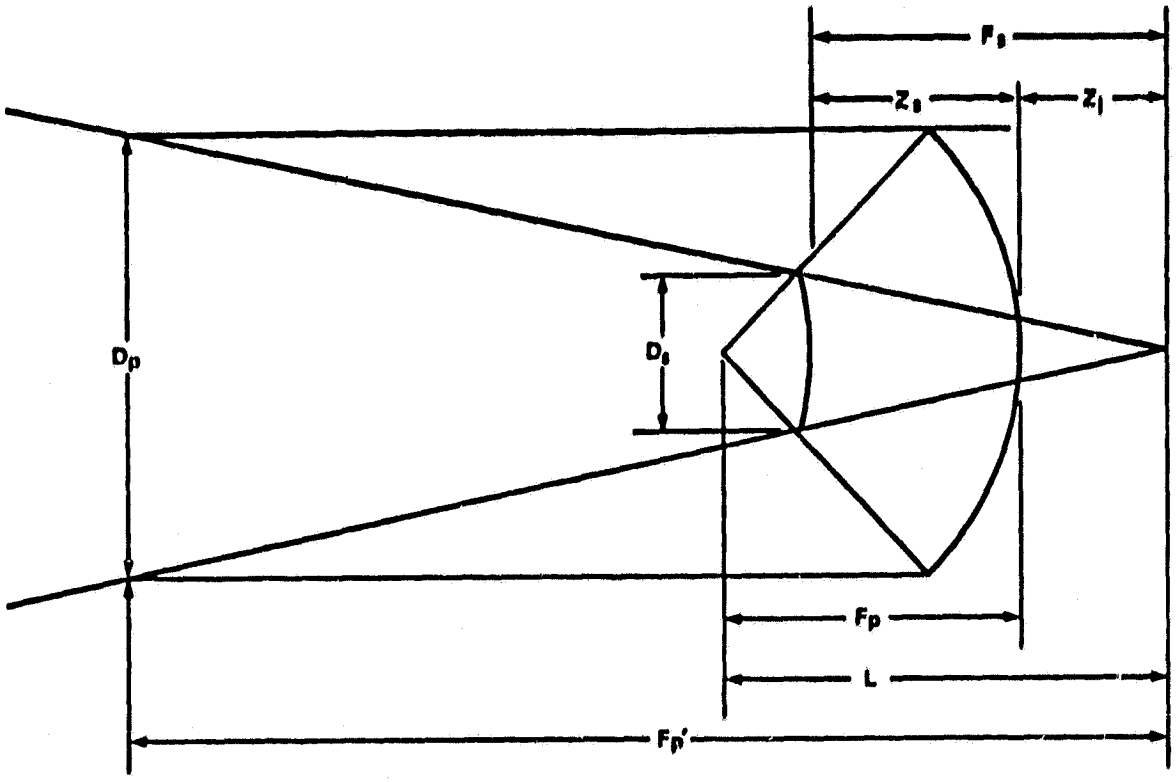

Primary Mirror Aperture, D_p	=	1.2 m
Focal Length of Primary Mirror, F_p	=	0.45 m
Eccentricity of Primary Mirror, e_p	=	1
Secondary Mirror Aperture, D_s	=	19.85 cm
Eccentricity of Secondary Mirror, e_s	=	1.2195
Equivalent Focal Length, $F_p' = D_p F_s/D_s$	=	4.8 m
Equivalent Focal Ratio	=	4.0
On Axis Distance from Center of Primary Surface to Focal Plane, Z_l	=	38.10 cm
On Axis Distance from Center of Primary Surface to Secondary Surface, Z_s	=	38.48 cm
Magnification, $A = F_s F_p/(D_s D_p)$	=	10.67
Variation in Focal Distance for a Change in Secondary Mirror Position, $dz_l/dz_s = 1 + A^2$	=	114.78
Plate Scale, S	=	0'.716/mm

FIGURE 2.2

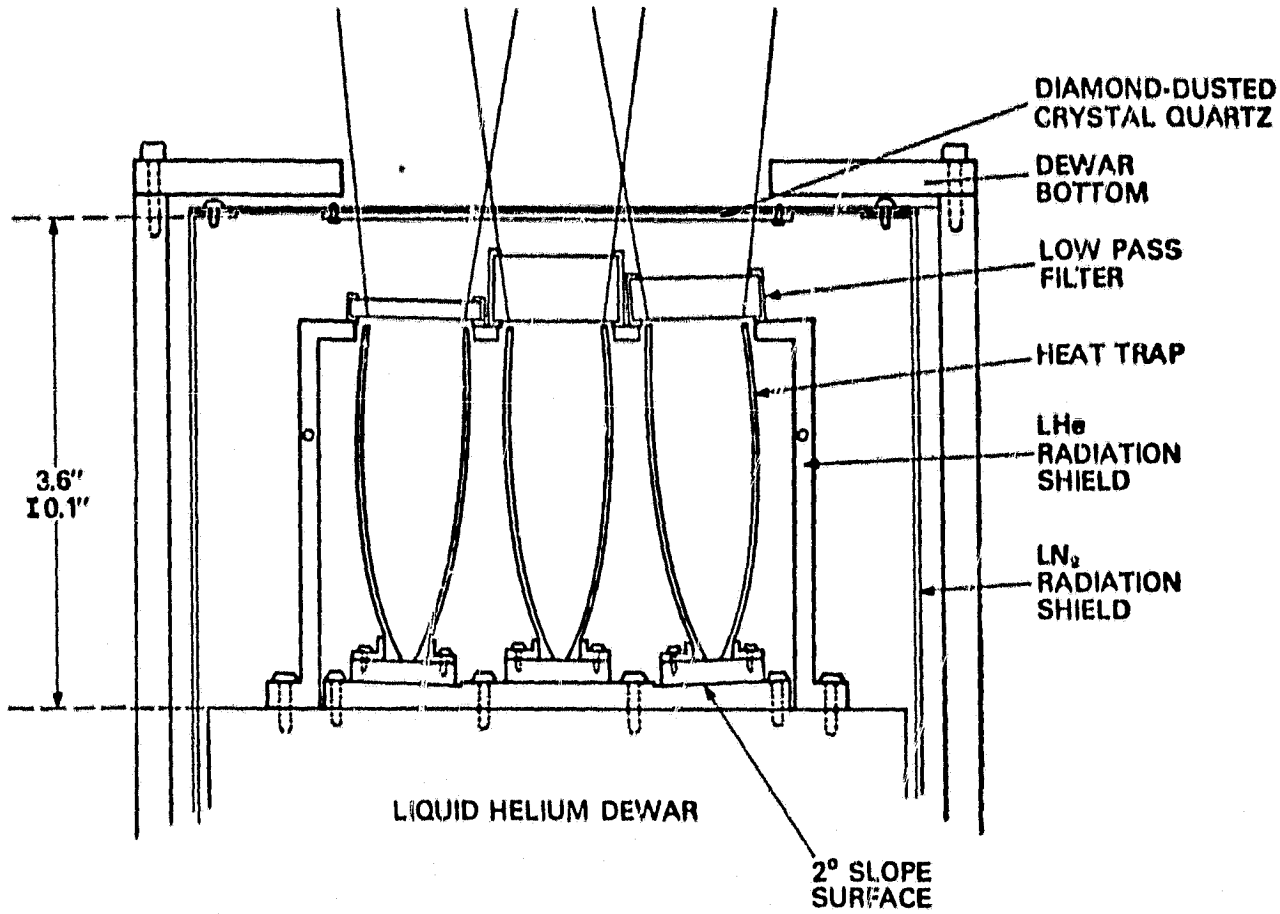
DIAMOND-DUSTED CRYSTAL QUARTZ
DEWAR BOTTOM
LOW PASS FILTER
HEAT TRAP
LHe RADIATION SHIELD
LN2 RADIATION SHIELD
3.6" ± 0.1"
LIQUID HELIUM DEWAR
2° SLOPE SURFACE

FIGURE 2.3

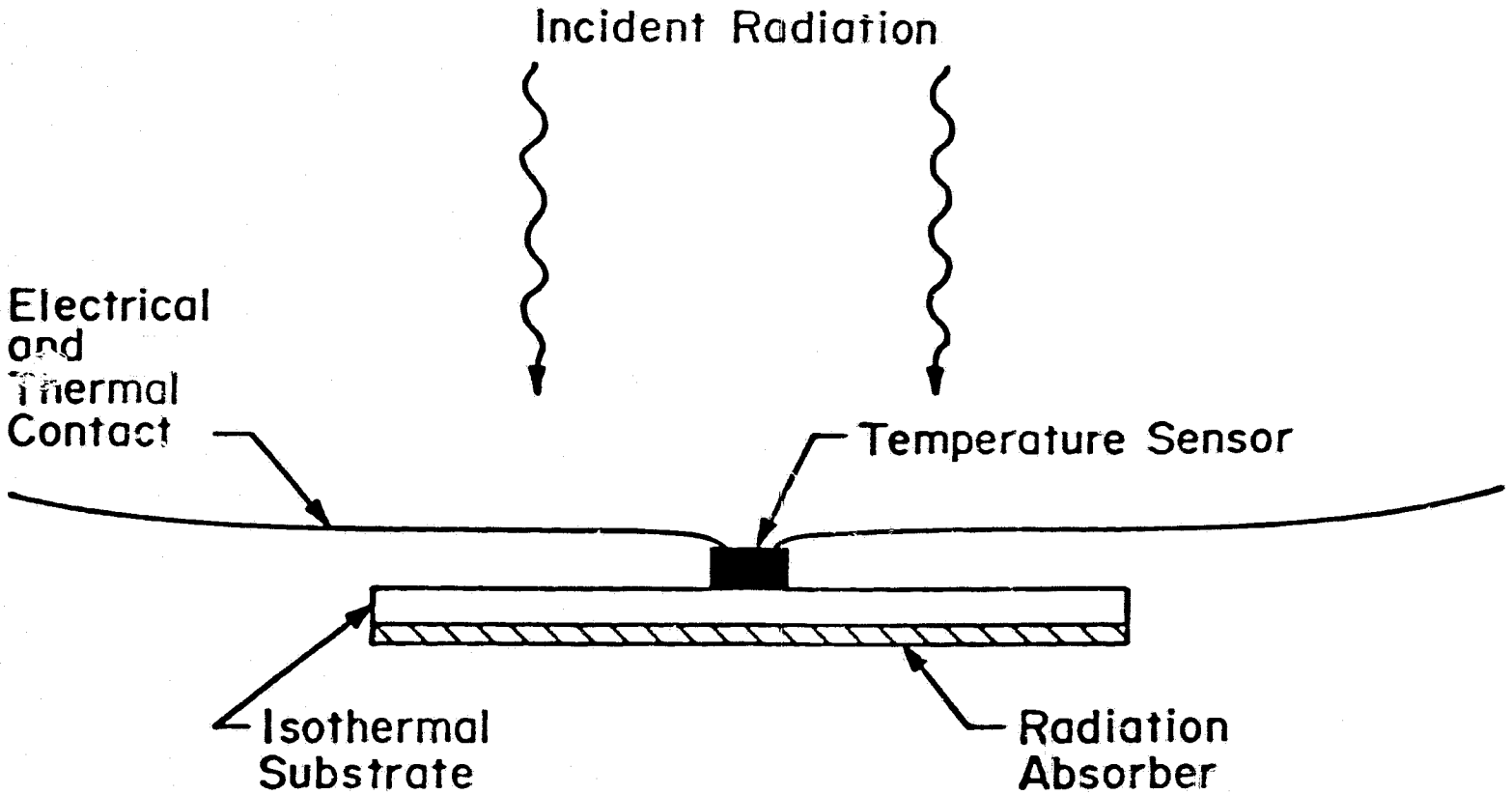

COMPOSITE BOLOMETER

FIGURE 2.4

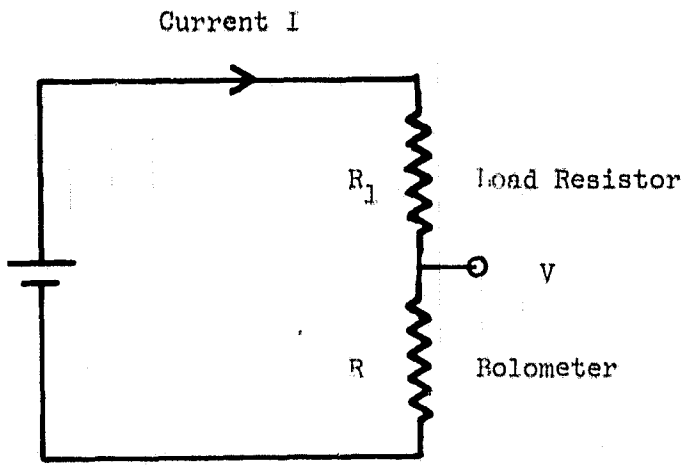

Electrical Circuit

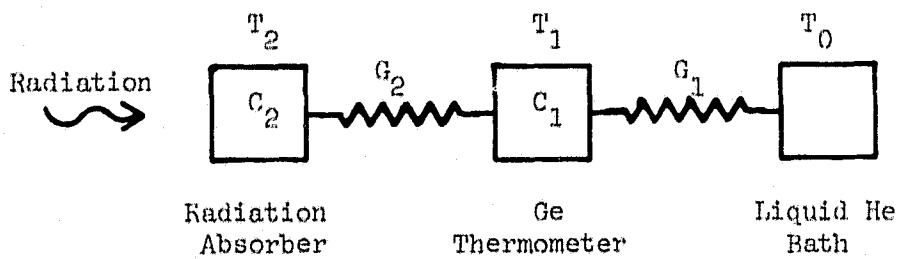

T = Temperature G = Thermal Conductance C = Thermal Capacitance

Thermal Circuit

FIGURE 2.5

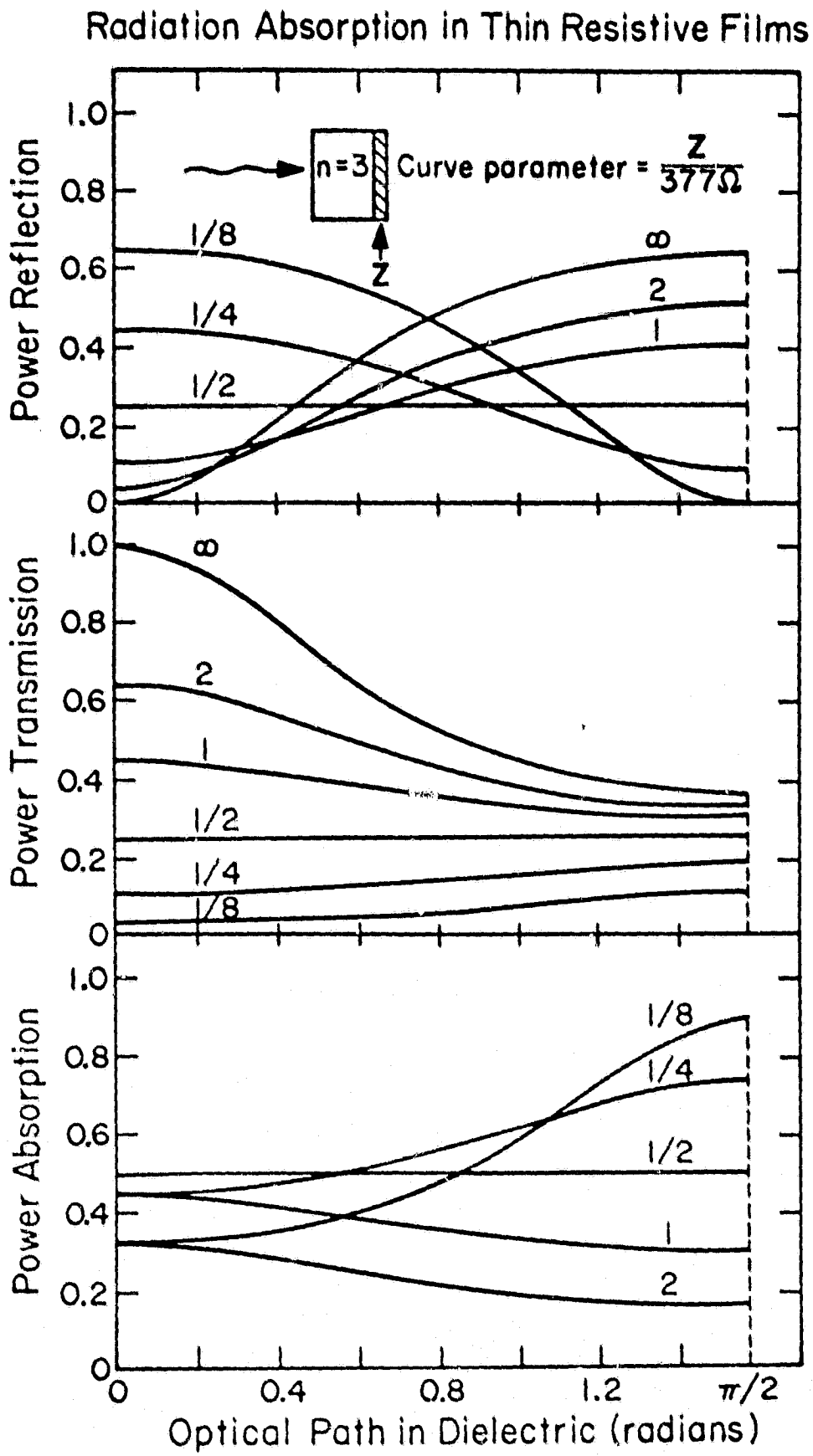
Radiation Absorption in Thin Resistive Films
Power Reflection
Power Transmission
Power Absorption
n=3
Curve parameter = Z/377Ω
Z
1/8
1/4
1/2
1
2
∞
0
0.2
0.4
0.6
0.8
1.0
0.4
0.8
1.2
π/2
Optical Path in Dielectric (radians)

FIGURE 2.6

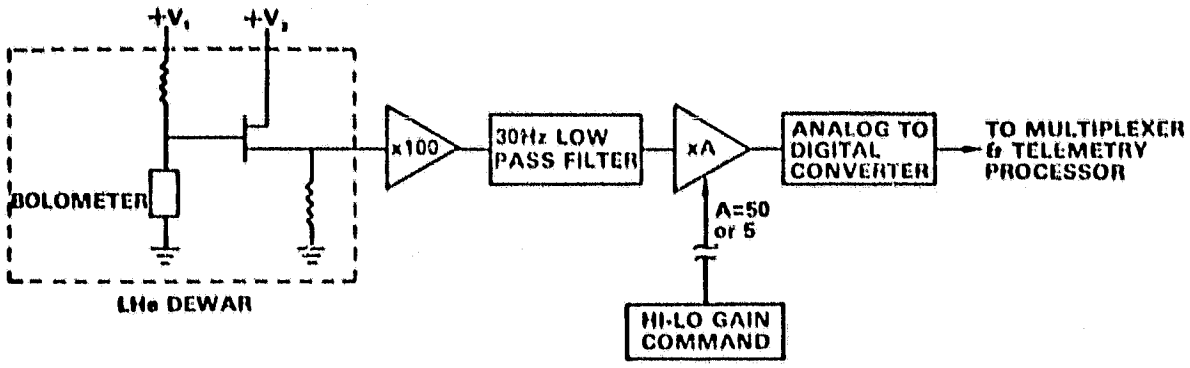
+V1
+V2
BOLOMETER
LHe DEWAR
x100
30Hz LOW PASS FILTER
xA
A=50 or 5
HI-LO GAIN COMMAND
ANALOG TO DIGITAL CONVERTER
TO MULTIPLEXER & TELEMETRY PROCESSOR

FIGURE 2.7

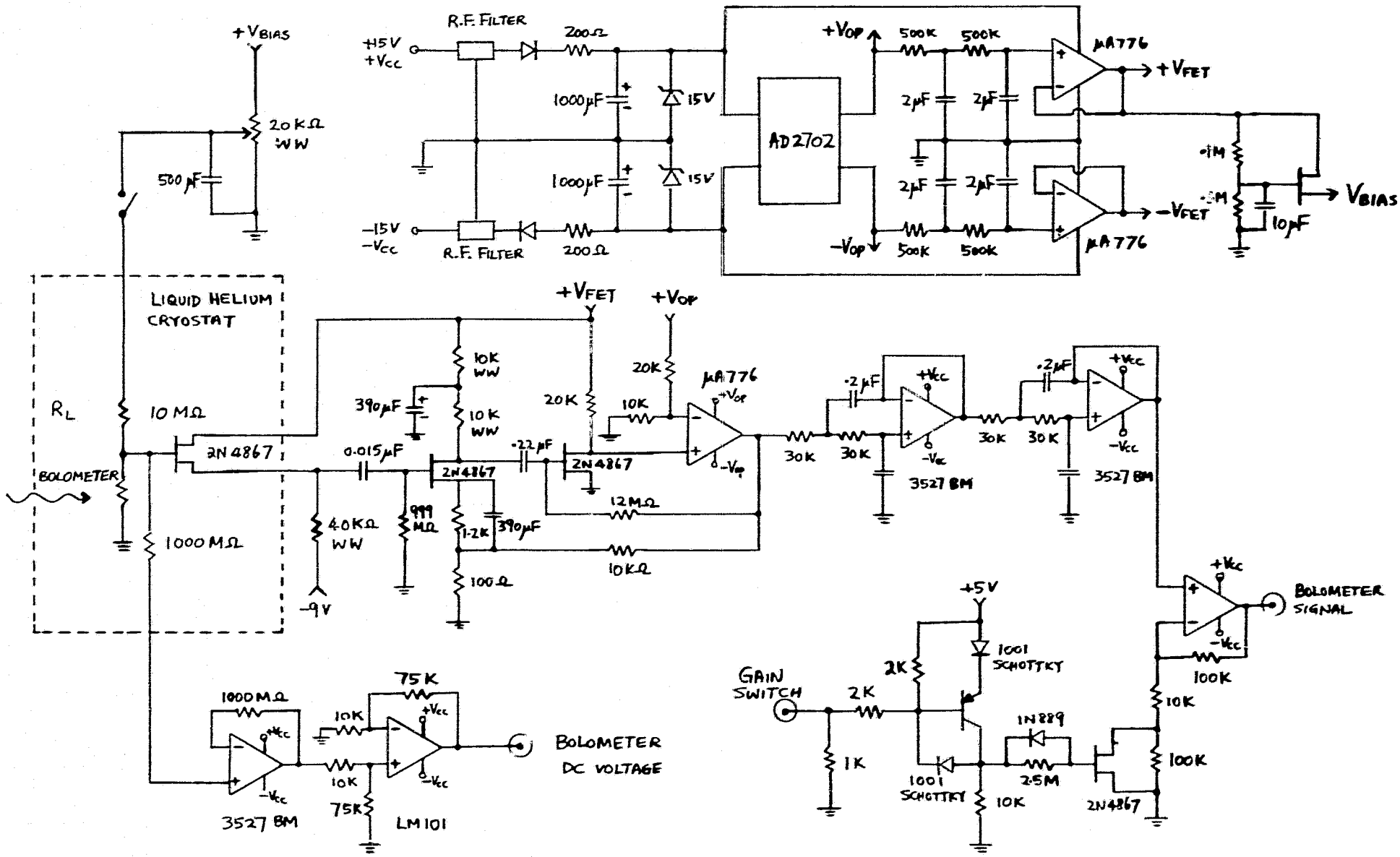
+VBIAS
20KΩ WW
500μF
R.F. FILTER
+15V +Vcc
200Ω
1000μF
15V
-15V -Vcc
AD2702
+Vop
-Vop
500K
2μF
μA776
+VFET
-VFET
VBIAS
1M
10μF
LIQUID HELIUM CRYOSTAT
RL
10 MΩ
BOLOMETER
1000 MΩ
2N4867
0.015μF
390μF
10K WW
20K
10K
.22μF
12MΩ
10KΩ
4.0KΩ WW
999 MΩ
1.2K
100Ω
-9V
30K
.2μF
3527 BM
+Vcc
-Vcc
1000MΩ
75K
LM101
BOLOMETER DC VOLTAGE
+5V
GAIN SWITCH
2K
1K
1001 SCHOTTKY
IN889
2.5M
100K
BOLOMETER SIGNAL

Figure 2.8

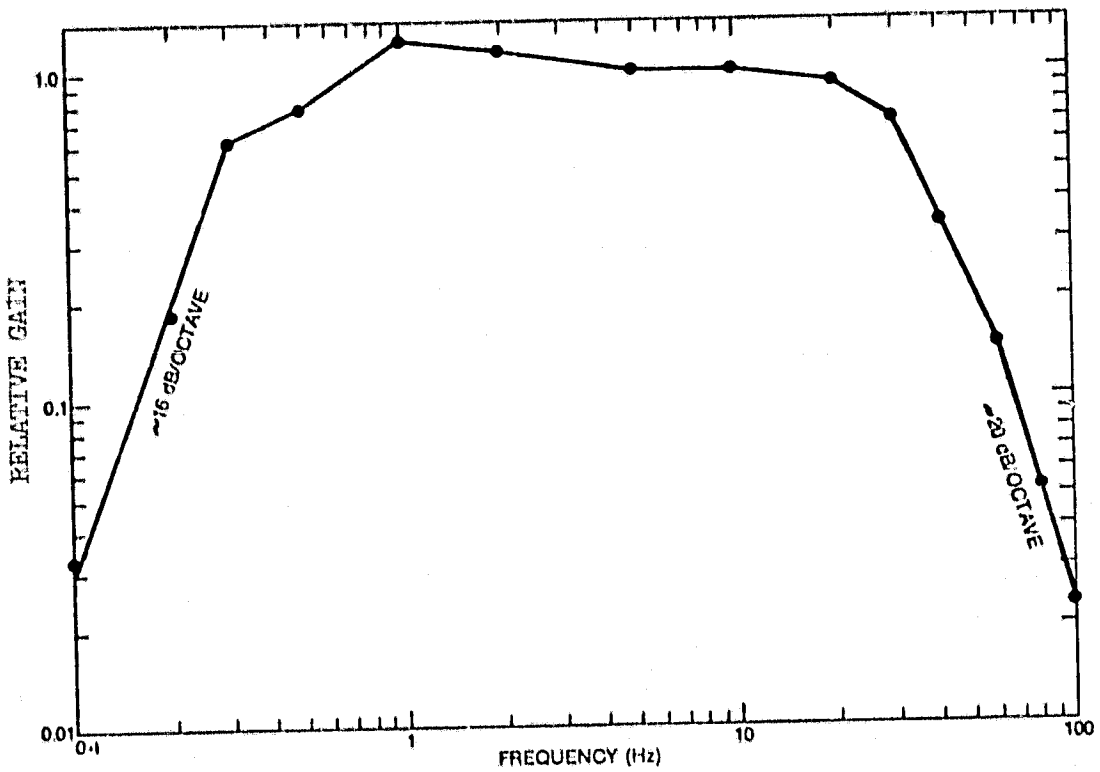
RELATIVE GAIN
1.0
0.1
0.01
0.1
1
10
100
FREQUENCY (Hz)
~16 dB/OCTAVE
~20 dB/OCTAVE

FIGURE 2.9

DESIGN PARAMETERS:

$r(z) = -(0.125988\,z + 1.5750) + (5.64427\,z + 7.8400)^{1/2}$ mm

$\Theta_1 = \sin^{-1}(1/2 f_T) = 7.180°$

$r_1 = \Theta_b f_T d_T = 9.505$ mm

$r_2 = r_1 \sin\Theta_1 = 1.225$ mm

$\ell_T = (r_1 + r_2)/\tan\Theta_1 = 61.0$ mm

$\ell_B \approx 0.35\,\ell_C$

f_T = focal ratio of telescope = 4

Θ_b = angular field of view = 14°

d_T = telescope aperture = 1.2 m

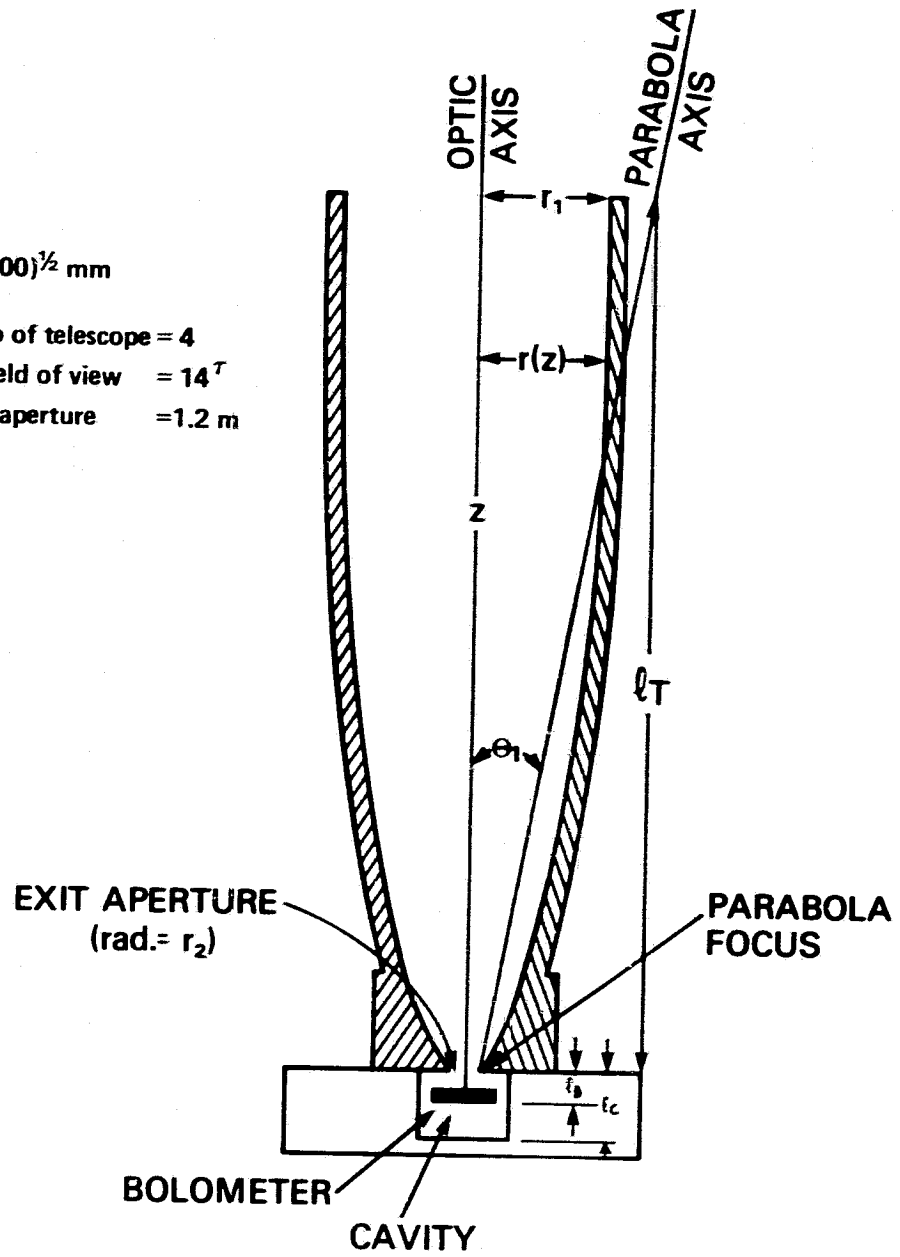

FIGURE 2.10

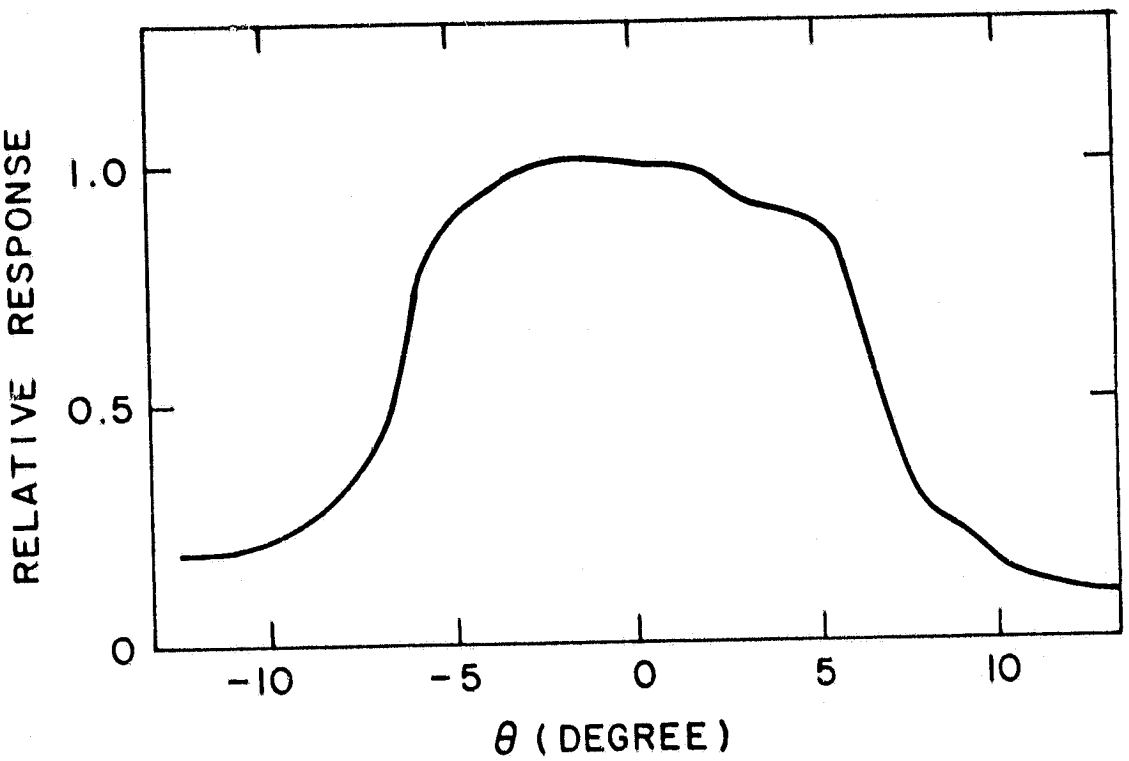

FIGURE 2.11

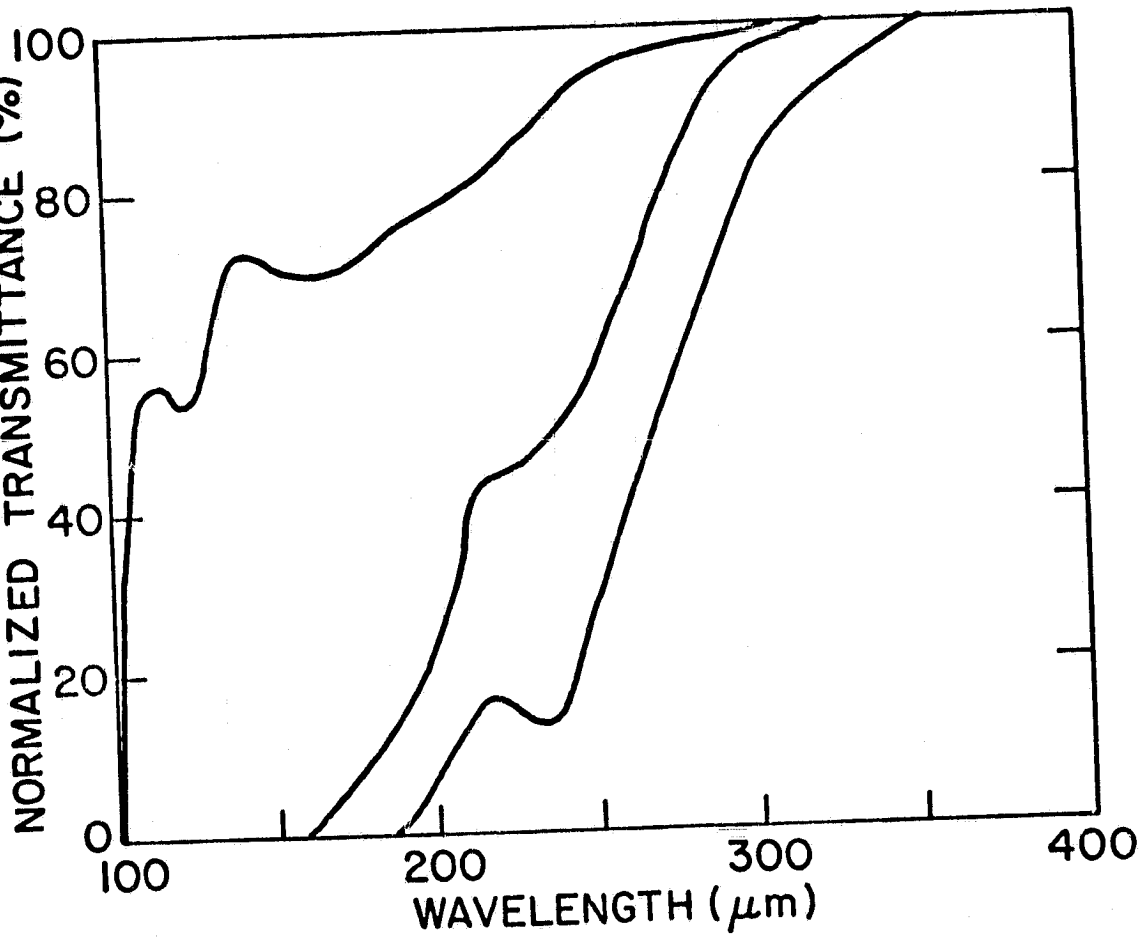
NORMALIZED TRANSMITTANCE (%)
100
80
60
40
20
0
100
200
300
400
WAVELENGTH (μm)

FIGURE 2.12

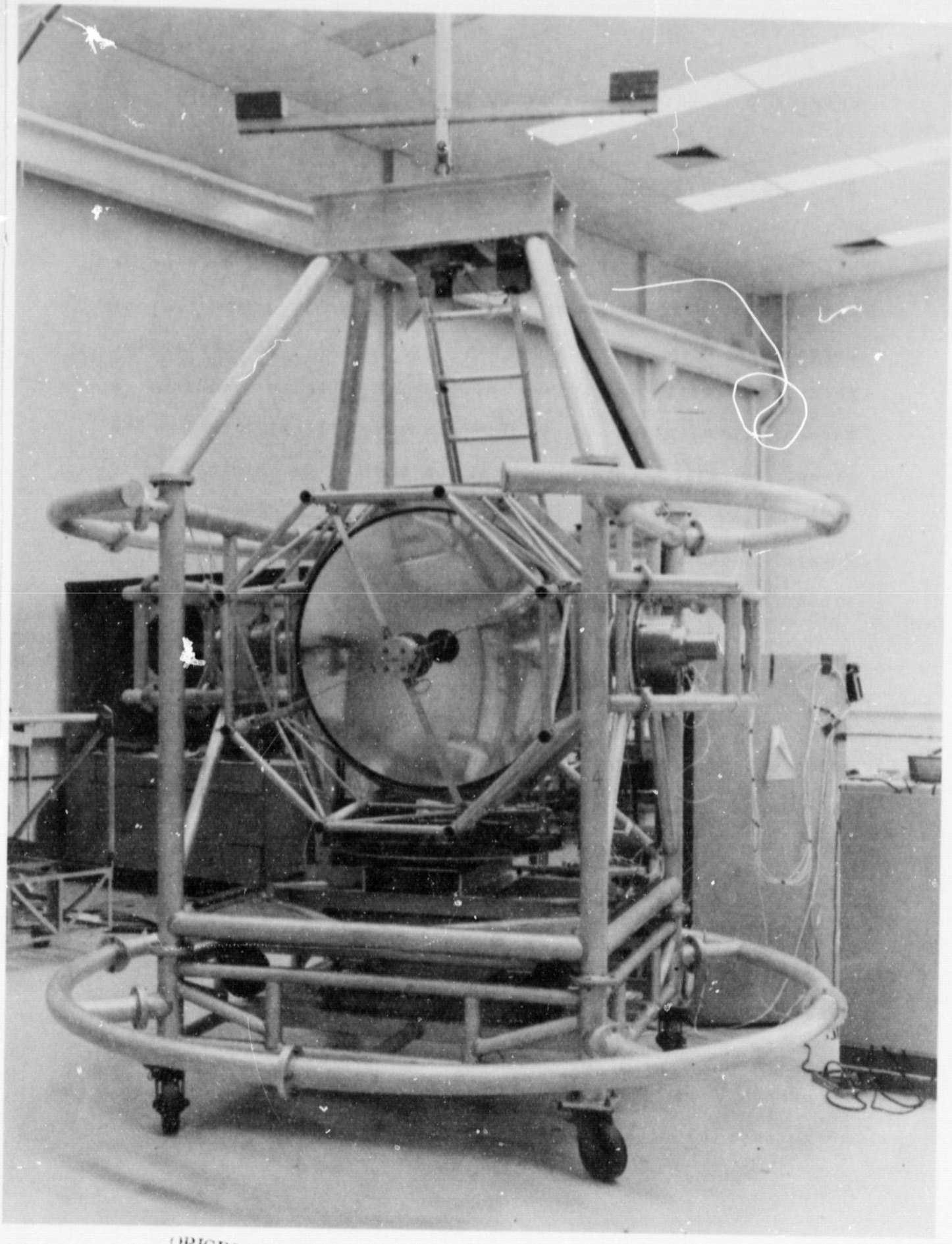

FIGURE 2.13

CHAPTER 3 SURVEY PREPARATION AND FLIGHT OPERATIONS

3.1 SURVEY STRATEGY AND OBSERVATION PLANNING

The objective of the Submillimeter Survey is to provide complete mapping observations of the Galactic plane regions accessible from the launch site in Texas. To accomplish this goal with a minimum number of flights requires a careful formulation of a comprehensive flight plan. The extent to which this plan may be varied is limited by a number of instrumental and astronomical constraints. Several aspects of the considerations in the survey planning are described here.

The basic strategy is to map successive 6° x 6° fields along the Galactic equator, with each field separated by about 6° in longitude. Contiguous fields are partially overlapped to provide photometric continuity. Selection of the fields to be scanned at a given time is guided by the following requirements: 1) the elevation angle of the field is to be within the 0-60° elevation range of the telescope (preferably not too close to the limits); and 2) the orientation of the Galactic equator is to be at an angle greater than 45° to the cross-elevation scan line (preferably as close to 90° as possible) so that the sky brightness gradient is high. The combination of selected

fields in a flight is assembled in such a way as to maximize the opportunities for which conditions (1) and (2) are most favorably met. In particular, the following received priority treatment: a) Galactic plane regions with a narrow time window in which conditions (1) and (2) can be met; b) favorable conditions under which several contiguous raster fields might be scanned sequentially without interruption, and c) regions of particular astrophysical interest. In addition, consideration was also given to ensure that different flights of the survey were optimally compatible with one another to ensure an efficient completion of the project. During each flight, planets and selected "standard" fields were observed repeatedly to establish the photometric calibration and monitor the stability of the system. The standard fields, containing low temperature, extended sources, are also useful in establishing flight-to-flight photometric consistency of the data.

As an aide to a comprehensive flight planning process, an azimuth-elevation sky map showing the location and orientation of the entire Galactic plane as a function of sidereal time was made and is shown in Figure 3.1. A color-coded version of this sky map has been used extensively in flight planning as well as in the field to permit quick decisions to be made on modifying the flight plan. Several computer programs have also been developed

for flight planning purposes. Some of the outputs are shown in Figure 3.2. A listing of the flight plan for the first flight is shown in Table 3.1.

3.2 FLIGHT OPERATION

The basic guideline in the development of the flight system is to obtain a reliable instrument that can function and survive in the environmental extremes and physical abuses associated with balloon-borne operations. To obtain an understanding of and confidence in the instrument, extensive testing was carried out on both the subsystem and system level, in ambient and in thermal-vacuum environment, in the laboratory and in the field. These tests revealed many potential weaknesses in the design and fabrication process, lead to intelligent reworkings, and thereby contributed much to the success of the first two flights.

The survey observatory was dissembled into several modular parts before being shipped to the National Scientific Balloon Facility in Palestine, Texas. There the observatory was reassembled and interfaced with the telemetry package provided by NSBF. The payload was put through a magnetometer calibration on an isolated field away from major steel structures. After a satisfactory system test of the entire payload under remote control, the observatory was declared flight-ready.

Preparation for launch was made when the meteorological forecast indicated the conditions on the ground and at

altitude would be favorable for a successful launch, flight, and recovery. The launching operations were handled entirely by the NSBF personnel. A 52-ton special purpose vehicle (Tiny Tim!) moved the observatory to the center of a 1 km diameter launch pad. The instrument was again placed through a final readiness check. When the decision to launch was made, the launch vehicle picked up the payload under a pair of jaws. The polyethylene balloon was laid out and attached to the payload through a suspension link containing a parachute. The balloon was filled with helium gas while being restrained by a metal spool attached to another vehicle. At the moment of launch, the balloon was released, and the launch vehicle holding the payload manuevered quickly until the payload was held by a taut line directly underneath the balloon. At that precise moment the payload was released.

During the ascent phase, all the instruments of the observatory were activated. The only exception was the azimuth drive system (the momentum wheel and payload support jitter bearing), which was not turned on so as to avoid excessive servo-response induced by atmospheric disturbances during the initial phase of ascent. There was no latching mechanism for restraining telescope motion during ascent. The telescope was held at a fixed elevation angle by the elevation axis servo-system in order to prevent the

telescope from pointing at the setting Sun or from hitting the stops at the extreme positions. After passing through the tropopause, the azimuth control system was turned on, and the telescope was commanded to acquire a bright infrared source such as a planet or the Galactic center region to provide a preliminary check on the pointing and detector systems performance. High quality data were not obtained until about 2.5 hours after launch when the payload reached an nominal float altitude of 29 km. At that altitude, the bolometers were cooled down to 1.7 K by the liquid helium bath in pressure equilibrium with the atmosphere, and the residual atmospheric opacity was negiglible.

In the first two flight of the instrument, the observations were terminated when the payload approached the telemetry limit which is about 300-350 miles from the balloon base. All instrument subsystems except the telemetry package were powered down before the descent phase. The gondola was detached from the balloon by commands issued by the pilot in a chase plane in the vincinity of the landing area. The payload was parachuted to ground and recovered by a prepositioned crew.

3.3 SKY COVERAGE AND FLIGHT PERFORMANCE

During the first flight in November 1979, the survey instrument returned a substantial amount of useful scientific data. The flight lasted about 14 hours, with 11 1/2 hours of productive observing at an altitude of 29 kilometers. A total of 43 fields of 6° x 6° each were raster scanned, covering altogether 26 distinct fields on the sky. The region include about 1/3 of the Galactic plane with $|b| < 3°$, a 200 square degree field around the Orion/Rosette molecular clouds, a few other out-of-plane sources, as well as calibration observations on Venus, Mars, Jupiter, Saturn and the Moon. The region scanned are shown in a celestial map in Figure 3.3. A list of the celestial positions of the raster field centers is given in Table 3.2

During the entire flight, the payload was fully commandable with all subsystems functioning properly. Nearly 90 % of the time at float altitude was spent with the system recording astronomical data in the raster scan mode. Rasters were positioned with an accuracy of about 1/2° in flight. A positional uncertainty of less than one beam width (1 to 3 arcmin) can be reconstructed from the field photographs and star transit information obtained respectively by the camera and visible light photodiode. The microcomputer-controlled (LSI-11) ground station

contributed much to the very effective operation by providing a real-time CRT display of crucial science, pointing, and engineering data and a strip chart record of the digitally demodulated signal from the three infrared detectors and aspect sensor. A sample CRT display from the ground station computer is shown in Table 3.3. The payload was successfully recovered from Western Alabama with only minor damage to a crash-ring section and fracture of the Channel 2 filter.

The second flight of the instrument occurred in August 1980, returning about 6.5 hours of useful scientific data. The sky region scanned in this flight is also shown in Figure 3.3 and Table 3.2. During the entire flight, the payload was fully commandable. Shortly after reaching float altitude, the null-magnetometer was found to develope a large constant offset error. The pointing error was readily corrected with an in-flight positional calibration, with very little loss of observing time. The flight was terminated before dawn when the payload reached the telemetry range limit. The payload landed in Western Texas. The altimeter signal, which enabled the pilot in a chase plane to determine the time of landing in the dark, was lossed due to an improperly buffered electronic circuit. As a result, the parachute was not detached in time, causing the payload to be dragged for a distance of about 600 m.

The outer gondola crash rings were broken off, but the instruments, protected by the sturdy inner gondola frame, remained intact.

Table 3.1 Observation Plan

DATE OF OBSERVATION (GREENWICH) : 15 NOV 1979
LONGITUDE OF PAYLOAD : 95D45M OS
LATITUDE OF PAYLOAD : 31D46M OS

GMT	LST	OBJECT	RA(79)	DEC(79)	AZM	ELV	AZMO	ELVO	RISE	SET
23 30	20.75	POLORIS	2 13 33	+89 10 39	0.96	31.87	-2.70	34.87	16.90	16.90
23 30	20.75	ALPHA PER	3 22 51	+49 47 20	42.07	18.14	38.85	21.14	20.92	15.18
23 30	20.75	CAPELLA	5 15 10	+45 58 36	33.42	1.04	30.41	4.04	23.28	16.56
23 30	20.75	ALPHA PSA	22 56 29	-29 44 6	149.63	21.01	146.35	24.01	21.00	6.27
23 30	20.75	VENUS	16 51 36	-23 14 48	232.97	11.70	229.87	14.70	14.55	0.52
23 45	21.00	GALACTIC L= 0.0	17 44 15	-28 55 34	222.72	13.56	219.59	16.56	15.73	1.10

DATE OF OBSERVATION (GREENWICH) : 16 NOV 1979
LONGITUDE OF PAYLOAD : 95D45M OS
LATITUDE OF PAYLOAD : 31D46M OS

GMT	LST	OBJECT	RA(79)	DEC(79)	AZM	ELV	AZMO	ELVO	RISE	SET
0 0	21.25	GALACTIC L=342.0	16 52 39	-43 40 27	221.48	-6.26	218.48	-3.26	15.90	23.03
0 15	21.50	GALACTIC L=348.0	17 12 11	-38 55 11	224.64	-2.60	221.64	0.40	15.81	23.23
0 30	21.75	GALACTIC L=354.0	17 29 11	-33 59 18	228.16	0.86	225.15	3.88	15.73	0.47
0 45	22.00	VENUS	16 46 14	-23 3 8	244.50	-2.83	241.50	0.17	14.38	0.33
1 0	22.25	GALACTIC L= 0.0	17 44 15	-28 55 34	234.11	1.59	231.10	4.59	15.67	1.00
1 15	22.50	GALACTIC L= 6.0	17 57 57	-23 46 10	238.36	4.52	235.34	7.52	15.62	1.53
1 30	22.75	GALACTIC L= 12.0	18 10 36	-18 32 36	242.88	7.25	239.83	10.25	15.53	2.02
1 45	23.00	GALACTIC L= 18.0	18 22 29	-13 16 2	247.62	9.79	244.54	12.79	15.53	2.45
2 0	23.25	GALACTIC L= 24.0	18 33 52	- 7 57 29	252.55	12.15	249.44	15.15	15.50	2.87
2 15	23.50	GALACTIC L= 30.0	18 44 58	- 2 37 49	257.64	14.35	254.49	17.35	15.47	3.23
2 30	23.75	GALACTIC L= 36.0	18 55 57	+ 2 42 11	262.84	16.41	259.66	19.41	15.42	3.69
2 45	0.01	GALACTIC L= 42.0	19 7 3	+ 8 1 51	268.14	19.37	264.93	21.27	15.38	4.09
3 0	0.26	ALPHA LYR	18 36 12	+38 45 55	302.52	22.94	299.19	25.94	13.22	5.20
3 0	0.26	GALACTIC L= 48.0	19 18 26	+13 20 23	273.43	20.26	270.22	23.26	15.35	4.52
3 15	0.51	GALACTIC L= 54.0	19 30 20	+18 36 56	278.64	22.11	275.52	25.11	15.30	4.95
3 30	0.76	GALACTIC L= 60.0	19 42 59	+23 50 29	284.19	23.95	280.83	26.95	15.27	5.42
3 45	1.01	GALACTIC L= 66.0	19 56 42	+28 59 51	289.49	25.93	286.07	28.93	15.22	5.99
4 0	1.26	GALACTIC L= 72.0	20 11 51	+34 3 27	294.73	27.78	291.23	30.78	15.15	6.43
4 15	1.51	GALACTIC L= 78.0	20 28 53	+39 59 13	299.86	29.84	296.29	32.84	15.09	7.07
4 30	1.76	GALACTIC L= 84.0	20 48 26	+43 44 19	304.89	32.02	301.22	35.02	14.99	7.62
4 45	2.01	GALACTIC L= 90.0	21 11 16	+48 14 49	309.76	34.36	305.99	37.36	14.87	8.70
5 0	2.26	L=195, B=+5	7 4 34	+18 15 30	92.83	24.30	79.46	27.30	2.92	11.47
5 15	2.51	ORION A	5 36 1	- 6 0 10	122.07	31.93	118.41	34.93	2.48	13.95
5 30	2.76	ROSETTE	6 24 1	+ 3 29 49	107.27	31.62	103.62	34.62	2.83	15.15
5 45	3.01	ORION B	5 46 1	- 1 0 9	121.87	39.01	117.64	42.01	2.43	14.35
6 0	3.26	MARS	10 2 24	+14 1 42	71.98	-2.22	68.98	0.78	6.08	19.25
6 15	3.52	W. ROSETTE	6 0 1	+ 3 29 50	121.21	45.02	116.72	48.02	2.48	14.75
6 30	3.77	MON R2	6 0 1	- 7 30 10	134.94	39.35	130.88	42.25	2.95	14.28
6 45	4.02	NGC 2264	6 32 1	+10 59 27	112.30	49.48	107.37	52.48	2.70	15.60
7 0	4.27	MARS	10 2 24	+14 1 42	79.71	10.17	76.62	13.17	6.02	19.25
7 8	4.40	JUPITER	10 38 35	+ 9 34 20	79.96	1.97	76.95	4.97	6.82	19.65
7 15	4.52	GALACTIC L= 96.0	21 38 20	+52 25 10	321.52	17.39	318.32	20.29	14.67	8.80
7 30	4.77	GALACTIC L=102.0	22 10 42	+56 7 48	323.75	21.26	320.46	24.36	14.70	11.25
7 45	5.02	GALACTIC L=108.0	22 49 18	+59 12 10	325.51	25.45	322.10	28.45	13.42	13.42
8 0	5.27	GALACTIC L=114.0	23 34 22	+61 26 4	326.74	29.64	323.18	32.64	14.17	14.17
8 15	5.52	MARS	10 2 24	+14 1 42	89.17	26.06	85.74	29.06	6.03	19.25
8 23	5.65	JUPITER	10 38 35	+ 9 34 20	89.67	17.87	86.45	20.87	6.82	19.65
8 30	5.77	GALACTIC L=120.0	0 24 38	+62 36 53	327.60	32.18	325.93	35.18	15.08	15.08
8 45	6.02	GALACTIC L=126.0	1 16 54	+62 36 23	327.24	36.45	323.05	39.45	15.08	15.82
9 0	6.27	GALACTIC L=132.0	2 7 5	+61 24 37	326.05	40.64	321.91	43.64	16.72	16.72
9 15	6.52	GALACTIC L=138.0	2 52 5	+59 9 57	323.90	44.67	319.45	47.67	17.46	17.46
9 30	6.77	W 3	2 25 40	+61 47 24	326.24	50.24	322.21	42.24	17.03	17.03
9 45	7.02	JUPITER	10 38 35	+ 9 34 20	101.42	35.25	97.60	38.25	6.82	19.65
9 53	7.16	PERSEUS CLUSTER	3 19 4	+41 28 27	299.07	43.43	294.71	46.43	21.72	14.13
10 0	7.28	GALACTIC L=144.0	3 30 40	+56 4 55	319.43	44.35	315.00	47.35	19.65	16.52
10 15	7.53	GALACTIC L=150.0	4 2 57	+52 21 54	314.63	47.34	309.93	50.34	21.10	15.22
10 30	7.78	GALACTIC L=156.0	4 29 57	+48 11 11	308.70	49.73	303.75	52.73	22.20	15.02
10 45	8.03	JUPITER	10 38 35	+ 9 34 20	112.68	47.47	107.97	50.47	6.82	19.65
10 53	8.16	COMA CLUSTER	12 58 25	+28 3 56	72.93	28.50	69.42	31.50	8.27	22.88
11 0	8.28	VIRGO CLUSTER	12 29 30	+12 29 52	93.14	29.22	89.58	32.22	8.55	21.63
11 15	8.53	GALACTIC L=162.0	4 52 40	+43 40 28	301.88	45.92	297.21	48.92	23.08	15.90
11 30	8.78	GALACTIC L=168.0	5 12 11	+38 55 12	294.94	46.29	290.34	49.29	23.83	15.80
11 45	9.03	GALACTIC L=174.0	5 29 11	+33 59 18	287.84	45.81	283.28	48.81	0.47	15.73
12 0	9.28	GALACTIC L=180.0	5 44 18	+28 55 36	280.90	44.51	276.45	47.51	1.03	15.68

Table 3.2 List of Field Centers Surveyed

Flight #1, Nov 15/16 1980

Raster #	GMT	Source	RA(1979)	Dec(1979)
	$23^h 50^m$		$16^h 51^m 36^s$	$-23^d 14^m 48^s$
1	23 59	Venus	16 51 36	-23 14 48
2	0 19	$\ell = 0°$	17 44 15	-28 55 34
3	0 37	Venus	16 51 36	-23 14 48
4	0 51	$\ell = 0°$	17 44 15	-28 55 34
5	1 10	$\ell = 6°$	17 57 57	-23 46 10
6	1 31	$\ell = 12°$	18 10 36	-18 32 36
7	1 46	$\ell = 18°$	18 22 29	-13 16 02
8	2 4	$\ell = 24°$	18 33 52	- 7 57 29
9	2 20	$\ell = 30°$	18 44 58	- 2 37 49
10	2 39	$\ell = 36°$	18 55 57	2 42 11
11	2 56	$\ell = 42°$	19 07 03	8 1 51
12	3 12	$\ell = 48°$	19 18 26	13 20 23
13	3 28	$\ell = 54°$	19 30 20	18 36 56
14	3 46	$\ell = 60°$	19 42 59	23 50 29
15	4 2	$\ell = 84°$	20 48 26	43 44 19
16	4 21	Orion A	5 36 1	- 6 0 10
17	4 39	Rosette	6 24 1	3 29 49
18	4 56	Orion B	5 46 1	- 1 0 9
19	5 8	Orion B	5 40 0	- 2 0 0
20	5 25	W. Rosette	6 1 1	3 29 50
21	5 42	Mon R 2	6 6 0	- 6 30 0
22	5 59	NGC 2264	6 39 59	9 55 0
23	6 17	Mars	10 4 41	13 51 14
24	6 29	ℓ=195° b=5°	7 4 32	18 15 42
25	6 45	ℓ=195° b=5°	7 4 32	18 15 42
26	7 2	Jupiter	10 39 9	9 31 23
27	7 16	Jupiter	10 39 9	9 31 23
28	7 26	Orion A	5 36 1	- 6 0 10
29	7 45	W3	2 25 40	61 47 24
30	8 3	W3	2 25 40	61 47 24
31	8 20	Mars	10 4 41	13 51 14
32	8 33	Jupiter	10 39 9	9 31 23
33	8 46	Coma Cl.	12 58 25	28 4 9
34	9 5	$\ell = 264°$	8 48 29	-43 44 6
35	9 22	$\ell = 270°$	9 11 19	-48 14 32
36	9 43	Moon	12 59 8	- 2 50 44
37	10 1	Moon	12 59 8	- 2 50 44
38	10 16	Moon	12 59 8	- 2 50 44
39	10 28	Taurus Cld.	4 31 33	24 19 37
40	10 46	$\ell = 276°$	9 38 23	-52 24 50
41	11 2	$\ell = 282°$	10 10 45	-56 7 17
42	11 19	Saturn	11 43 37	3 54 43
43				

Table 3.2 (Cont'd)

Flight #2 August 15, 1980

Raster #	GMT	Source	RA(1979)	Dec(1979)
	$2^h\ 0^m$		$11^h\ 5^m\ 7^s$	$6^d\ 59^m\ 32^s$
1	2 14	Jupiter	11 47 15	3 38 33
2	2 29	Saturn	12 44 30	- 0 22 0
3	2 54	Moon	17 44 18	-28 55 35
4	3 9	$\ell = 0°$	16 41 43	-45 57 49
5	3 20	$\ell = 339°$	16 41 43	-45 57 49
6	3 38	$\ell = 339°$	16 59 28	-42 6 40
7	3 56	$\ell = 344°$	17 15 9	-38 6 27
8	4 12	$\ell = 349°$	17 29 10	-33 59 15
9	4 31	$\ell = 354°$	17 44 18	-28 55 35
10	4 50	$\ell = 0°$	16 25 20	-24 22 39
11	5 12	ρ Oph. Cld.	15 52 56	- 2 50 26
12	5 29	L 134 Cld.	17 41 53	-29 46 39
13	5 47	$\ell = 359°$	17 53 34	-25 29 51
14	6 04	$\ell = 4°$	2 7 8	61 24 48
15	6 22	$\ell = 132°$	2 52 8	59 10 7
16	6 40	$\ell = 138°$	1 16 56	62 36 35
17	6 59	$\ell = 126°$	18 14 40	-16 47 19
18	7 5	$\ell = 14°$	18 14 40	-16 47 19
19	7 21	$\ell = 14°$	18 4 25	-21 9 49
20	7 42	$\ell = 9°$	4 29 56	48 11 6
21	8 00	$\ell = 156°$	5 12 13	38 55 9
22	8 21	$\ell = 168°$	18 45 4	- 2 37 39
23	8 38	$\ell = 30°$	19 30 26	18 37 13
24	8 59	$\ell = 54°$	6 33 10	19 28 4
25	9 10	Venus	6 33 10	19 28 4
26	9 15	Venus	6 33 10	19 28 4
27		Venus		

Table 3.3 Sample Ground Station Display

DATE: 11/16/79 TIME: 3:15: 4

SCIENCE DATA

POINTING DATA
RA 1° HR 15 MN 25 SEC
DEC 1500.52 MN 51 SEC
TR AZ 279.1 DEG
EL 16.1 DEG 16.0
LAT 31.2 DEG
LONG 93.7 DEG WEST
DLAT -0.23DEG/HR
DLONG -0.37DEG/HR
LSIDT 0 HR 38 MN 30 SEC

ACS STATUS

DEWAR STATUS
DET A RES 6.35 V
DET B RES 7.52 V
DET C RES 4.47 V

DET A LOCKIN 55.
DET B LOCKIN 36.
DET C LOCKIN 80.
ASPECT -1.

CHOPPER STATUS
AMPLITUDE 3396.
PHASE

ASPECT
CAMERA STATUS

FRAME COUNT 510

COMMAND NO IN EXEC
MAG DEV 5.9
NULL MAG 273.2

CMD STATUS DA00
LAST CMD RCD FAF3
RELAY STATUS 0469
RASTER FLAG FFFF

BAL ALTITUDE FT GMT 3:14:59 DATE 11/16/79

DATE: 11/16/79 TIME: 3:47: 5

HOUSEKEEPING DATA

TEMP(C)		CURRENT				VOLTAGE	
		STRONGBACK					
ELECTR	0.3	REG+15	0.4	GYR HT	0.1	REG+15	15.3
CHOPER	-20.1	REG-15	-0.1	GYRO	0.6	REG-15	-15.5
CAMERA	10.2	REG+ 5	0.7			REG+ 5	4.9
DEWAR	-19.8	STG HT	1.4			GY+-15	2.7
TELSCP	-39.4	CH +28	0.9			GY+-26	2.7
GYRO	2.2					GY+ 28	29.2
GYRO E	3.0						
		GONDOLA					
BATT 1	8.1	BATT 1	13.7	MOM WH	-9.7	BATT 1	29.6
BATT 2	29.1	BATT 2	0.5	REG+15	1.3	BATT 2	29.6
ELECTR	19.5	ELC HT	0.5	REG-15	-0.7	28V BS	28.2
LT EL	-1.5	LT EL	0.7	REG1+5	5.0	REG+15	14.6
RT EL	-12.5	RT EL	0.3	REG2+5	6.5	REG-15	-14.9
DITHER	7.1	DITHER	0.2			REG1+5	5.4
MOM WH	2.4					REG2+5	5.3
						D BIAS	0.0

ALTITUDE 742. FT

FIGURE CAPTIONS

Figure 3.1: Azimuth-elevation maps showing the celestial position and orientation of the Galactic equator as a function of local sidereal time at a latitude of 32°. These maps were used in flight planning for selecting the portion of Galactic plane that was accessible at a favorable orientation (plane inclined more than 45° to the cross elevation scans). The first map shows the Galactic equator at 2-hour interval between 0 and 10 hour local sidereal time; and the second between 12 and 22 hour. Only the portion of the plane with elevation angle between 0° and 60° is accessible for observation with the balloon-borne telescope.

Figure 3.2a: A sample 6° x 6° raster-scan pattern on the sky in equatorial coordinates showing the location and orientation of the Galactic equator. The raster lines are along the cross elevation direction. Adjacent scan lines are separated by 8 arcmin in elevation. Each raster box contains a total of 44 scan lines.

Figure 3.2b: Azimuth and elevation position of a region to be scanned as a function of time.

Figure 3.3: An equatorial coordinates map showing the regions surveyed in the first (lined) and second (dotted) flights of the submillimeter observatory. Coordinates are in right ascension and declination. The heavy solid line is the Galactic equator. Raster scans of contiguous 6° x 6° fields were made in the enclosed regions, with multiple scans of some fields. In addition, scans were made of Venus, Mars, Jupiter, Saturn, and the Moon to characterize instrument performance.

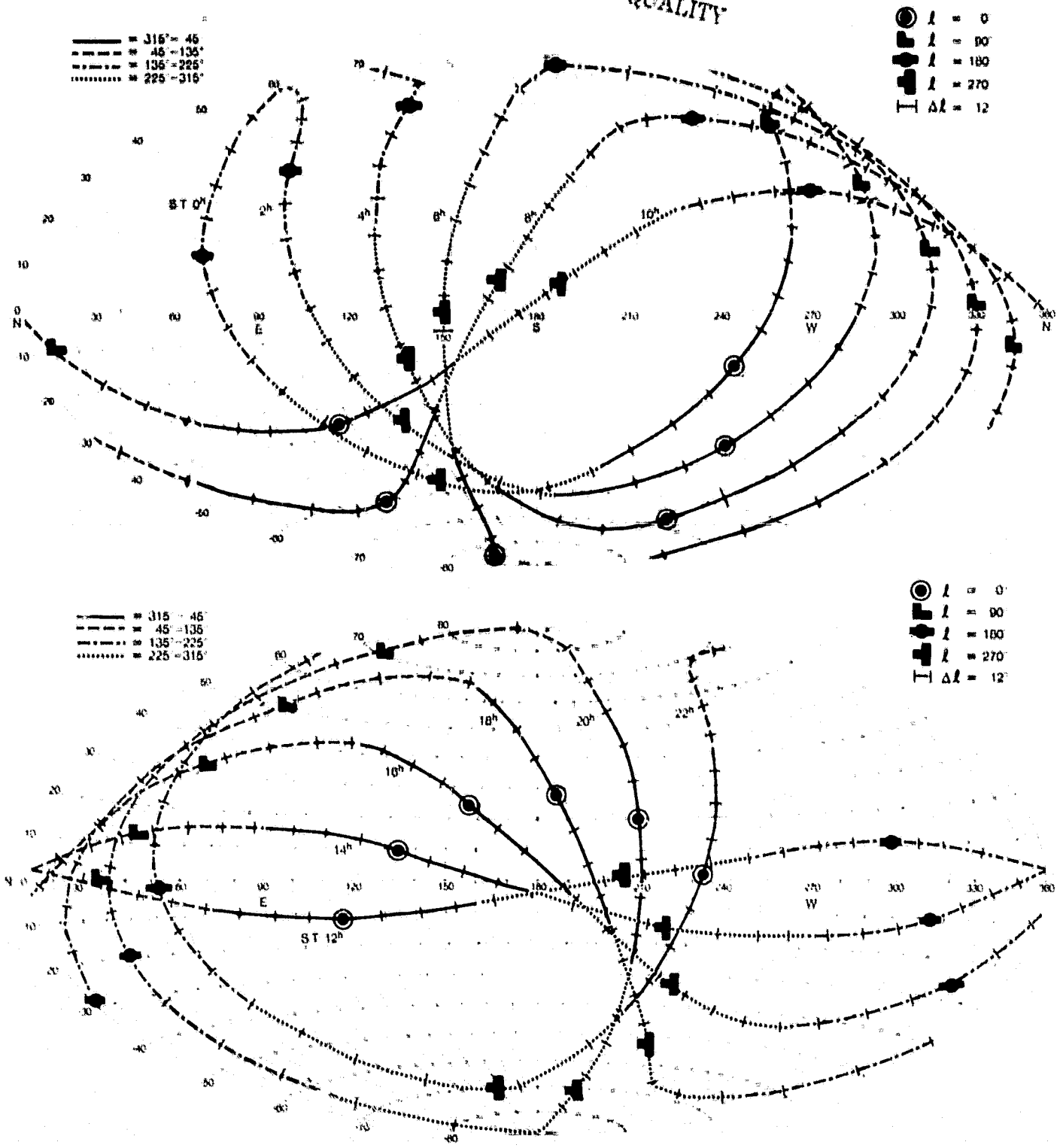

Figure 3.1

Figure 3.2

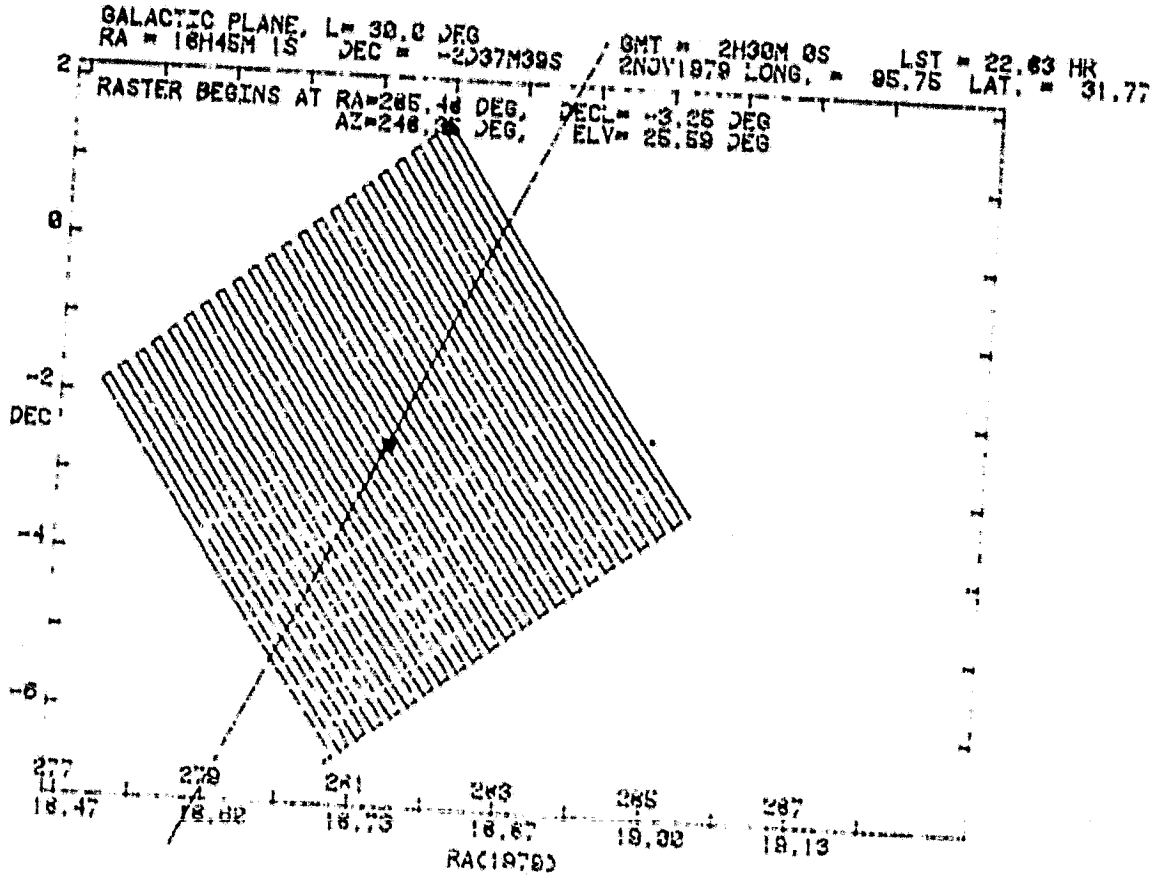
GALACTIC PLANE, L= 30.0 DEG
RA = 18H45M 1S DEC = -2D37M39S
GMT = 2H30M 0S LST = 22.63 HR
2NOV1979 LONG. = 95.75 LAT. = 31.77
RASTER BEGINS AT RA=285.4d DEG, DECL= -3.25 DEG
AZ=248.3 DEG, ELV= 25.59 DEG
2
0
-2
-4
-6
DEC
277
18.47
279
18.52
281
18.73
283
18.87
285
19.00
287
19.13
RA(1979)

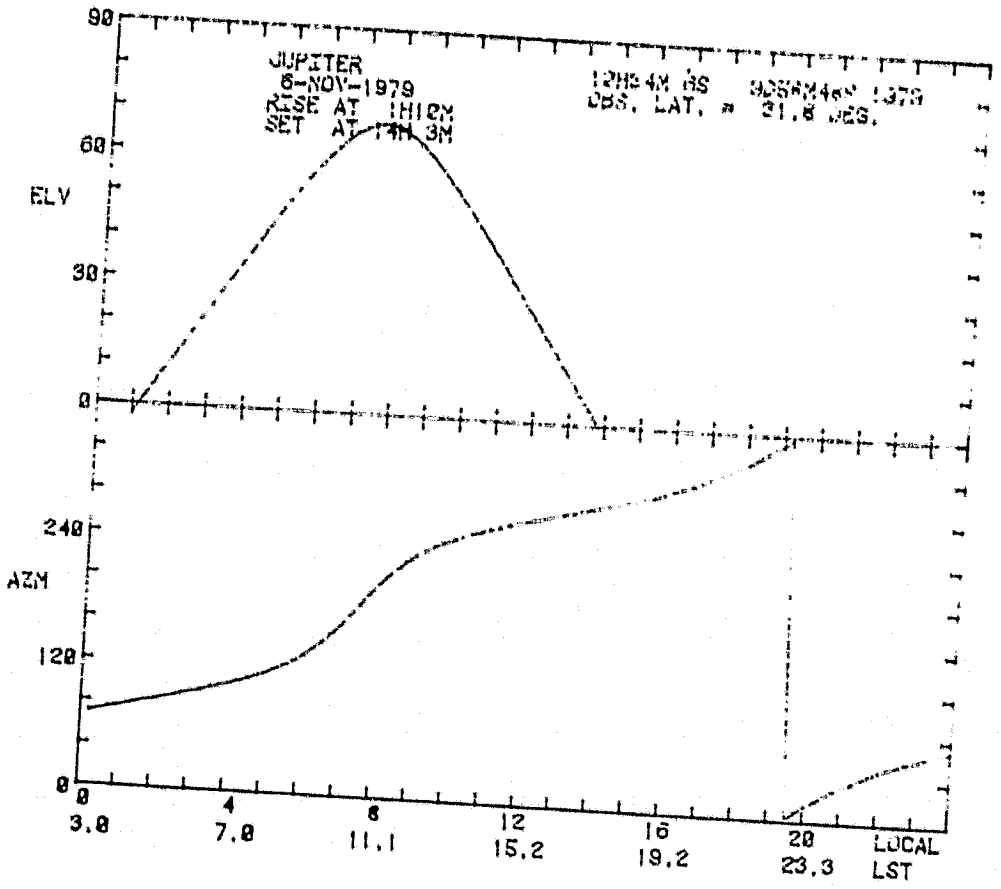
JUPITER
6-NOV-1979
RISE AT 1H12M
SET AT 14H 3M
90
60
30
0
ELV
240
120
0
AZM
0
3.8
4
7.8
8
11.1
12
15.2
16
19.2
20
23.3
LOCAL
LST

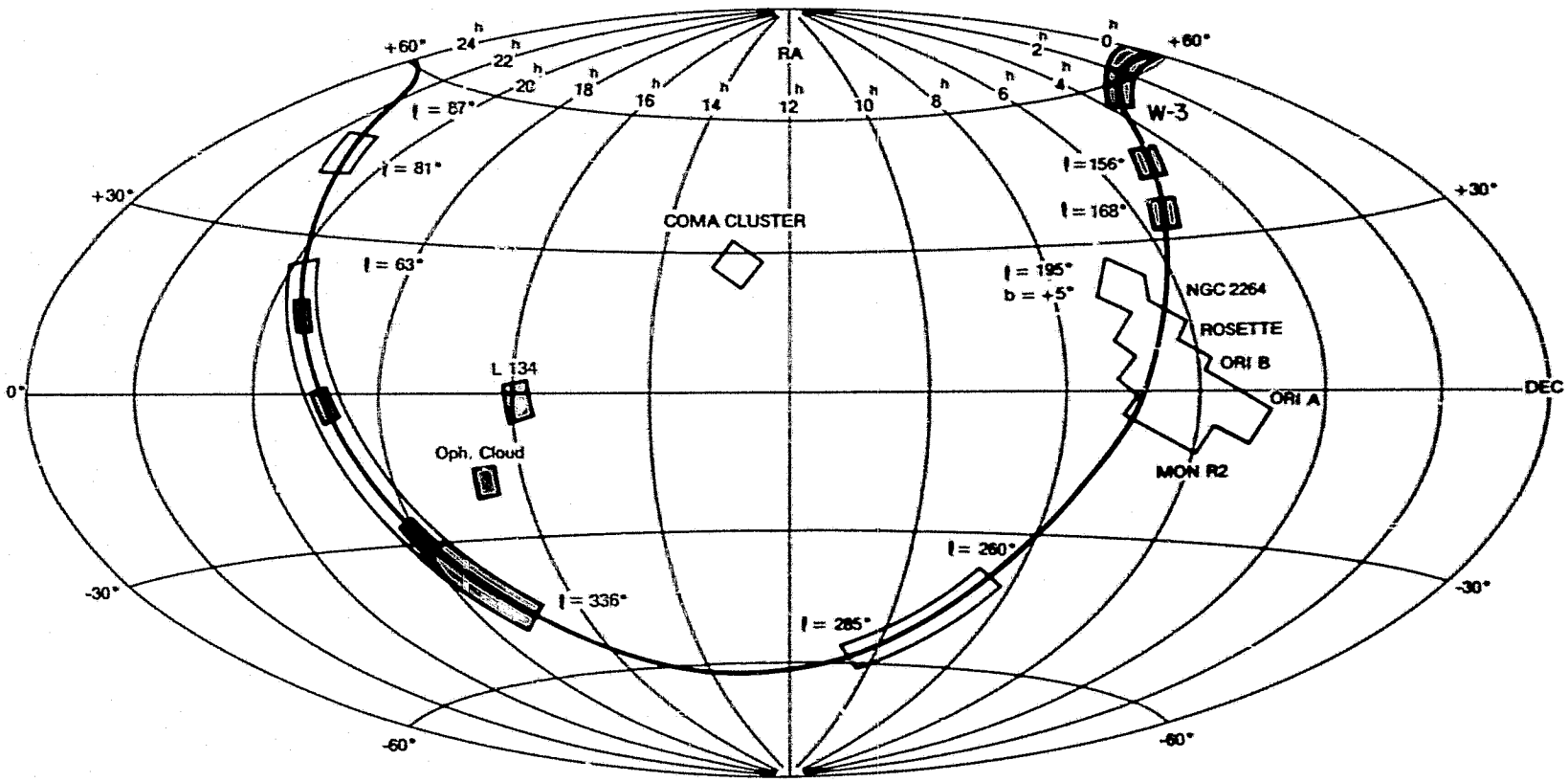
+60°
24 h
22 h
20 h
18 h
16 h
14 h
RA
12 h
10 h
8 h
6 h
4 h
2 h
0 h
+60°
l = 87°
l = 81°
W-3
l = 156°
l = 168°
+30°
COMA CLUSTER
+30°
l = 63°
l = 195°
b = +5°
NGC 2264
ROSETTE
ORI B
L 134
ORI A
DEC
0°
Oph. Cloud
MON R2
l = 260°
-30°
l = 336°
l = 285°
-30°
-60°
-60°

CHAPTER 4 DATA REDUCTION

4.1 DATA FORMAT AND PROCESSING SOFTWARE

The scientific and engineering data from the survey instrument are transmitted in real time and recorded at the ground station at Palestine, Texas. There is no provision for on-board data storage. The data collected from the various sensors (IR and Si detectors, voltage, temperature sensors, azimuth and elevation encoders, etc.) are organized in 16 different channels, each channel containing data words from one or more type of sensors. The data words are sampled in integral multiple time intervals of 1/160 second. The signal voltage of each of the three infrared detectors is encoded in 2 8-bit words, while most of the engineering data are encoded in a 8-bit word. A 1/10 second length of data, synchronized to one complete chopper cycle and containing 256 8-bit words, forms a data frame. Some of the words in a data frame are sub-commutated to contain several infrequently sampled engineering data. An on-board microprocessor is used to format both the scientific and engineering data for serial transmission to the Consolidated Instrument Package (CIP) supplied by NSBF. The data is then pulse-code modulated (PCM) and telemetered to the ground station where it is recorded on analog tapes in real time.

The data was also received in real time by the ground station LSI-11 computer. The contents of the analog tapes are digitized and recorded on 9 track digital tapes after the flight. Nine digital tapes, together with a 200-ft roll film and auxiliary data from NSBF (payload altitude and position log), form the raw data product for the first flight of the balloon package.

A flow chart of the data processing procedures used for reducing the data in this thesis is shown in Figure 4.1. The first few steps in the processing utilize the software written by Stier (1979) and his collaborators. This software was originally developed for the balloon instrument at the Harvard-Smithsonian Center for Astrophysics. These steps include the reformatting of the data, computation of the phase of the infrared signals, and phase-synchronous demodulation of the chopped infrared signals. Following these processing steps, I wrote the remaining software for restoring the raster scan lines, determining the telescope aspect, and providing scientific analysis of the data.

4.2 PHASE SYNCHRONOUS DEMODULATION

In infrared astronomical observations at wavelengths longer than a few microns, the radiation from astronomical objects is often several orders of magnitude fainter than the thermal blackbody emission from the telescope and the atmosphere. A standard procedure to observe this small signal buried in a bright background is to switch the telescope beam back and forth between the source and an adjacent field of sky, thereby modulating the source signal at a fixed frequency. The AC-coupled detector output then contains the signal of interest as well as a lot of noise at many frequencies and phases whose amplitudes are most likely much higher than the signal. The process of retrieving this modulated source signal is called phase synchronous demodulation, or lock-in filtering. In this process, the detector data stream is multiplied by a periodic reference signal (such as a sine or square wave having similar waveform as the signal) at the chopper frequency with phase close to the bolometer signal. The product is then passed through a low-pass filter (integrated in time). The output is a slowly varying term which is proportional to the amplitude and to the cosine of the phase difference between the reference signal and the detector signal. Non synchronous inputs (noise) that share no common frequencies with the reference signal will contribute very little DC

component to the output. The lock-in filter thus acts as a narrow bandpass filter that also rejects out-of-phase synchronous signals. The equivalent band width of the lock-in filter is determined by the time constant T of the low pass filter.

The digital implementation of the lock-in filter used in this thesis is given by Stier (1979). The bolometer offset signal due to thermal imbalance of the instrument is used for determining the phase of the infrared signal relative to the chopper cycle defined by the position transducer outputs. This phase information is obtained from the sine and cosine terms of the fundamental frequency component of the chopper amplitude and the bolometer signal. This relative phase angle is then used as an input to determine the time offset in the starting point of a reference cosine wave at the chopper frequency.

The detector signal is sampled 16 times in each chopper period of 0.1 second. This signal is multiplied by the reference cosine wave approximated by 16 discrete numerical values per cycle. The products in a time interval of an integral number of chopper periods are added together. In the present case, a two-cycle integration time is chosen. This time interval corresponds to about half the transit time of a point source. The equation of the lock-in filter

may be represented by:

$$S = 1/\tau \int_0^\tau v(t) \cos(\omega_o t + \phi)\, dt$$
$$\approx (\Delta t/\tau) \sum_{n=1}^{32} v(t_n) \cos(\omega_o t_n + \phi)$$

where S is the demodulated signal, τ is the integration time (= 0.2 sec, or 2 periods), v(t) is the detector signal at time t, $\omega_o/2\pi$ = 10 Hz is the chopping frequency and ϕ is the phase of the cosine wave relative to the chopper. Because the data is sampled every 1/160 second, the integral is replaced with a finite series at discrete times $t_n = n\Delta t$, where $\Delta t = 2\pi/16\omega_o$.

The response of this filter to input signal of frequency ω is obtained by setting $v(t) = e^{i\omega t}$:

$$H(\omega) = (\Delta t/\tau) \sum_{n=1}^{32} e^{i\omega t_n} \cos(\omega_o t_n + \phi)$$

The amplitude of the frequency response of this filter is shown in Figure 4.2.

An improved version of this digital lock-in filter has been designed by a colleague, R. F. Silverberg, but was not implemented in time for this thesis. In this new version, instead of varying the phase ϕ in the reference signal to match that of the detector signal, the origin of the time in

the data stream is adjusted to make $\phi = 0$. This is done because a reference wave equal to cos $(\omega_o t)$ provides a better rejection of low frequency noise components and the frequency response is then independent of ϕ. In addition, the data is integrated over 4 chopper cycles, but the effective bandwidth of the system is kept equal to that of a 2-chopper-cycle integration by windowing the reference cosine wave with a Hamming window apodizing function of the form:

$$w(t_n) = 0.54 + 0.46 \cos(2\pi(n-32)/N-1)$$

where n = 1 to N, with N = 64 (4 chopper cycle). The lock-in filter output is then equal to:

$$S = \sum_{n=1}^{64} v(t_n)\ w(t_n) \cos\ (\omega_o t_n)$$

where the origin of t_n is chosen to match the phase of the reference signal. Preliminary assessment indicates that this lock-in filter provides a factor of 2.5 improvement in noise rejection over the version used in this thesis.

4.3 RESTORATION OF INFRARED SCANS

In the submillimeter survey, the observations were made in a raster scanning mode at a rate of 20 arc minutes per second, with a 10 Hz wobbling secondary mirror switching between two fields of the sky separated by 20 arc minutes in the scanning direction. The output of the detector, after synchronous demodulation, is proportional to the gradient in the sky brightness. To restore the sky brightness, I used the integration-type algorithm discussed by Simon (1976).

Each data point in the output from the lock-in filter used was that for a 0.2 second sample or 2 chopper-cycle length of data. The separation between adjacent data points is then approximately 4 arc minutes. As this sampling interval is smaller than one beam throw, the data stream is partitioned into 5 independent data sets, each as an independent input set to Simon's algorithm. Five subsets were chosen because the separation between the positive and negative beams is nearly equal to 5 times the separation between adjacent data points. To further reduce high frequency noise, a three-point running average was made on the data stream before partitioning. This produces a spatial correlation extending up to 12 arc minutes, which is comparable to one beam width and is not expected to alter significantly the appearance of the final contour maps.

A constant of integration in each restored line equal to zero was assumed. This is justified in most scan lines where either the starting or ending positions are about 3 degrees from the Galactic equator where the sky brightness is expected to be small. A consequence of this assumption is that this survey is not sensitive to any isotropic radiation which may be of considerable astrophysical interest. The presence of bright sources at the beginning or end of a scan line is reflected in the presence of negative flux levels in the output of the restoration process. These scan lines were rejected from the final data product, although a judicious re-definition of the constant of integration could remove this anomaly. Fortunately, these lines occur infrequently and mostly at the beginning and end of a raster field where redundant scan lines at a different time and starting position are sometimes available. At regions which have been redundantly scanned, the restored scan lines are usually consistent with each other to within statistical uncertainties.

4.4 ASPECT DETERMINATION

The telescope attitude was determined both in real time and more accurately in post-flight data analysis. The real time attitude information was provided by a null magnetometer and a shaft angle encoder on the elevation axis. The value of these encoder outputs was updated every 1/10 second and transmitted to the ground station. The conversion of the raw data into azimuth and elevation was performed by the ground station computer, using conversion factors obtained from pre-flight calibration. This information provided a real time display of the pointing direction and contributed to a very versatile and efficient operation of the observatory.

During ground check-out, calibrations of the null magnetometer and elevation shaft encoder were made using a theodelite. The theodelite readings were calibrated by observations of a few bright stars. The calibration of the magnetometer was done in an isolated field away from major steel structures. The magnetic bearing was converted into geographic bearing using a model of the Earth's magnetic field (Barraclough et al. 1975). Because of the changing position of the balloon in flight, it was necessary to update the magnetic deviation in real time. The uncertainty in azimuth is estimated to be about 1/2 degree. The

uncertainty in elevation is about 0.2 degrees. During flight operations, additional offset errors may have arisen because of a different magnetic environment and a slightly different vertical reference due to slightly different weight loading. The overall uncertainty for in-flight pointing accuracy is estimated to be about 1/2 degree, as was verified when bright, known objects such as planets were easily acquired at the expected location. This uncertainty is acceptable for source acquisition purposes in survey observations in which fields of angular size of 6 x 6 degrees^2 were raster-scanned.

In presenting the survey data, a positional uncertainty of a fraction of the field of view is desirable. A 35 mm camera coaligned with the telescope and a photodiode sensor sharing the focal plane with the infrared detectors provide additional information for post-flight aspect reconstruction. The camera, a Robot 35 mm camera with a 35 mm lens and a 200 ft film magazine, took one picture for every raster scan line during which the shutter opens and closes six times, giving a streak pattern of the star field. In principle, one could identify the stars on the photograph for each raster line to determine the pointing direction. This is an extremely tedious and time consuming job best reserved for occasional sampling purposes. I have developed a simpler and satisfactory approach by using a combination

of the photodiode star sensor together with the outputs of the null-magnetometer, elevation shaft angle encoder, cross elevation and elevation gyro rates. A flow chart of this procedure is shown in Figure 4.3.

The first step of this procedure is to get a good calibration of the null-magnetometer and elevation encoder. The star sensor signals obtained in most raster fields were used for this purpose. Knowing the rough azimuth and elevation of the telescope at the time of a star transit, the approximate RA and Dec of the star was computed and compared with the star positions in the American Emphemeris and Nautical Almanac. Once an identification was made, the correct azimuth and elevation of the telescope at the time of star transit is known, which is then used to derive the offset error in the magnetometer and elevation encoder. A number of stars were sighted during the entire flight, and an offset plot showing the difference between the true positions and the raw encoder positions is shown in Figure 4.4. The remarkable feature is that the azimuth offsets appear to be locally constant with large deviations occuring at two places separated by about 180 degrees in azimuth. This suggests that the effect may be related to the particular magnetic property of the magnetometer or the gondola structure. The elevation offsets are rather constant in all positions. The-peak-to-peak scatter of the

offset in azimuth (except at the anomalies) and elevation is about 0.2 degree. These systematic offset components appear to be correctable.

The azimuth and elevation encoder outputs, after being corrected for the systematic offset errors, are still unsatisfactory in two respects. The random noise in the magnetometer readout is rather large, typically with peak-to-peak amplitude of about 0.2 to 0.3 degrees on short time scales of 0.1 second or longer. The elevation shaft angle encoder, which uses the gondola frame as a local vertical reference, was sensitive to slight pendulum motion. On a longer time scale, however, the stability of these encoders was extemely good.

In contrast, the gyroscope rates in the cross elevation and elevation axes provide very accurate short term (< 1 minute) information which is unaffected by gondola pendulum motion about these two axes. By integrating the gyro rate, one could then get very good relative position readouts on a short time scale. The accuracy, however, is eventually limited by the long term drift of the gyroscope.

The complementary properties of the gyroscope and the attitude encoders can therefore be combined to provide position readout that is accurate on a time scale of seconds

and stable over a period of a raster of about 15 minutes. The long term stability of the magnetometer and the elevation encoders provide the references for evaluating and correcting for the systematic gyro drift. A plot of the gyro drift in several rasters is shown in Figure 4.5. The gyro drift is predominantly linear in time, with small higher-order deviations. The total drift is about 1 degree in a time interval of approximately 15 minutes. The gyro drift was fitted with a third-order polynomial and fed back into the integrated gyro position. This corrected gyro position is then combined with the photodiode star sensor to provide an absolute positional readout. The offset of the infrared channels relative to the star sensor was determined by observations of planets, which are bright infrared and visible objects. The final uncertainty in the absolute position is estimated to be typically less than 0.1 degree. At some locations this uncertainty is as small as about 3 arc minutes as derived from additional star sightings. A conservative estimate of the uncertainty is about 1/2 of the instantaneous field of view of our photometer.

FIGURE CAPTIONS

Figure 4.1: Flow chart showing the major steps in the data processing for the survey results presented in this thesis.

Figure 4.2: The response of the digital lock-in filter used in this thesis to an input signal of unit amplitude at frequency f. The reference signal is a 10-Hz cosine wave represented by 16 discrete numerical coefficients per cycle. The integration time is 2 chopper periods.

Figure 4.3: Flow chart showing the steps involved in the determination of telescope aspect. The positional uncertainty obtainable with this method is typically less than 0.1 arc degree, and may be as good as 3 arcmin at some locations.

Figure 4.4: The offsets in azimuth and elevation between the optical axis of the photodiode star sensor and the nominal aspect of the telescope mount as a function of azimuth angle, determined by comparing the readouts of the magnetometer and elevation encoder with the celestial positions of identified stars at the time of sightings.

Figure 4.5: The long term drift in the positional readout of the gyroscope in the elevation and azimuth direction during one raster scan. The gyro drift rate and direction were approximately constant during the time when the data for this thesis were taken.

DATA PROCESSING FLOW CHART

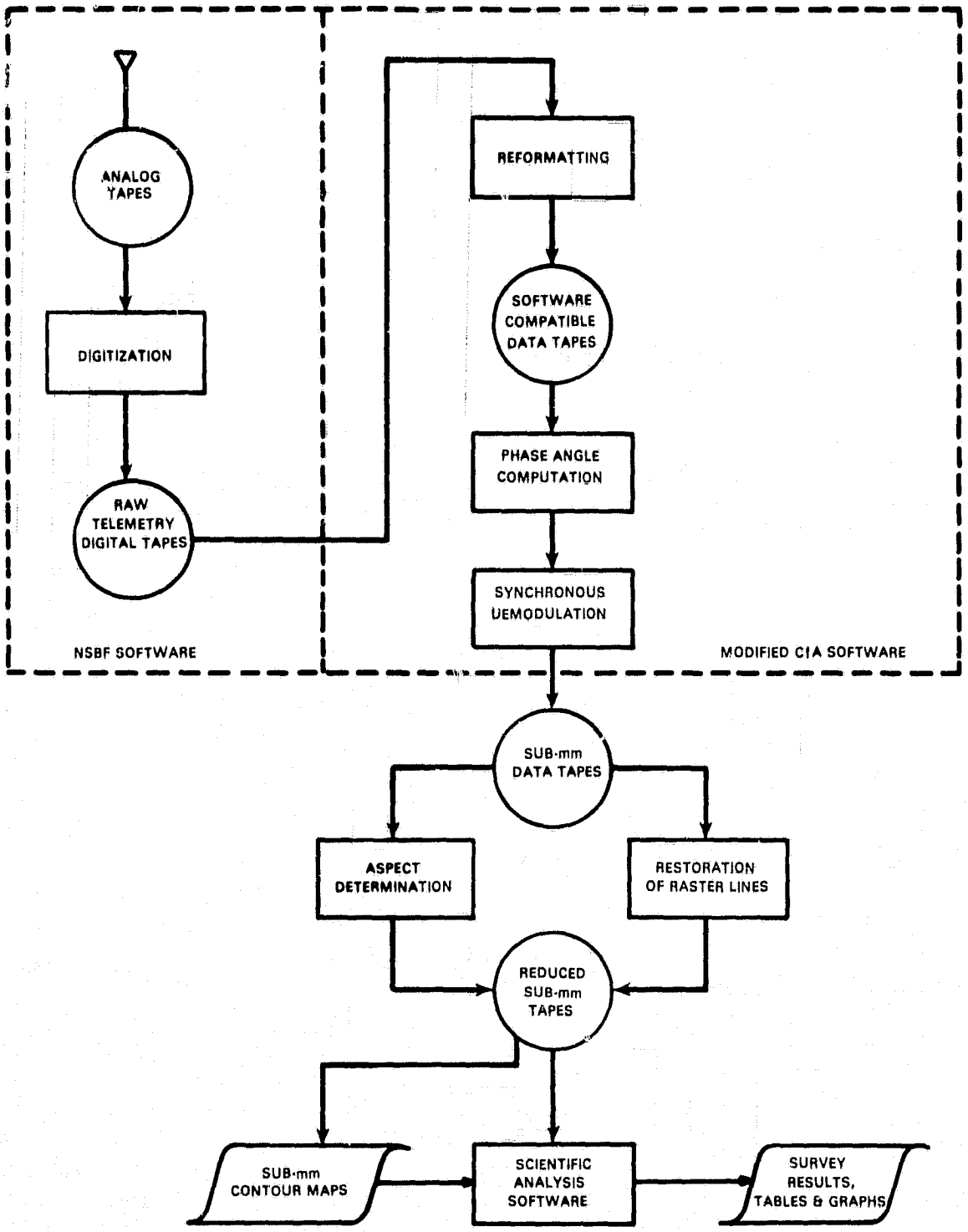

FIGURE 4.1

C-2

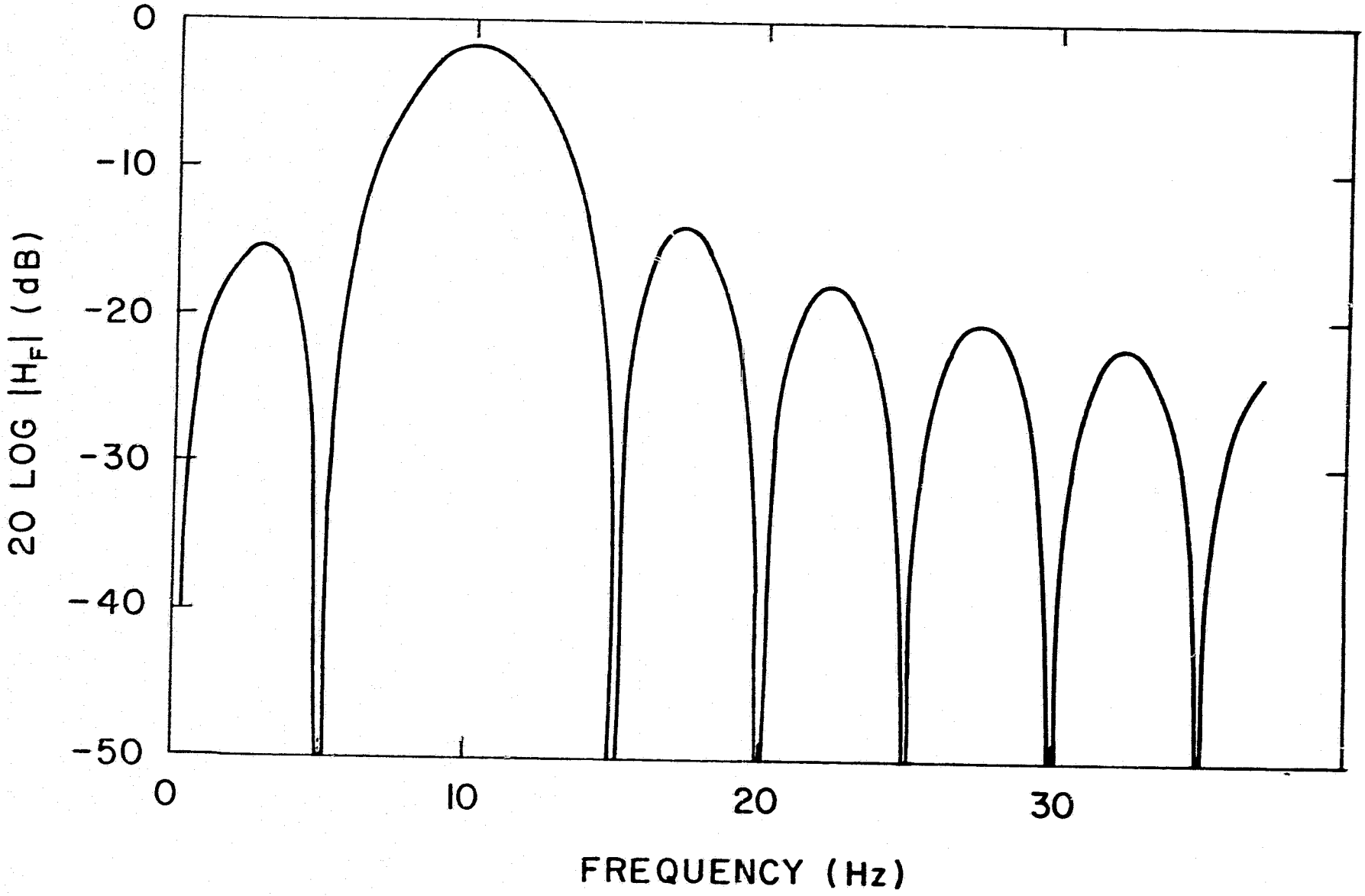

FIGURE 4.2

ASPECT DETERMINATION FLOW CHART

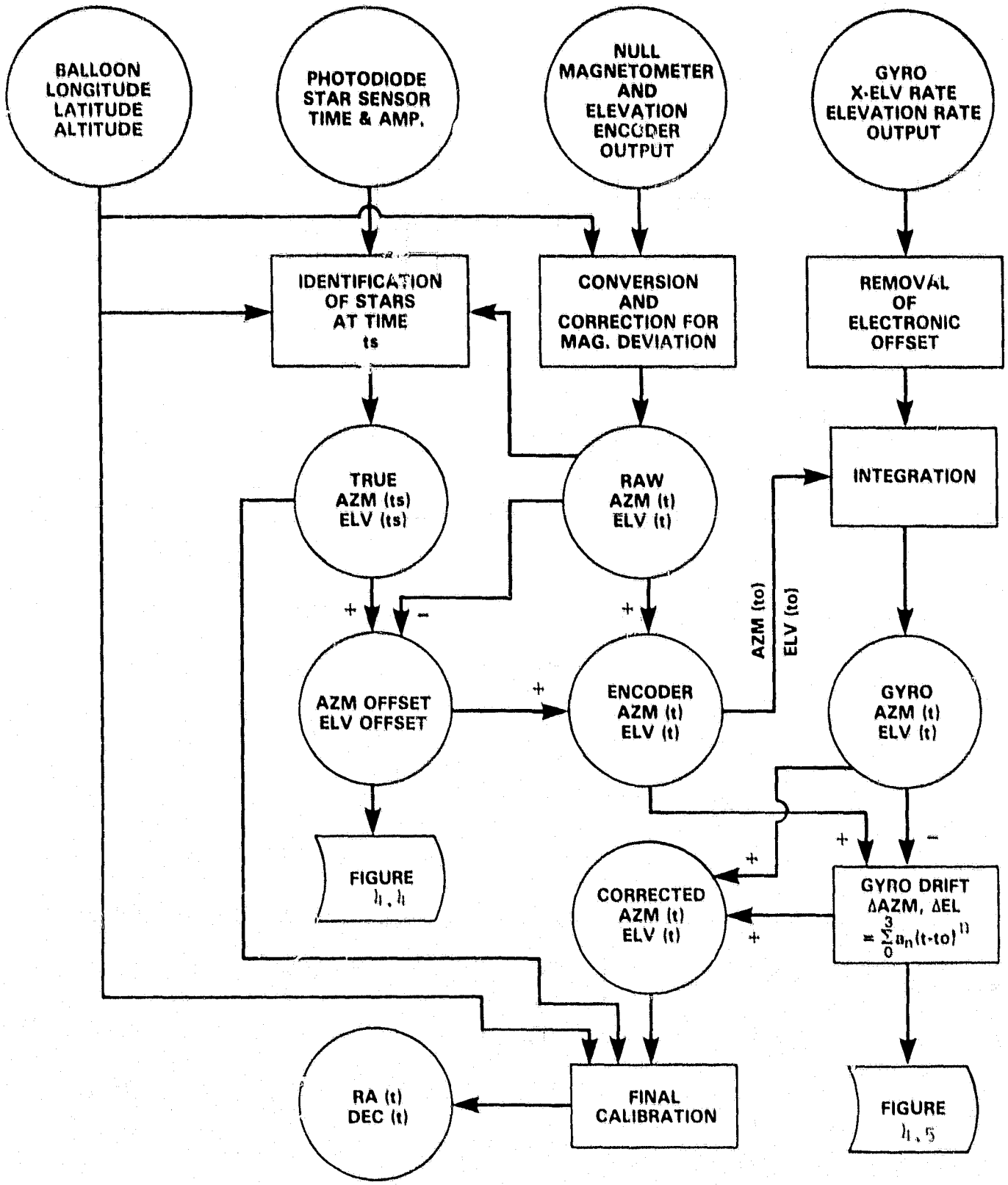

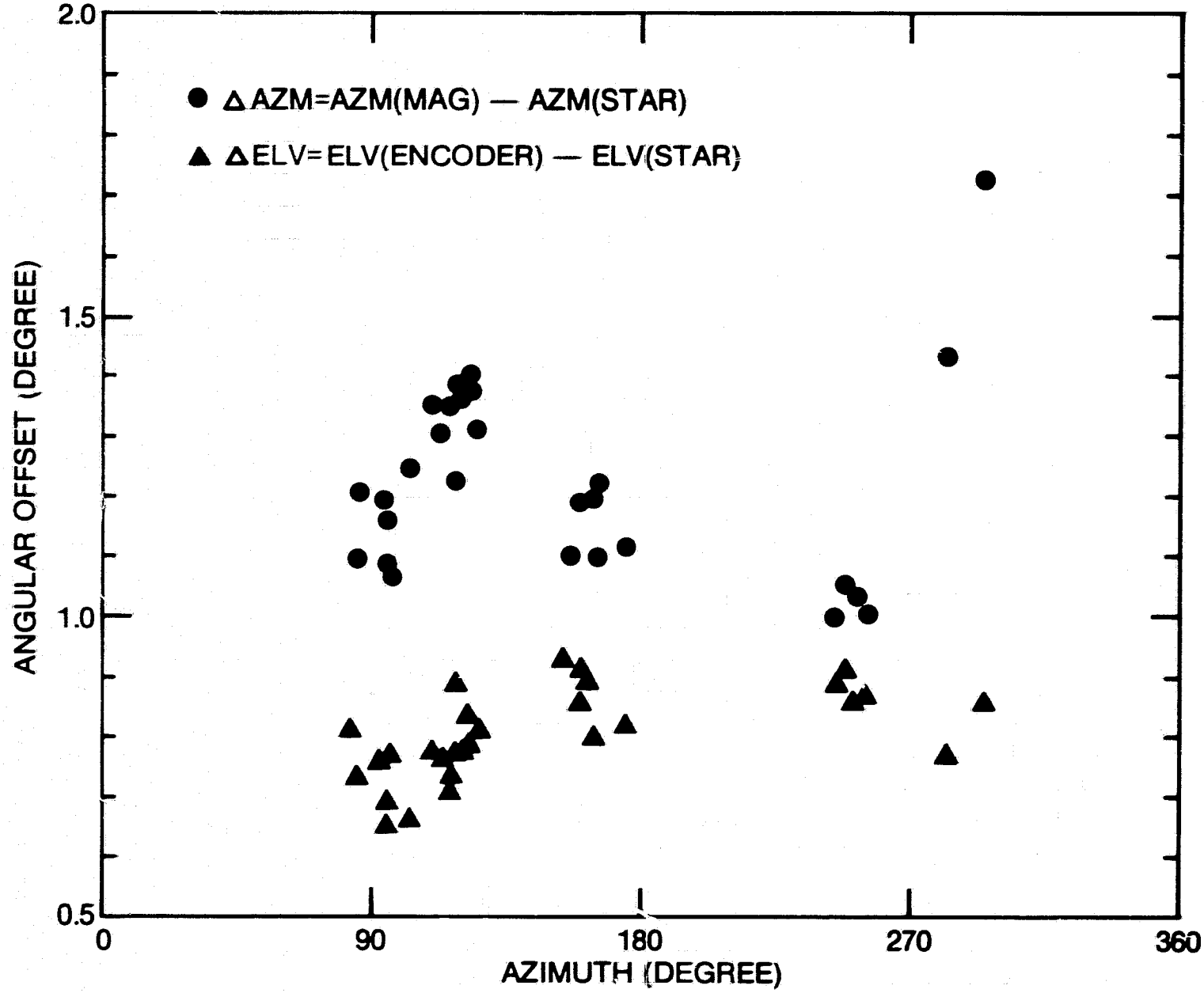
2.0
1.5
1.0
0.5
ANGULAR OFFSET (DEGREE)
● ΔAZM=AZM(MAG) — AZM(STAR)
▲ ΔELV=ELV(ENCODER) — ELV(STAR)
0
90
180
270
360
AZIMUTH (DEGREE)

FIGURE 4.4

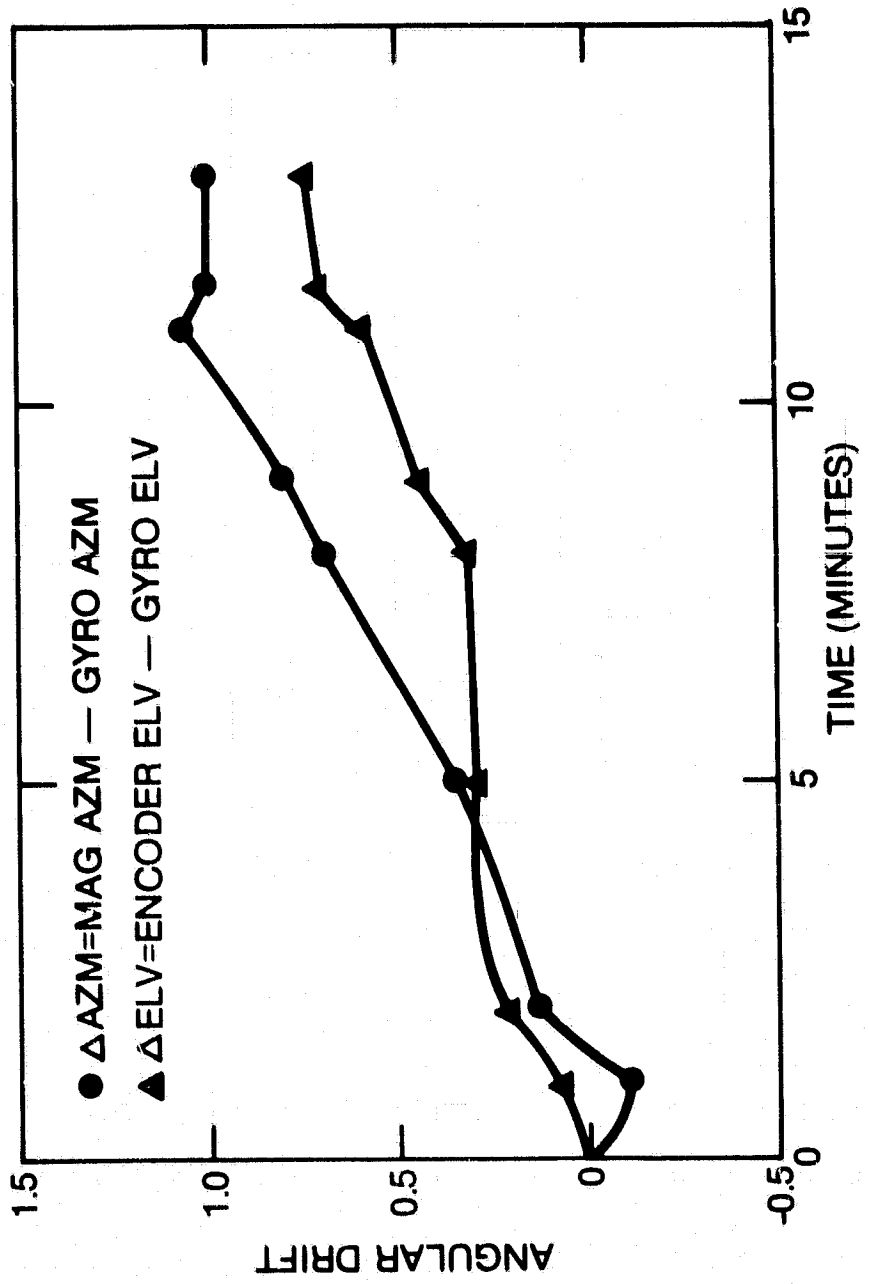
● ΔAZM=MAG AZM — GYRO AZM
▲ ΔELV=ENCODER ELV — GYRO ELV
ANGULAR DRIFT
1.5
1.0
0.5
0
-0.5
0
5
10
15
TIME (MINUTES)

FIGURE 4.5

CHAPTER 5 PHOTOMETRIC SENSITIVITY

5.1 PHOTOMETRIC CALIBRATION

The primary means of calibrating the submillimeter photometer was through frequent in-flight observations of planets. During the first flight in November 1979, Venus, Mars and Jupiter were repeatedly observed and detected. Saturn was also been observed at the end of the flight but the data were lost due to frequent telemetry dropouts. The Venus observations were made before reaching float altitude when the detector sensitivity and atmospheric transmission were still changing. Only the Mars and Jupiter observations were used for photometric calibrations.

A strip chart record of a Jupiter scan is shown in Figure 5.1. Here one can see the chopper-modulated signals in the three wavelength bands. The signals in the three channels are separated in time because the field of view of the detectors are spaced by about 17 arcmin along the elevation direction. The bipolar signature of the signals is due to the scanning of a chopping double beam; i.e., the differential nature of the observation. This signature, together with the time separation of the detector signals in the three channels, provides an extremely effective means of discriminating real signals from spurious noise glitches

that appear simultaneously in all three channels.

In the following analysis, it is assumed that the size of the planet image underfills the aperture at the focal plane. This assumption is supported by a higher resolution profile of the Jupiter scan in Figure 5.2. For a planet with mean disk brightness temperature T_p at submillimeter wavelength and angular size Ω_p, a normalized photometer spectral response g_ν, and atmospheric transmission t_ν, the incident power from the planet is:

$$P_p = A\Omega_p \int B_\nu(T_p)\, g_\nu\, t_\nu\, d\nu \qquad \text{(watt)} \qquad (1)$$

With a detector signal voltage of V_p from the planet, the ratio P_p/V_p then serves as a power conversion scale for calibrating other astronomical objects. For another source with signal V_s, the associated incident power is:

$$P_s = V_s\, P_p/V_p \qquad \text{(watt)} \qquad (2)$$

The above conversion is applicable on the condition that the bolometer response is linear. Laboratory measurements show that the linearity condition is satisfied under an observing environment where the chopper-modulated infrared radiation is much smaller than the DC background radiation.

If the source uniformly fills the telescope beam Ω_t, the source radiance is defined as:

$$I_s = P_s / A\Omega_t \quad (w\ m^{-2}\ sr^{-1}) \tag{3}$$

For most observed dust clouds, the spectrum resembles that of a diluted blackbody with a characteristic temperature of a few tens of kelvin. At submillimeter wavelengths covered by our three channels, the source emission decreases rapidly with increasing wavelength so that the effective bandwidth is narrower than the instrumental bandwidth. It is often convenient to define a flux-weighted mean frequency and an effective bandwidth for a broad-band system as:

$$c/\lambda_{eff} = \nu_{eff}$$

$$= \int \nu\ B_\nu(T)\ g_\nu\ t_\nu\ d\nu \ /\ \int B_\nu(T)\ g_\nu\ t_\nu\ d\nu \tag{4}$$

The equivalent spectral bandwidth is defined as:

$$\Delta\nu = \int B_\nu\ g_\nu\ t_\nu\ d\nu \ /\ t_{\nu eff}\ B_{\nu eff} \tag{5}$$

The spectral radiance from the source at the effective frequency is related to the radiance by:

$$S_{\nu eff} = I_s / \Delta\nu \qquad (w\ m^{-2}\ sr^{-1}\ Hz^{-1}) \tag{6}$$

A common unit often used by infrared and radio astronomers is the spectral flux density:

$$F_{\nu eff} = S_{\nu eff}\, \Omega_t \qquad (w\ m^{-2}\ Hz^{-1} = 10^{26}\ Jy) \qquad (7)$$

The fundamental quantity that is measured in the submillimeter survey is the incident power on the detector. The other quantities in equations (3) through (7) are derived parameters. The values of S_ν, F_ν, ν_{eff}, and $\Delta\nu$ are all dependent on the assumed temperature and spectrum of the source.

The calibration of the submillimeter photometer system is based on the measured spectral response g_ν of the photometer shown in Figure 2.11 and an assumed mean disk temperature of 125 K for Jupiter (Wright 1976). The calibration conversion factors and the system noise equivalent fluxes for the three wavelength channels are listed in Table 5.1. The effective wavelengths for the three channels as a function of blackbody temperature are calculated and plotted in Figure 5.3. It can be readily seen that the effective wavelength of the photometer is a sensitive function of temperature for $T < 50$ K. For a source temperature of 30 K, the effective wavelengths were 190, 305, 360 μm for the three channels in the first flight.

For higher source temperature, the effective wavelengths approach the asymoptotic values of 147, 276, and 330 μm.

5.2 STATISTICAL UNCERTAINTIES

The statistical uncertainties in the photometric calibration are random fluctuations or noise in the measured signal. The noise may arise from a number of sources including detector noise, microphonic vibration noise, fluctuation in the chopper amplitude and hence infrared offset signal, and power surges in the electronics system. This combined noise signal sets a limitation on the sensitivity and resolution of the photometer.

The noise associated with each data point within a finite time interval is calculated by finding the r.m.s. fluctuation in the detector signal at the position where the telescope is known to be pointing at blank sky. Since the infrared photons originate mainly from the atmosphere, telescope and other instrument surfaces, the r.m.s. noise measured at the blank sky position is assumed to be the same as that measured at the source position except for increased photon noise. Defining the noise voltage as:

$$V_n = (\Sigma(v_i - \langle v \rangle)^2/N)^{1/2} \qquad (8)$$

where v_i is the amplitude of the infrared signal after synchronous demodulation and $\langle v \rangle$ is the mean signal of N data points. If each data point v_i is sampled once every Δt

seconds, the effective bandwidth for the measurement is $\Delta f = 1/2\Delta t$. The noise signal per unit bandwidth is

$$N_n = (V_n^2/\Delta f)^{1/2} = V_n/\Delta f^{1/2} \qquad (9)$$

The noise equivalent radiance, NER, defined as the equivalent radiance in one hertz bandwidth (1/2 second integration time) that would yield a signal-to-noise ratio of 1 is:

$$NER = N_n/A\Omega \times P_p/V_p \qquad (w\ m^{-2}\ sr^{-1}\ Hz^{-1/2}) \qquad (10)$$

The noise equivalent flux density is:

$$NEFD = \Omega\ NER/\Delta\nu \times 10^{26} \qquad (Jy\ Hz^{-1/2}) \qquad (11)$$

where P_p and V_p are the power and signal received from a calibration source such as a planet. The values of the NER and NEFD are listed in Table 5.1.

5.3 SYSTEMATIC UNCERTAINTIES

The systematic uncertainties in the photometric calibration set a limitation on the absolute photometric accuracy of the survey results. These uncertainties may affect different segments of the data to varying extents, or may affect the entire data set uniformly. The estimated systematic uncertainty from sources that are accountable is about 15 %. However, there are in addition a few other uncertainties that cannot be reliably estimated, so that the actual systematic uncertainty could be considerably higher. Some of these systematic uncertainties and the estimated values are described in the following paragraphs.

A) Variation of bolometer responsivity in flight.

The responsivity of the bolometer is the signal response per unit incident power. The responsivity may fluctuate during the time in between calibration observations of planets or other well known sources. The fluctuations arise mainly due to a change in the bolometer temperature, which may be caused by a change in the helium vapor pressure due to varying float altitude of the telescope package, or by a change in the background atmospheric radiation at low elevation angles. A bolometer

DC voltage monitor circuit for each of the three photometric channels provides the means for determining the change in resistance whereby the responsivity change may be estimated. The DC resistance variations in the three bolometers were determined to be typically less than 2 % during the time interval in which the data in this thesis were taken. In addition, an altimeter on the payload provides frequent ambient pressure readouts from which the temperature of the liquid helium bath may be derived. A plot of the helium bath temperature versus time during the flight is shown in Figure 5.4. The data for this thesis was obtained in the first 2 hours after reaching float altitude when the helium temperature was estimated to have varied between 1.71 to 1.72 kelvin. The calibration observations of Jupiter were made at the time when the bath temperature was at about 1.74 K. The variation in bolometer responsivity due to this range of temperature change is probably less than 3 %, as determined from a responsivity vs temperature plot (Figure 5.5) experimentally determined in the laboratory, where the responsivity $S \propto T^{-1}$ to $T^{-3/2}$. This variation in responsivity was judged to be negligible compared with other sources of uncertainties and was not corrected for in the data analysis.

The responsivity variation due to change in background loading at low elevation angles (< 3 degree) is probably

larger than 5 %. If the infrared offset signal is mainly caused by a thermal imbalance in the telescope structure that is independent of elevation angle, the responsivity of the detector scales directly with the amplitude of this offset signal. This provides a means of estimating the responsivity change. An offset signal decrease of as much as 20 % was observed for the scan lines at elevation below 0 degree. For the data presented in this thesis, none of the scans were made at an elevation much lower than 5 degrees. Above this angle, the background loading on the bolometers was very stable.

B) Uncertainty in the planet brightness temperature.

Jupiter was used as the primary photometric calibration standard for our observations. The assumed disk brightness temperature is 125 K in the submillimeter bands. This assumed brightness temperature is within the estimated range of 127±3 K in the 30-300 μm band, and 121 K in the 125-300 μm band (Wright, 1976). The latter value is the reconciled brightness temperature based on the assumed value of 150 K of Armstrong et al., (1972). This nominal bightness temperature is consistent with more recent observations (Harper et al., pre-published data) and theoretical modeling results (Hanel et al., 1980). Since the flux from Jupiter

is linearly proportional to temperature, an error of 10 to 15 K, typical of the uncertainty in the brightness temperature, translates into a systematic calibration error of about 8 to 12 %.

C) Uncertainty in the spectral response of the photometer.

The spectral response of the detector and associated filter optics was measured in the laboratory using a Fourier transform spectrometer (Nicolet FTS 7000). The measurements were made repeatedly with reproducible results to within variations in the relative transmission of typically less than 5 %. The wavelength scale of the spectrometer, which determines the cut-on wavelenghths of the photometer, was measured accurately by counting laser interference fringes. The relative spectral calibrations were based on the assumption of a flat spectral response of the reference detector system. The validity of this assumption has not been verified, so that the potential uncertainty in the spectral calibration could be higher.

D) Uncertainty in the atmospheric transmission.

Model calculations of atmosphere transmission at an altitude of 29 km have been made by Traub and Stier (1976).

Their results indicate a transmission very close to 100 % in the submillimeter bands. In particular, the estimated average transmission in the 40-250 μm band as a function of air mass η is:

$$\langle t_\nu \rangle \approx 0.99 - 3.3 \times 10^{-3}\ \eta \qquad (12)$$

Using this equation as a guide, the average transmission in the submillimeter bands is probably > 95 % at elevation angles higher than 5 degrees. I adopt $\langle t_\nu \rangle = 1$ in analysing the data presented in this thesis. The error incurred due to this assumption is probably less than 5 %.

E) Baseline Uncertainty

With a spatial-scan, double-beam instrument, the detector signal is proportional to the emission gradient across the sky. Restoration of the source emission using an integration type algorithms requires an assumption on the extended background emission distribution or baseline of the photometric system. Most of the scan lines in this survey start at $b \approx 3$ degrees, so that an argument may be made that the starting fields are probably free of strong extended emission. This is by no means certain, and the restored scan lines may contain varying amounts of

uncertainty in the baseline level. The baseline uncertainty is expected to be small compared with the peak fluxes associated with bright emission peaks, but may be of considerable astrophysical interest.

The extended source restoration process using an integration algorithm can also introduce an instrumental baseline error. Noise glitches or drifts in instrumental background emission at one end of a raster line may get propagated throughout the entire line. This effect may be noticeable in some areas in the contour maps presented in Figure 6.1, where some of the extended spurs and valleys along the scanning and beam-switching direction may be attributed to baseline drift or noise glitches. The types of anomalies are probably insignificant at the higher contour levels.

5.4 PHOTOMETRIC PERFORMANCE

The design goal for the submillimeter survey photometric sensitivity is an NEFD of less than 100 Jy $Hz^{-1/2}$ for all three spectral bands. Laboratory calibrations of the detector system alone indicated that this goal could be adequately met. The observed photometric sensitivity based on actual in-flight calibration using Jupiter as standard turns out to be a factor of 4 to 9 worse than the design goal. Further investigation of the photometric performance revealed that the degraded sensitivity is due to a combination of excess noise and a smaller than estimated optical efficiency in the photometer/telescope interface. The noise in flight was approximately a factor of three higher than that measured in the laboratory, while the optical efficiency was only about 14 % instead of the estimated value of about 50 %. The estimated optical efficiency of 50 % was based on the measured light cone beam profile efficiency of 70 % and on the assumed 90 % reflectivity each at the primary, secondary and dichroic mirror surfaces.

The increase in noise may in part be explained by inadequate out-of-band rejection in the digital lock-in filter used in the analysis of the data presented here, especially if the bolometers possess excessive 1/f type

noise. An improved version of the digital lock-in filter has been designed by a colleague, R. F Silverberg. Preliminary assessment indicated that a factor of 2.5 reduction in noise may be achievable in the shortest wavelength channel. If this improvement is applicable to the other channels as well, the observed NEFD listed in Table 5.1 would have to be revised downward to 350, 270, and 190 Jy $Hz^{-1/2}$ for the three channels respectively. None of the reported flux values for the submillimeter emission sources nor the conclusions of this thesis need to be changed. Instead, some of the arguments may be further strengthened by the improved signal to noise ratio.

TABLE 5.1 Photometric Sensitivity Summary

Flight #1

	CHANNEL 1	CHANNEL 2	CHANNEL 3
$V_{Jupiter}$ (data unit)	990	292	264
$P_{Jupiter}$ (watt)	3.05×10^{-9}	5.92×10^{-10}	3.84×10^{-10}
N_n (data unit $Hz^{-1/2}$)	4.4	2.8	2.4
NEP (w $Hz^{-1/2}$)	1.35×10^{-11}	5.68×10^{-12}	3.48×10^{-12}
NER (w m^{-2} sr^{-1} $Hz^{-1/2}$)	1.43×10^{-6}	5.98×10^{-7}	3.67×10^{-7}
λ_{cut-on} (50 %) (μm)	110	230*	270
λ_{eff} (125 K) (μm)	152	281	334
$\Delta\nu$ (125 K) (Hz)	1.34×10^{12}	7.36×10^{11}	6.51×10^{11}
NEFD (Jy $Hz^{-1/2}$) (preliminary)	890	680	470
NEFD (Jy $Hz^{-1/2}$) (improved)	350	270	190
Minimum Detectable Flux (Jy)	350	270	190

* λ_{cut-on} for Channel 2 was 160 μm in Flight #2.

FIGURE CAPTIONS

Figure 5.1: A strip chart record of a scan across Jupiter. The bipolar signatures reflect the scanning double-beam nature of the measurements. The signals in the three channels are separated in time because the field of view of the three detectors are separated by about 17 arc minutes along the elevation direction.

Figure 5.2: High resolution profiles of the beam pattern in the three submillimeter bands. The FWHM beamwidths are about 10 arcmin.

Figure 5.3: The flux-weighted effective wavelengths for the three broad band submillimeter channels.

Figure 5.4: Pressure and liquid helium bath temperature profile during the first flight of the survey instrument.

Figure 5.5: Relative responsivity of the bolometers as a function of liquid helium bath temperature.

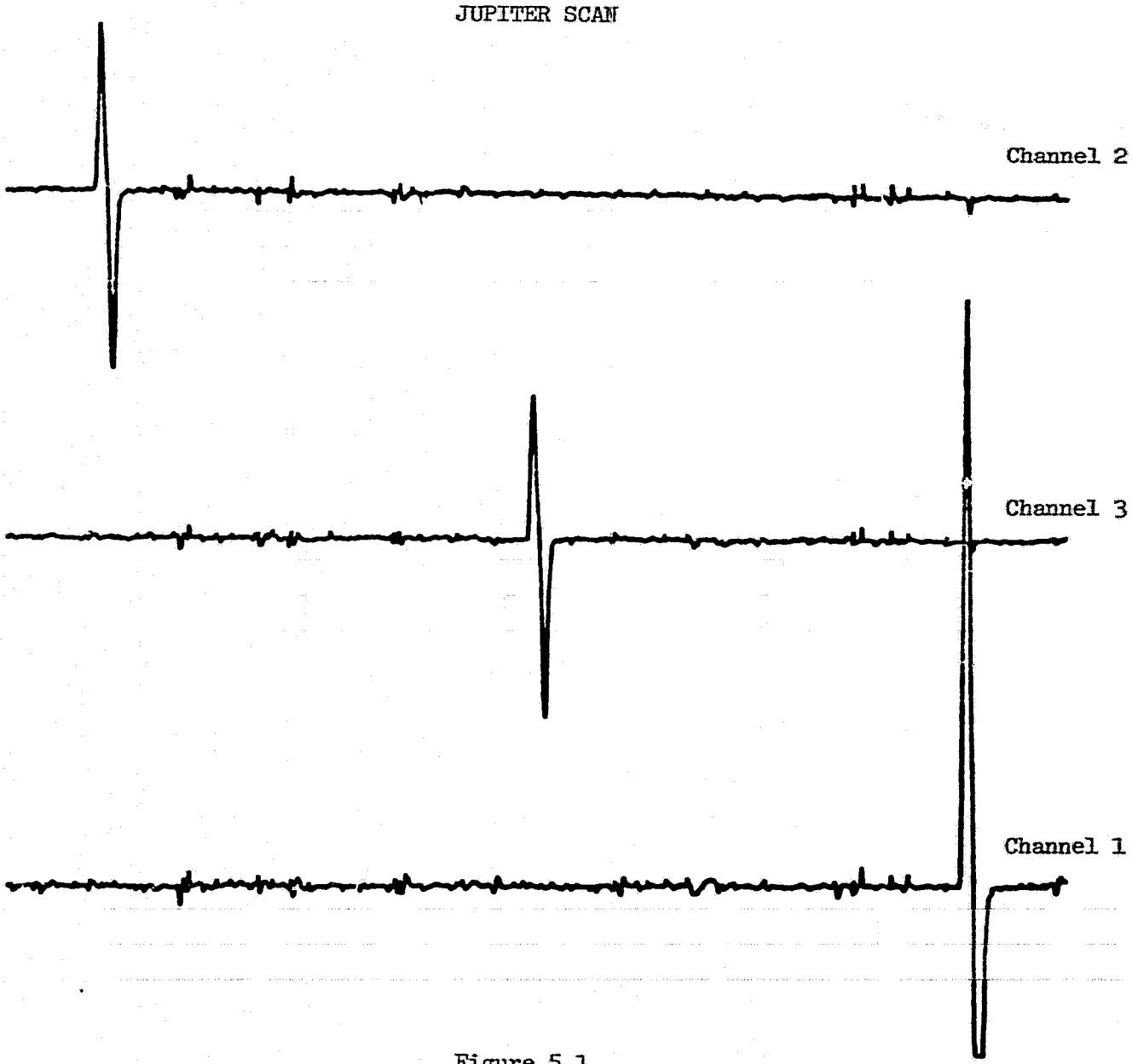

Figure 5.1

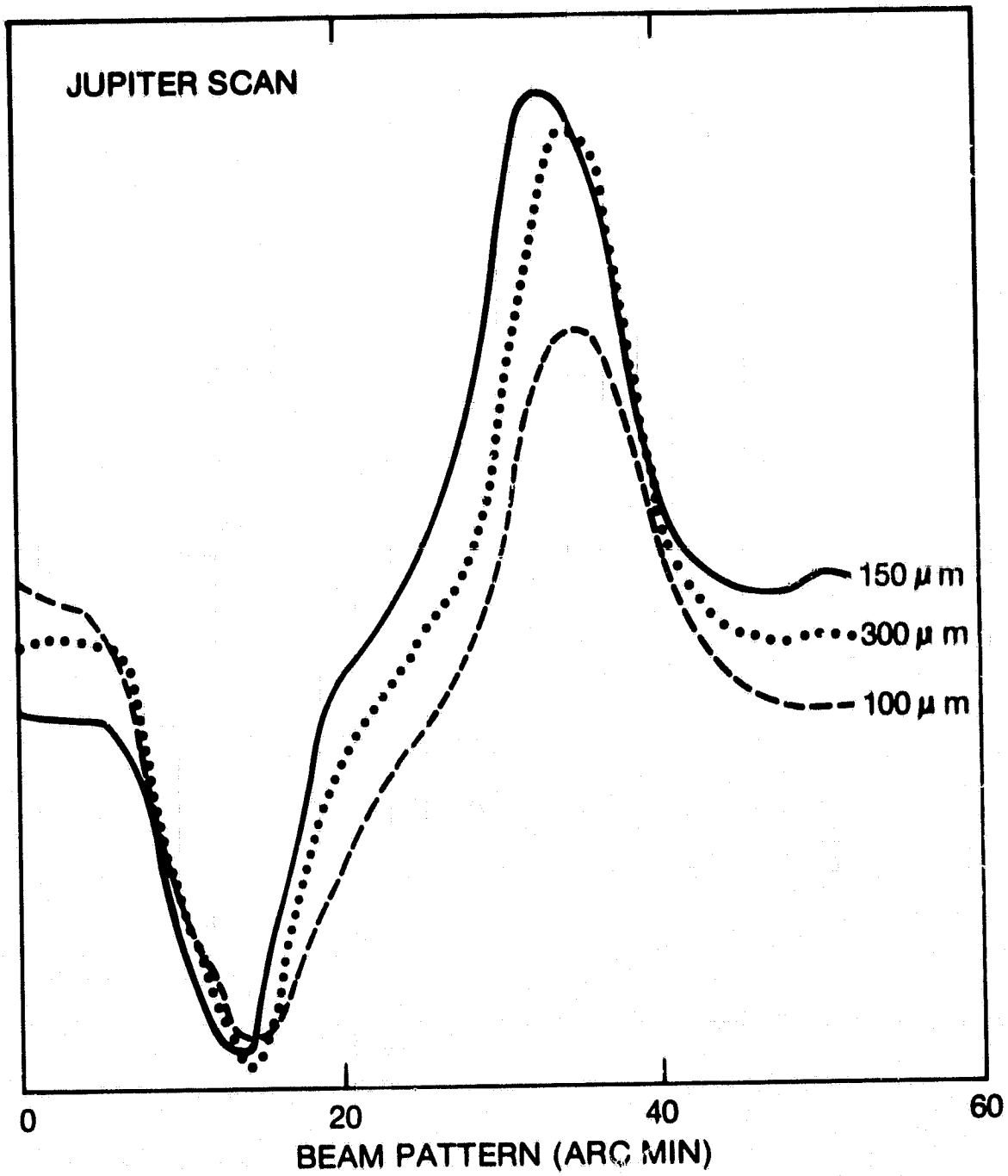
JUPITER SCAN
150 μ m
300 μ m
100 μ m
0
20
40
60
BEAM PATTERN (ARC MIN)

FIGURE 5.2

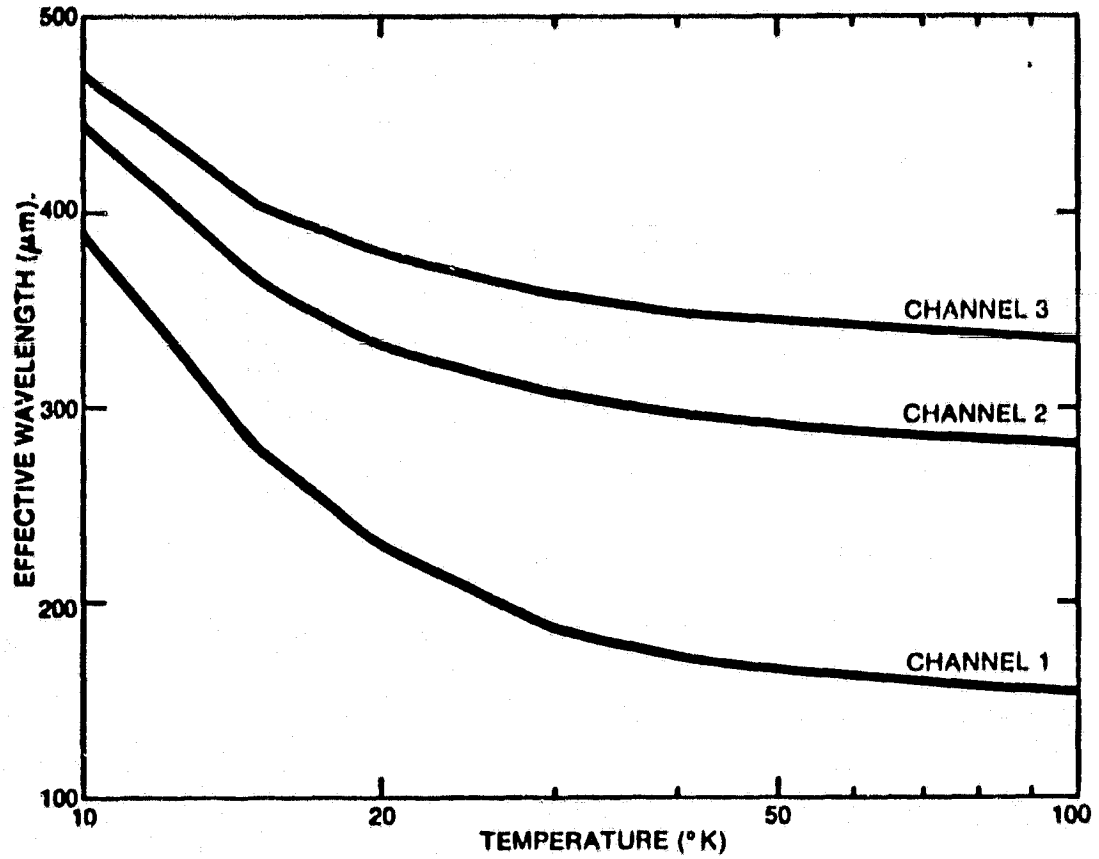
500
400
300
200
100
EFFECTIVE WAVELENGTH (μm).
CHANNEL 3
CHANNEL 2
CHANNEL 1
10
20
50
100
TEMPERATURE (°K)

FIGURE 5.3

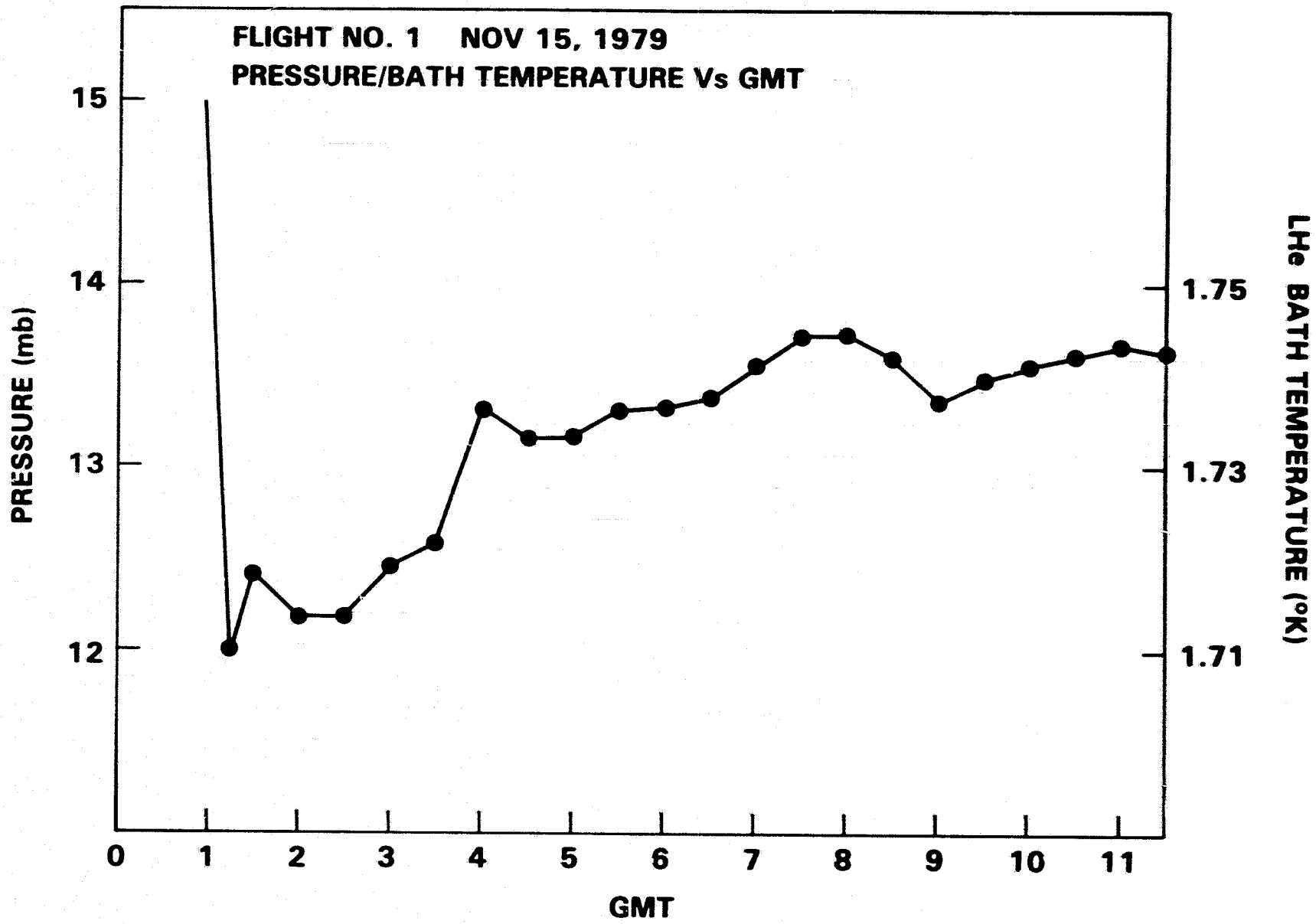
FLIGHT NO. 1 NOV 15, 1979
PRESSURE/BATH TEMPERATURE Vs GMT
PRESSURE (mb)
15
14
13
12
LHe BATH TEMPERATURE (°K)
1.75
1.73
1.71
0
1
2
3
4
5
6
7
8
9
10
11
GMT

FIGURE 5.4

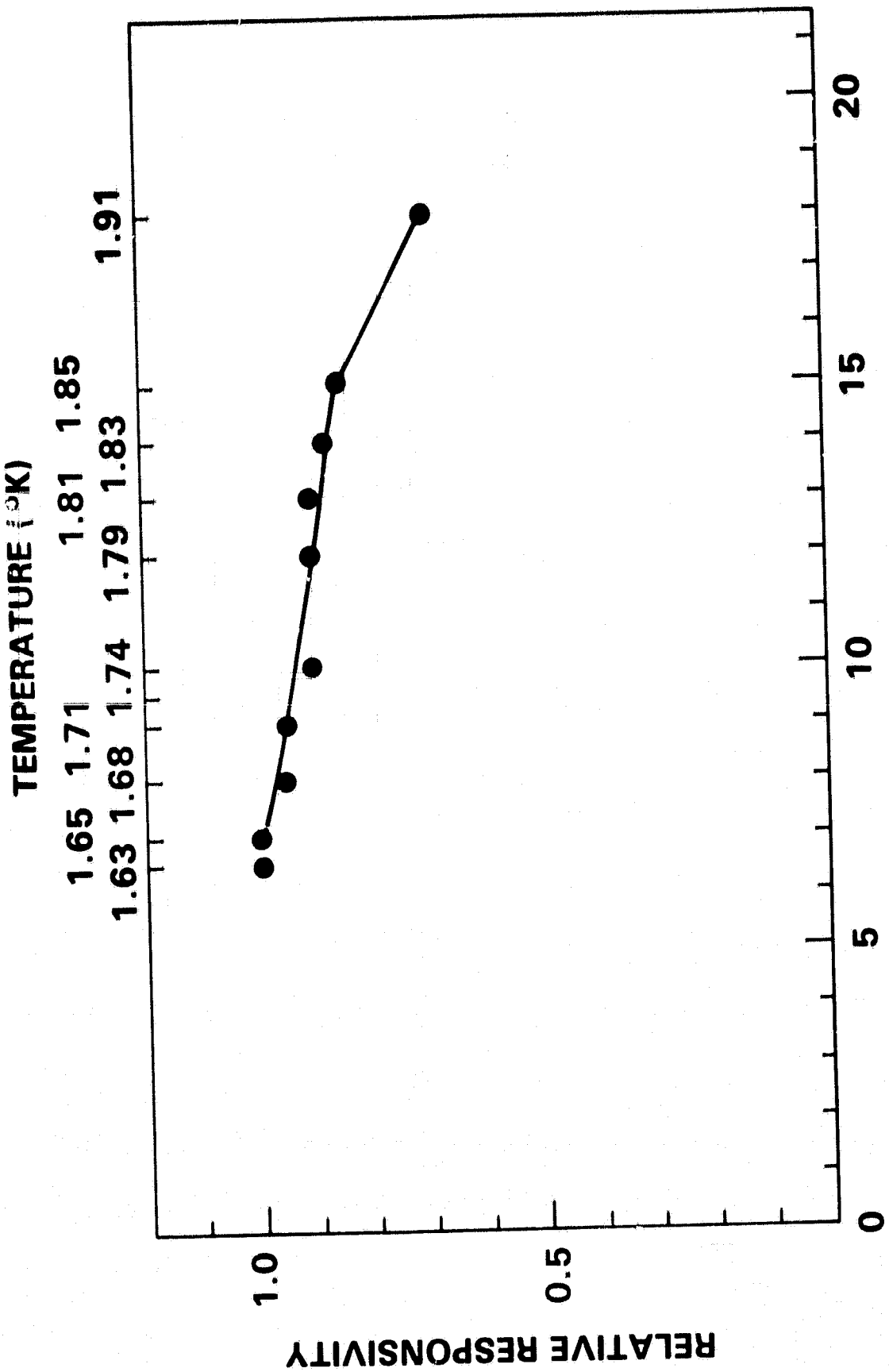
RELATIVE RESPONSIVITY
1.0
0.5
0
5
10
15
20
PRESSURE (mm Hg)
TEMPERATURE (°K)
1.63 1.65 1.68 1.71 1.74 1.79 1.81 1.83 1.85 1.91

FIGURE 5-5

CHAPTER 6

SUBMILLIMETER WAVE SURVEY OF THE GALACTIC PLANE

6.1 SUBMILLIMETER WAVE EMISSION CONTOUR MAPS

The results of the Submillimeter Sky Survey presented in this thesis are confined to the region of the Galactic plane from $\ell = 8°$ to $\ell = 44°$. Contour maps of the surface brightness in the three wavelength bands are presented in Figure 6.1. The data covers approximately 1/4 of all the sky regions observed in the first flight of the instrument on November 15, 1979. A map showing the total sky coverage in the first two flights is shown in Figure 3.3.

Details on the data reduction and analysis leading to the results presented here have been discussed in the previous chapters. To summarize, the observations were made in a raster scanning mode using an array of three detectors each having a field of view of 10 arc min square. Jupiter was used as the photometric calibration standard, with an assumed brightness temperature of 125 kelvin at submillimeter wavelengths (Wright, 1976; Armstrong et al., 1972). The statistical photometric uncertainties associated with the three wavelength bands are approximately 3×10^{-6}, 1×10^{-6}, and 7×10^{-7} w m^{-2} sr^{-1} respectively, corresponding to about 1/2 to 1/3 of the lowest contour level in the maps.

The absolute photometric uncertainties in the calibration from accountable sources are about 15 %. The sources of uncertainties are discussed in Section 5.3. Positions on the maps were calibrated by using the in-flight observed positions of a set of bright stars shown in Figure 4.4. The positional uncertainty is typically less than 5 arcmin.

The contour maps are plotted in Galactic coordinates. The slanted lines represent the boundaries of the sky fields surveyed, which cover approximately ± 3° in Galactic latitude. Scanning and beam switching are along the direction parallel to one pair of the boundaries which is at an angle less than 45 degrees to the line of constant latitude. This orientation was planned so that extended emission may be more easily restored. Some of the extended spurs and valleys in the contours along the scanning and beam-switching direction may be spurious, arising mainly from the extended source restoration process where baseline drift or a noise glitch may be present. These anomalies, however, do not appear to affect significantly the contour levels other than the lowest two. No attempts were made to smooth the contours as some of the features may be real.

The identifiable individual emission peaks and the extended, diffuse emission from the Galactic plane are analyzed and discussed separately in the following sections.

6.2 SELECTED BRIGHT, DISCRETE SOURCES

After development of the large scale map, a list of sources with relative maximum peak emission in the submillimeter maps was selected and catalogued for further studies. The selection may not be all inclusive and may overlook either very extended emission plateaus or small sources with peak fluxes only a few times noise above a smooth continuum background. These submillimeter emission peaks are designated by their Galactic coordinates, and are listed in Table 6.1, together with the equatorial coordinates and the observed surface brightness in the three channels with one beam size centered on the peak position.

The second part of Table 6.1 contains a few derived quantities based on the observed submillimeter surface brightness. These include the dust temperature, total far-infrared radiance, optical depth, and dust column density. Details on how these derived quantities were generated are given in Appendix A. In the analysis of the submillimeter survey data, it is assumed that the emission arises from thermal continuum radiation by dust grains. This assumption is based on the observed brightness level and on previous observational experience. The ratios of the fluxes in the three spectral bands are consistent with those

expected from blackbody sources at temperatures of a few tens of degree Kelvin. The surface brightness observed within the broad continuum spectral bands is much too high to be significantly affected by line emission processes.

Table 6.2 provides an identification of the sources with those that have been observed in other surveys at infrared and submillimeter wavelengths. The striking result is that among the 27 emission peaks listed in Table 6.1, 9 have not been identified in previous surveys at far infrared and submillimeter wavelengths (Nishimura et al., 1980; Boisse et al., 1980; Ryter and Puget, 1977, Low et al., 1977; Olthof, 1974; Furniss et al., 1975; Hoffmann et al., 1971). Of the remaining, 9 were found to be located within 0.2 degree (about 1 beam width in our survey) of identified sources in the survey of Nishimura et al., (1980), Furniss et al., (1975), and Hoffmann et al., (1971) where the source positions are explicitly given. The remaining 9 sources are located more than 0.2 degree but less than 0.5 degree from some previously observed far infrared sources. A summary comparison of the characteristics of these surveys is provided in Table 6.3.

The nine sources that were not identified in the previous surveys are in general as bright as those identified. A few of these are more than 1 degree away from

the Galactic equator. The signal-to-noise ratios of these sources were at least 9 in our 100 microns low-pass band. Most of these sources were also detected with high sinal-to-noise ratio in the other two longer wavelength channels at times separated by about 37 seconds, which was the time separation before the same field on the sky was scanned by these elevation angle separated detectors. As a result, these newly identified submillimeter sources may be accepted with a very high degree of confidence. The reason for their not being identified in previous surveys may be due to inadequate spatial coverage, photometric sensitivity, or brightness contrast.

The nine sources that are found to have 0.2 to 0.5 degree positional offsets were mostly identified previously by Hoffmann et al., (1971), Maihara et al., (1979) and Nishimura et al., (1980), where the observations were made at faster scanning rates with larger positional uncertainties than the present survey. The positional offsets are assumed to be caused by instrumental uncertainties.

For those sources that were previously identified, the measured surface brightness are compared with those reported in the other surveys. The purpose of this comparison is to check for consistency among the available observational

results, and to examine the spatial and spectral characteristics of the sources. The comparison, however, must be accepted with caution because of the many differences in the instruments, calibration procedures, data analysis techniques, and presentation methods. A comparison of the large scale Galactic emission is presented in a separate section.

Nishimura et al., (1980) and Low et al., (1977) have observed the Galactic plane between $\ell = 352°$ and $45°$ using different versions of the same instrument. The radiance reported by Nishimura et al., (1980) for the bright emission peaks that we have in common appear to be consistent with our measured radiance in the 100-μm low-pass band to within ± 30 % after being normalised for beam size effects. Their reported peak positions, however, typically differ from ours by more than our positional uncertainty of about 0.1 arc degree. The earlier observations of Low et al., (1977) were made with a wider spectral bandwidth of 60-300 μm which measures essentially the total infrared brightness. With this important difference, it is interesting to note that their reported radiance for the sources in common with those tabulated in Table 6.1 are approximately equal to our measured radiance in the 100-μm low-pass channel. If the calibrations are correct, this implies a source temperature lower than 30 kelvin, consistent with our derived

temperature range for the case with dust emissivity $\epsilon_\nu \propto \nu^n$, where n is the emissivity spectral index and was assumed to be 2.

The survey of Hoffmann, Frederick and Emery (1971) was made with a beam size of 12 arc minutes in the band 80-135 μm. All the sources that Hoffmann et al. have detected within the region shown in Figure 6.1 are also detected in our survey (HFE No. 49, 50, 56, 57, 58). For the first four, their quoted flux densities at an effective wavelength of 100μm are consistently about 30 % lower than our derived flux densities at an effective wavelength of about 200 μm (Channel 1). If the calibrations in both observations are correct, the observed flux density increase would imply a color temperature of about 30 K, corresponding to a dust temperature less than 30 K. This result is again consistent with our range of derived temperature for the dust emissivity index n=2. Only in one source (HFE 58) is our measured flux significantly different from that reported by Hoffmann et al., (1971).

Boisse et al., (1980) have also observed the Galactic plane with a 0.4 degree beam in the 114-195 μm and 71-95 μm bands. Their reported radiance in the 114-195 μm band are consistent to within a factor of 2 with our measured fluxes in the 100 μm band for the sources W31, W39, W43, W44, W47

and W49. The results of Ryter and Puget (1977), obtained using an instrument similar to Boisse et al. (1980), are less consistent with our results, but the difference may at least be partly accounted for by their narrower bandwidth.

The derived dust temperatures for the sources listed in Table 6.1 are in the range of 20-30 K for dust emissivity spectral index n=2 and 30-50 K for n=1. This is generally lower than the range of temperature (50-100 K) measured in the brightest one arc minute regions of HII/molecular clouds (cf. Werner et al., 1976; Harvey et al., 1978; Gatley et al., 1979; and Thronson & Harper, 1979). Probable incomplete beam-filling in our larger beam cannot affect the temperature estimate, since the temperature is derived from the flux ratio at two wavelengths. Instead, the trend supports a real temperature decrease away from the center of a source. The factor of 2 to 3 decrease resulting from a measurement using a beam 10 times wider indicates that the temperature gradient is rather modest, consistent with the theoretically estimated temperature gradient in centrally heated moecular clouds where $T(r) \propto r^{-0.4}$ (Scoville & Kwan, 1976; Leung, 1976).

6.2.1 COMPARISON WITH CO OBSERVATIONS

Another powerful technique for probing the cool interstellar material is the CO emission line observations at a wavelength of 2.6 mm. The most important source of CO excitation involves collision with molecular hydrogen (Goldreich and Kwan, 1975; Scoville and Solomon, 1974). By implication, the CO emission line is generally accepted as a tracer of the interstellar molecular hydrogen content. In this section, I present a comparison of the observational properties of the dust and molecular gas emission.

At present several surveys of the ^{12}CO molecular line emission from the Galactic plane have been made(Scoville & Solomon, 1975; Gordon & Burton, 1976; and Dame *et al.*, 1980; Cohen *et al.* 1980). For comparison with our submillimeter survey results, it is desirable that the CO observations be made with a similar beam size and adequate sampling interval so that the same fields are being observed. The CO survey of Dame *et al.*, (1980), with a beam size of 7.5 arc min and sampling interval of mostly one beam width, provides the most extensive spatial coverage at resolution similar to the present submillimeter survey. For this reason the comparisons are made mostly with the results of that survey.

The submillimeter survey measures essentially all the

dust emission along a line-of-sight. An appropriate quantity directly comparable with the submillimeter data is the CO intensity integrated over the entire velocity range. Although the ^{12}CO line is optically thick, the velocity-integrated ^{12}CO intensity is still thought to be a proportional indicator of gas column density, principally through counting clouds within the wide velocity range along a line of sight through the Galaxy (Zuckerman and Evans, 1974, Scoville and Solomon, 1975, Gordon and Burton, 1976, Leung and Lizst, 1976). A pre-publication contour map of integrated $T(^{12}CO)$ was provided to us by Dame et al., (1980), covering the latitude range from -1° to 1°. From a comparison with this map, all of the submillimeter source peaks within the Galactic latitude range ($|b| < 1°$) are seen to be associated with CO emission. About half of the submillimeter sources listed in Table 6.1 are located within 0.1° of clearly identifiable $\int T(^{12}CO)\, dV$ emission peaks. The other half, though not directly coincident with integrated CO intensity peaks, are mostly located in regions of extended emission near strong CO emission centers. The submillimeter peaks with $|b| > 1°$ are also located within the regions surveyed by Cohen et al., (1980a) where CO line emission is found, although the emission intensities at those exact locations are not individually known because of the low spatial resolution of this CO survey. The Galactic coordinate designations of the identifiable CO peaks that

are coincident with the submillimeter sources are listed in Table 6.4, together with the measured $\int T(^{12}CO)\, dV$ values for most sources.

In Figure 6.2, the submillimeter fluxes in the three channels are plotted against $\int T(^{12}CO)\, dV$. A rougly linear relationship is noted in all three channels. The scatter in the correlation appears to be smaller for Channel 2 and Channel 3. At longer submillimeter wavelengths, the dependence of the submillimeter flux on dust temperature is less sensitive. If the correlation reflects a proportionality between the dust and gas column density, the scatter should be smaller in the longer wavelength channels, as is observed in Figure 6.2. Fitting a straight line to the data points yields the following averaged observational relationship for the 22 sources:

$$\langle I(Ch.1)/\int T(CO)\, dV\rangle = 6.3 \pm 2.0 \quad (1)$$

$$\langle I(Ch.2)/\int T(CO)\, dV\rangle = 1.2 \pm 0.5 \quad (2)$$

$$\langle I(Ch.3)/\int T(CO)\, dV\rangle = 0.64 \pm 0.3 \quad (3)$$

in units of 10^{-7} w m^{-2} sr^{-1}/K km s^{-1}. The uncertainties are the r.m.s. deviation of the mean and do not reflect the systematic uncertainties.

The quantity $\int T(^{12}CO)\, dV$ provides a reasonable measure

of the hydrogen column density along a line-of-sight. A nominal conversion relationship is given by Fazio and Stecker (1976):

$$N_H = 4.6 \times 10^{20} \int T(^{12}CO)\, dV \qquad (cm^{-2}) \qquad (4)$$

where $N_H = \int n_H\, dl$, and $n_H = 2n(H_2) + n(HI)$, and $\int T(^{12}CO)\, dV$ is in units of K Km s^{-1}. As pointed out by Fazio & Stecker (1976), this conversion factor is probably uncertain by a factor of 5 when CO data are taken alone, but may be as small as 2 when arguments taking into account IR and X-ray absorption data are considered.

Using Equations (4) and (A13), the gas-to-dust ratio for the list of sources in Table 6.2 is then given by :

$$\begin{aligned} M_H / M_D &= N_H\, m_H / M_D \\ &= 7.6 \times 10^{-4} \int T(^{12}CO) dV / M_D \end{aligned} \qquad (5)$$

where $\int T(^{12}CO)\, dV$ is in units of K km s^{-1} and M_D is the dust mass column density in units of gm cm^{-2}. This ratio is independent of the assumed source distance. The gas-to-dust mass ratios for the list of sources in Table 6.4 fall within the wide range 30 to 300. The mean gas-to-dust mass ratio for the 22 sources is

$$\langle M_H / M_D \rangle = 130 \pm 70$$

It is worth pointing out that the gas-to-dust ratio derived in this way represents an average value along a line-of-sight through the Galaxy. Inherent in the derivation are two simplifying assumptions: 1) the emissivity properties of the dust grains in the interstellar medium may be characterized by a single set of mixture-averaged parameters (see Appendix A), and 2) the column density of atomic and molecular hydrogen gas along a line-of-sight is related to the integrated CO intensity by equation (4). Concerning the second assumption, the integrated CO intensity is generally thought to be a proportional measure of the molecular hydrogen content only, and is not related to the atomic hydrogen content. The justification for including the atomic hydrogen content in equation (4) is based on empirical results of several independent observations including 21-cm line, ^{12}CO line, x-ray absorption, γ-ray and infrared flux. The inferred total gas column densities (H_2 + HI) in the direction of the Galactic center from these measurements were summarized by Stecker et al. (1975). Equation (4) is an empirical conversion relationship obtained from these observations, and is assumed to be applicable to other Galactic longitude regions as well. In general, a line-of-sight along the Galactic plane passes through both spiral-arm and inter-arm regions where hydrogen gas in molecular and atomic forms may be present in varying amount, so that the proportionality

constant in equation (4) may vary accordingly. For the present purpose, it is sufficient to assume a constant proportionality factor. The fact that the above gas-to-dust mass ratio is so close to the value of 100 obtained from other observational evidence indicates that the CO-to-hydrogen abundance ratio adopted in equation (4) is quite realistic.

As most of the mass in the interstellar clouds is in the form of hydrogen, while the bulk of the luminosity is radiated at far infrared and submillimeter wavelengths, the ratio $I_{IR}/\int T(CO)\, dV$ provides a measure of the mass-to-light ratio for those clouds. The estimated total infrared brightness I_{IR}, related to the flux in one channel by Equation (A8), is plotted against the measured $\int T(CO)\, dV$ in Figure 6.3. As seen from the graph, a rough trend of proportionality is noted, although the scatter is rather large. The averaged value for the 22 sources is:

$$\langle I_{IR} / \int T(^{12}CO)\, dV \rangle \propto (1.9 \pm 0.9) \times 10^{-6} \qquad (6)$$

in units of w m^{-2} sr^{-1}/K km s^{-1}. The uncertainty is a measure of the dispersion about the mean and does not reflect any systematic uncertainty. The small dispersion is remarkable since $I_{IR} \propto T_d^{6}$ for dust grains with emissivity index n = 2. For a dust temperature range of 20-30 K, an

uncertainty of 5 K would translate into a possible uncertainty in the above ratio by at least a factor of 3.

The hydrogen mass-to-infrared luminosity ratio, M_H/L_{IR}, may also be derived from equations (4) and (6):

$$M_H / L_{IR} = 1/4\pi \; 4.6 \times 10^{20} \; m_H \int T(^{12}CO) \; dV / I_{IR}$$
$$= 1.2 \times 10^{-7} \int T(^{12}CO) \; dV / I_{IR} \quad (M_\odot/L_\odot) \quad (7)$$

where L_{IR} is the total infrared luminosity. This ratio is independent of the assumed source distance. The values for the submillimeter peaks in units of $M_\odot/L_\odot$ are tabulated in Table 6.2. The ratios are in general one to two orders of magnitude below the solar value. The mean value of the hydrogen mass-to-infrared light ratio, derived from the fitted slope of Figure 6.3, is

$$< M_H / L_{IR} > = 0.061 \pm 0.03 \quad (M_\odot/L_\odot) \quad (8)$$

This average value corresponds to an infrared luminosity per hydrogen atom $< L_{IR}^{H} > \approx 5 \times 10^{-30}$ w/(H atom) at these bright peaks, compared with the value of 2×10^{-30} w/(H atom) for the average interstellar medium reported by Serra et al., (1978).

6.2.2 COMPARISON WITH RADIO CONTINUUM OBSERVATIONS

In Table 6.5 the submillimeter emission peaks are listed together with probable identifications of radio continuum sources at 5 GHz. For sources with $|b| < 1°$, the radio peak designations are obtained from the survey maps of Altenhoff *et al.*, (1978), which used a beam width of 2.6 arcmin and obtained a positional uncertainty of 0.3 arcmin. For sources outside this latitude range, the radio source positions are obtained from the survey of Altenhoff *et al.* (1970), with a beam size of 11 arcmin and a positional uncertainty of 1 arcmin.

The most remarkable result in Table 6.5 is that 19 of the 27 submillimeter sources with $|b| < 1°$ are found to be located within 0.1° of the radio continuum peak positions selected from Altenhoff *et al.* (1978). The three sources with $|b| > 1°$ are also associated with radio continuum emission peaks given in Altenhoff *et al.* (1970). Only 4 of the 27 sources are found not to have any significant 5 GHz emission. The radio continuum spectral slopes indicates that the radio sources are predominantly HII regions.

Of the 4 submillimeter sources that do not possess any significant radio continuum emission, two (G33.4+0.1, G34.5+0.2) are associated with ^{12}CO emission peaks in the

maps of Dame et al. (1980). The other two (G18.9-0.1, G21.4-0.2) are also located in regions of fairly strong CO line intensity.

For those sources that are associated with free-free emission, the 5 GHz flux densities measured with an 11 arc minute beam (Altenhoff et al., 1970) are given in Table 6.5. Judging from the FWHP radio source sizes and source distributions in the radio maps (Altenhoff et al., 1978), the 11 arc minute beam is probably large enough to measure all of the free-free emission from the individual sources but small enough to exclude contributions from nearby sources. The total free-free emission at 5 GHz provides a means for estimating the Lyman continuum (Lyc) photons required to sustain the ionization of the HII regions. The Lyc photons absorbed by the gas are eventually degraded into Lyman alpha (Lyα) photons which can only be removed by absorption by dust grains. In many far infrared sources, the observed infrared flux is often much too large to be accounted for by Lyα absorption alone (Emerson and Jennings, 1978; Gatley, 1979, Furniss et al., 1975; Harper and Low, 1971). A measure of the relative importance of dust heat sources other than Lyα photons is provided by the infrared excess ratio (IRE), defined as:

$$IRE = L_{IR} / N_c h\nu_\alpha \qquad (9)$$

where L_{IR} is the integrated infrared luminosity, N_c is the number of Lyc photons, h is Planck's constant, ν_α is frequency of a Lyα photon. If every recombination of an electron with a H^+ ion eventually lead to the production of a Lyα photon, $N_c h\nu_\alpha$ is the luminosity that would be available for dust heating through absorption of Lyα photons. The free-free continuum flux is proportional to the number of recombinations. Thus N_c, the number of Lyc photons per second required to maintain the ionization of an HII region, may be inferred using the relation (Mezger et al., 1974):

$$(N_c/\text{sec}) = 4.76 \times 10^{48}\, a(\nu,T_e)^{-1}\, (\nu/\text{GHz})^{0.1} \times (T_e/\text{K})^{-0.45}\, (S_\nu/\text{Jy})\, (D/\text{Kpc})^2 \qquad (10)$$

where S_ν is the free-free flux at frequency ν, T_e is the electron temperature, and $a(n,T_e)$ is an numerical correction factor for the optical depth tabulated by Mezger and Henderson (1967) and is very close to 1 under normal circumstances. Using the flux density S_ν from Altenhoff et al., (1970) and the electron temperatures T_e from Reifenstein et al., (1970) and Shaver and Goss (1970), the infrared excess ratios for the list of submillimeter peaks are calculated and listed in Table 6.5. The values of IRE mostly range from 1 to 15, and is considerably higher for the few sources not associated with HII regions.

Panagia (1973) has modelled the ratio of the total stellar luminosity to Lyα luminosity for zero-age main sequence (ZAMS) O and B stars. This ratio is identical to the infrared excess IRE if all the stellar radiation is absorbed by dust grains and re-radiated at far infrared wavelengths. From the tables of Panagia (1973), the value of this ratio as a function of the stellar spectral type is plotted in Figure 6.4. For stars later than O4, the stellar to Lyα luminosity ratio is greater than 3.5, increasing rapidly to larger than 100 for stars later than B0. Using Figure 6.4 as a guide, the spectral type of the embedded energy source may be estimated (though not uniquely) from the value of IRE. These estimated spectral types, SP(IRE), for the submillimeter sources are listed in Table 6.4.

The estimates of spectral type based on the infrared excess ratio and Panagia's tables are made on the following assumptions: 1) the embedded object is a ZAMS star; 2) the HII region is ionization bounded; and 3) there is little or no dust inside the HII region to compete for the absorption of Lyc photons. If, for example, the embedded heat source is at an earlier evolutionary stage, the observed IRE may be significantly higher than that of a main sequence star with an equivalent initial mass. The presence of dust inside the HII region may also affect the ionization structure, and give rise to an apparently later spectral type estimate.

The validity of the above assumptions may be tested by evaluating the luminosities inferred from the spectral type and from the submillimeter brightness. It is noteworthy that the estimate of the spectral type is independent of the assumed distance. Using the parameters of the early type stars in Panagia (1973), the stellar luminosity for a single star of spectral type SP, L(SP), is inferred and listed in Table 6.4. The infrared luminosity L(IR) measured at that position may also be derived from the submillimeter data if the source distance is known. It is assumed that the infrared source is located approximately at the same position as the radio continuum source. The distance to the infrared source is taken to be equal to the distance derived from hydrogen recombination line observations of Reifenstein et. al. (1970), Wilson et. al. (1972), Wilson (1974), and Churchwell et. al. (1978).

It is of interest to compare L(IR) and L(SP). In Table 6.6, the sources are classified according to whether L(IR) is larger or smaller than L(SP). The case with L(IR) larger than L(SP) may imply the following scenarios: 1) the embedded energy source contains more than one star of spectral type SP(IRE) or later, with combined luminosity L(IR); or 2) a significant amount of dust is inside the HII region, absorbing part of the Lyc photons; or 3) the energy

source is a pre-main-sequence object with lower ionizing photon flux than an equivalent ZAMS star; or 4) the source is closer than assumed in estimating L_{IR}. For the case where L(IR) is smaller than L(SP), the HII region may be a well developed one with very little dust absorption and re-radiation, so that the infrared luminosity observed does not account for all of the stellar luminosity; or, the source is more distant than assumed in estimating L_{IR}.

A plot of the Infrared Excess IRE versus distance from the Galactic center is shown in Figure 6.5. The graph suggests that the IRE may be decreasing with increasing galactocentric distance. A decrease in IRE with increasing galactocentric distance was noted by Boisse et al. (1980), who intrepreted this as due to a combination of galactic gradients in dust-to-gas mass ratio and the initial mass function. Our data are less conclusive on the existence of a gradient in IRE. Because of the scatter in Figure 6.5 and of the small number of samples involved, an intrepretation is not presented here. This relationship will be investigated in more detail when the present survey data for the complete Galactic plane is analyzed.

6.3 DIFFUSE SUBMILLIMETER EMISSION

Underlying the relatively compact emission peaks discussed in the previous sections is a diffuse submillimeter emissive background. The diffuse galactic plane emission at far infrared and submillimeter wavelengths has been previously detected in several previous surveys (e.g. Pipher, 1973, Rouan et al., 1977, Maihara et al., 1978, Owen et al., 1979, Nishimura et al., 1980) using large-beam instruments on balloon and rocket platforms. The present survey provides an order-of-magnitude improvement in sensitivity and represents the first observation to provide multispectral measurements at submillimeter wavelengths.

As shown in the submillimeter surface brightness contour maps in Figure 6.1, the diffuse emission extends continuously over the entire range of Galactic longitude, and up to approximately ± 1.5° in latitude. The large scale structures in the emission are mostly extended in the longitude direction with angular scale size of a few degrees. The width of the emission in the $\lambda > 100$ μm band (Channel 1) extends over ± 1 degree at longitudes $\ell < 20°$, and decreases slowly to slightly under ± 1 degree at longitude $\ell \approx 40°$. The observed full latitude extent is in approximate agreement with that measured by Nishimura et al., (1980), who employed a linear fast scanning instrument

instead of our double beam differential approach. The full latitude extent is dependent on the minimum detectable surface brightness gradient, which was about 3 x 10^{-6} w m^{-2} sr^{-1} deg^{-1} in our 100 μm low-pass channel and is about a factor of 2 lower than that of Nishimura et al., (1980). The minimum detectable surface brightness gradient was about 2 and 1 x 10^{-6} w m^{-2} sr^{-1} deg^{-1} in the two other longer wavelength channels . The apparent decrease in the full latitude extent at the longer wavelength bands probably reflects the falling spectrum for sources with color temperature > 10 K.

In order to examine the larger-scale aspects of the submillimeter emission from the different regions of the Galactic plane, the surface brightness in each of the three channels was integrated over the entire latitude range to yield the longitudinal brightness profiles (Figure 6.6). Strong emission peaks of relatively small angular extent do not contribute much to the integrated profiles. The lowest two contours of the maps in Figure 6.1 typically account for more than 50 % of the integrated brightness. The three brightness profiles shown in Figure 6.6 therefore provide a better overall picture of the variation of the emission structure along the Galactic plane. The uncertainties in the longitude profiles are mainly determined by the uncertainties in the position of the lowest contour, and are

estimated to be about 20, 7, and 5 x 10^{-10} w m^{-2} deg^{-1} in the three channels respectively.

One of the characteristics of the longitude profiles is the clumped nature of the submillimeter emission. The profiles exhibit strong brightness contrast with an angular scale of rougly 2 to 6 degrees. The overall emission profiles in the three submillimeter wavelength channels do not appear to differ significantly from one another. Observationally, the submillimeter surface brightness is proportional to the dust column density and temperature as $I \propto M_d \times f(T)$, where f(T) is a function of dust temperature related to the convolution of the photometer spectral pass band and Planck's function. The strong emission contrast may be attributed to dust column density or temperature effects. A brightness contrast of about 5-10 would translate into either a density contrast of 5-10 or a temperature contrast of about 2, or a combination of both.

The temperature effect may be investigated from the observed flux ratio between Channel 1 and Channel 2. Figure 6.7 shows the profile of the integrated brightness ratio. The inferred dust temperature for an effective dust emissivity spectral index of n = 2 is labelled on the right vertical axis. I adopted the value n = 2 based on consideration of theoretical calculations on dust grain

models (Leung, 1976). Observational results of other dust clouds suggest that $2 \leq n \leq 1$, so that the inferred dust temperature from using $n = 2$ probably represents a lower limit. The relative temperature profile is independent of specific dust parameters as long as the emissive properties are constant over the longitude range. As shown in Figure 6.7, the temperature profile does not show structure with sufficient contrast at the appropiate longitude to account for the variations in the submillimeter brightness profile. On this basis, the submillimeter brightness variations are thought to be largely caused by variations in the dust column density along a line of sight. Further support of this is provided in the comparison of the submillimeter brightness and the CO line intensity discussed in the next section.

A more interesting feature in the temperature profile in Figure 6.7 is that the mean temperature appears to increase slowly from $\ell = 8°$ to $\ell = 30°$, and then decreases abruptly at about $\ell = 32°$. Beyond this longitude range, the temperature trend is less well defined. It is important to note that in taking the flux ratio, many systematic effects in the calibrations are cancelled out, so that the flux ratio uncertainties are mainly dominated by statistical effects. The estimated uncertainty in the flux ratio is about $\pm$ 1, or about 20%, and perhaps slightly larger at

longitudes greater than 40 degrees. A linear least square fit to the flux ratio profile between ℓ = 8° to 32° was attempted and the fit is shown in the same figure. The reduced chi-square is about 0.92, indicating that the fitted gradient is probably a good representation of the general trend in the flux ratio profile within that longitude range.

The average dust temperature over the longitude and latitude range in Figure 6.1 may be inferred from the following two ratios:

$$\langle \int I(\mathrm{Ch.1})\, db / \int I(\mathrm{Ch.2})\, db \rangle = 4.6 \pm 1.2 \qquad (11)$$

$$\langle \int I(\mathrm{Ch.1})\, db / \int I(\mathrm{Ch.3})\, db \rangle = 7.7 \pm 2.2 \qquad (12)$$

Both of these ratios translate into an average dust temperature T_{IR} = 21 ± 4 K according to Figure A3 in Appendix A, assuming a dust emissivity spectral index n=2.

This dust temperature gradient, and the abrupt decrease, if real, may have important implications for the nature and distribution of the energy sources powering the Galactic submillimeter emission. Since the luminosity of the energy source required to raise the dust grains to temperature T scales as T^6 (assuming n=2), even a moderate increase in temperature from 17 to 25 K would imply a factor of 10 increase in luminosity density, other parameters being

constant. In this context, the temperature profile suggests a gradual, order-of-magnitude increase in infrared luminosity density towards the region $\ell = 30°$, followed by a steep decrease at a small angle beyond. This will be discussed in more detail in Section 6.4.

6.3.1 COMPARISON WITH CO SURVEY OF THE GALACTIC PLANE

A comparison of the diffuse submillimeter emission profile with the results of the ^{12}CO survey of Dame *et al.* (1980) is of particular interest. Both of these two surveys provide presently the most complete area coverage and highest spatial resolution of any Galactic plane survey at these wavelengths. The results provide an excellent data base for a meaningful comparison of the properties of dust and gas emission on a Galactic scale.

The most striking feature in the comparison of the longitudinal profiles of the submillimeter and ^{12}CO emission, plotted together in Figure 6.8, is the extremely good correlation between the submillimeter and CO emission profiles. The CO profile is obtained by integrating over all velocities and over the latitude range between -1 to +1 degree, while the submillimeter profile is also obtained by integrating over the same latitude range. These two profiles are almost identical to each other over the entire range of brightness contrast. A measure of the close agreement is provided in Figure 6.9 where the ratio of the submillimeter(λ >100 μm) to $\int T(^{12}CO)\, dV$ surface brightness is plotted on a linear scale in units of 10^{-7} w m^{-2} sr^{-1}/K km s^{-1}. An accompanying histogram shows that the brightness ratios fall within a very narrow range

of values with a gaussian shape distribution. The average submillimeter to CO surface brightness ratio is:

$$\langle I(Ch.1)/\int T(CO)\, dV \rangle = 4.8 \pm 1.4 \quad (13)$$

$$\langle I(Ch.2)/\int T(CO)\, dV \rangle = 1.1 \pm 0.34 \quad (14)$$

in units of 10^{-7} w m^{-2} sr^{-1}/K km s^{-1}. The uncertainties are r.m.s. measures of the scatter of the ratios and are much smaller than the contrast in the individual submillimeter or CO profiles. These ratios are observational results independent of any specific model of the emission processes. As a comparison, the corresponding average ratios for the 22 identifiable emission peaks discussed in Section 6.2.1 are 6.28 ± 2.21, 1.2 ± 0.5 for Channnel 1 and 2 respectively.

From an observational standpoint, this result provides an excellent prescription for inferring the gas emission intensity based solely on observations of dust emission alone (or vice versa). The essentially equivalent profiles of the ^{12}CO and submillimeter intensity over such a wide longitude range is unlikely to be fortuitous. Instead, the observational data provide strong support for a relationship of a more fundamental nature. The close correlation between the dust and molecular gas emission may be understandable within the framework of theoretical studies on the problems of 1) the formation of molecular hydrogen and 2) the energy

transfer between dust and gas.

It has been generally accepted that dust is an important ingredient for molecular hydrogen formation in the interstellar medium (Hollenbach and Salpeter, 1971; Hollenbach, Werner, and Salpeter, 1971; Cohen, 1976, Barlow and Silk, 1976; Goodman, 1978; Federman et al., 1979). The dust particles affect both the formation rate and the density of molecular hydrogen in two aspects. First, the dust grains provide the surfaces for the conversion of hydrogen from atomic to molecular form and for taking up the heat of formation. Second, the high ultraviolet and visible opacity of dust clouds provides effective shielding for the molecules from photo-dissociation by the interstellar radiation field. Above an extinction of about 1 magnitude, there is a sharp increase in the conversion of H into H_2. Consequently, molecular gas is more likely to be associated with regions of high dust density and is observable through CO line emission. Furthermore, theoretical modelling of CO cooling rates in molecular clouds with hydrogen density above 10^3 cm^{-3} suggests that collisons of gas and dust grains is a major energy transfer process for the gas to maintain the observed emission rate (Goldreich and Kwan 1974). As a result, the CO emission intensity is dependent on the dust and gas density as well as on the dust temperature. These interactions of molecular gas and dust

could be the factors leading to the observational similarity of the CO and submillimeter emission profiles. The present survey provides a quantitative measure of the relative emission strength which appears to remain constant along the Galactic plane.

The similarity of the CO and submillimeter profiles supports the idea that both surveys are observing gas and dust in spatially identical regions. On the basis of this assumption, several aspects of the interstellar gas and dust relationship are examined.

A) Interstellar Gas and Dust Ratio and Extinction.

As discussed in Appendix A, the dust column density M_d along a line of sight is related to the submillimeter emission by:

$$M_d = 1.2 \times 10^{23} \, I \, / \int \nu^2 \, B_\nu(T_d) \, g_\nu \, d\nu \quad (\text{gm cm}^{-2}) \qquad (15)$$

where I is the measured submillimeter radiance in units of w m^{-2} sr^{-1}, $B_\nu(T_d)$ is Planck's function at frequency ν and temperature T_d in units of w m^{-2} sr^{-1} Hz^{-1}, g_ν is the normalized spectral response of the photometer. The gas-to-dust ratio may be inferred from the submillimeter and

CO observations as follows (Equation 5):

$$M_H/M_d = 7.6 \times 10^{-4} \int T(CO)\, dV/M_d$$
$$= 6.3 \times 10^{-27} \iint T(CO)\, dV\, db / \int I(Ch.2)\, db$$
$$\times \int \nu^2 B_\nu(T_d)\, g_\nu\, d\nu \qquad (16)$$

where $\int T(CO)\, dV$ is in K km s^{-1} and I(Ch.2) in w m^{-2} sr^{-1}, B_ν in w m^{-2} sr^{-1} Hz^{-1}. The flux in Channel 2 is used because it is less sensitive to temperature. Putting the derived temperature profile into Equation (16), the gas to dust mass ratio profile was calculated and is shown in Figure 6.10. The mean gas-to-dust mass ratio, averaged over the entire longitude and latitude range, is

$$\langle M_H/M_d \rangle = 100 \pm 70. \qquad (17)$$

Again, the uncertainty is only a measure of the scatter and does not take into account the much higher uncertainties in the modelled dust emissive properties and the CO to H abundance ratio. The large scatter in the gas-to-dust ratio may be due to variations in dust temperature. A systematic trend, if any, cannot be established with confidence.

The average interstellar extinction of visible light, A_v, is proportional to the amount of dust along a given line of sight. An empirical relationship between the value of

extinction A_v to dust column density, assuming that the composition of dust is uniform, is given by Aannestad and Purcell (1973):

$$A_v = KM_d \quad \text{(mag)} \tag{18}$$

where $K = 3 \times 10^4$ cm^2 gm^{-1}, and M_d in gm m^{-2}. The interstellar extinction-to-gas ratio is then related to the submillimeter to CO intensity by (Equations 4,15)

$$\langle A_v/N_H \rangle = \langle KM_d/N_H \rangle$$

$$= 7.8 \times 10^6 \langle I(Ch.2)/\int T(CO)\, dV \rangle \times 1/\int \nu^2 B_\nu(T_d)\, g_\nu\, d\nu. \tag{19}$$

Assuming $T_d = 21 \pm 4$ K, $\langle I(Ch.2)/\int T(CO)\, dV \rangle = (1.1 \pm 0.34) \times 10^{-7}$ w m^{-2} sr^{-1}/K km s^{-1}, the average extinction to gas ratio is:

$$\langle A_v/N_H \rangle = (8 \pm 5) \times 10^{-22} \text{ mag/atom cm}^{-2} \tag{20}$$

where $N_H = N(HI)+2N(H_2)$.

Dickman (1976) has investigated this relationship using star counts and ^{13}CO column density observations in the direction of dark clouds. His derived extinction to H_2

ratio is:

$$\langle A_V/N(H_2)\rangle = (8 \pm 6) \times 10^{-22} \text{ mag/mol. cm}^{-2} \qquad (21)$$

Savage et al. (1977) and Bohlin, Savage, and Drake (1978) have utilized the Copernicus satellite to study the atomic and molecular hydrogen UV absorption in the direction of about 100 hot stars. They have derived a similar relationship:

$$\langle A_V/N_H\rangle = 5 \times 10^{-22} \text{ mag/atom cm}^{-2} \qquad (22)$$

The above comparison indicates that the interstellar extinction-to-gas ratio derived from submillimeter observations over long path lengths is very comparable to the localized ratio provided by the star count or reddening method. Thus the submillimeter observations may be used for further extending extinction estimates to regions of high opacity where star count methods are difficult, such as in very dense clouds or in external galaxies.

B) Gas and Dust Temperature and Size of Molecular Clouds

The CO survey of Dame et al., (1980) was made with a large beam size of 7.5 arcmin. As a result, the gas

temperature cannot be reliably estimated because of the uncertainty in the beam filling factor. The submillimeter survey, on the other hand, provides a temperature estimate of the dust which is independent of the beam filling factor. Collisions between dust and gas are expected to maintain the gas temperature close to that of the dust (Goldreich and Kwan, 1974). The gas temperature may be inferred from the submillimeter data with less uncertainty than from the CO survey. This suggests a way for estimating the beam filling factor in the CO survey observations which in turn is related to the average cross section of the molecular clouds within the observed velocity range along a line of sight through the Galaxy.

The equivalent radiation temperature T_R of the CO line is related to the observed flux density I_ν and the excitation temperature T_x of the CO gas by:

$$I_\nu = 2kT_R\nu^2/c^2 = \eta_\nu [B_\nu(T_x)-B_\nu(2.7)] (1-e^{-\tau\nu}) \qquad (23)$$

where η_ν is the beam filling factor at frequency ν (or velocity V), and τ_ν is the optical depth along a line of sight. For an optically thick ^{12}CO J=1-0 line, the radiation temperature is:

$$T_R = \eta_\nu h\nu/k [f(T_x)-f(2.7)]$$

$$= \eta_\nu \; 5.52 \; [f(T_x)-f(2.7)] \quad \text{(kelvin)} \tag{24}$$

where $f(T) = (e^{5.52/T}-1)^{-1}$. The excitation temperature T_x cannot be derived from large beam CO surveys because η_ν is not known. Even in the 1 arcmin ^{12}CO surveys of Scoville and Solomon (1975) and Gordon and Burton (1976), η_ν is unknown a priori. Under the assumption of local thermodynamic equilibrium, the excitation temperature is equal to the kinetic temperature of the gas, which is related to the dust temperature empirically by:

$$T_x = \alpha \; T_d \tag{25}$$

where α is a numerical constant slightly less than 1 (Goldriech and Kwan, 1974). For the following analysis I adopted a nominal value of 1. The dust temperature T_d derived from the submillimeter data is an averaged value along a line of sight, so that it is appropriate to consider the averaged CO radiation temperature and beam filling factor:

$$\langle T_R \rangle = \int T(^{12}CO) \; dV \; / \int dV \tag{26}$$

and $$\langle \eta_\nu \rangle = \int\int d\Omega \; dV \; / \; \Omega \int dV$$

$$= \langle T_R \rangle \; / \; 5.52[f(\alpha T_d)-f(2.7)]. \tag{27}$$

Using the value of $\int T(CO)\, dV$ and $\int dV$ from the survey data of Dame et al., (1980), and assuming $\alpha = 1$ and $T_x = T_d = 21 \pm 4$ K, the value of the beam filling factor averaged over the latitude range of $\pm$ 1 degree has been evaluated for the Galactic longitude range $\ell = 8°$ to $44°$. The longitude profile is shown in Figure 6.11. The range of beam filling factor for the 7.5 arcmin ^{12}CO survey is between 0.03 and 0.07.

This beam filling factor is related to the cross sections of the molecular clouds along a line of sight by:

$$\langle \eta_\nu \rangle = \langle \pi d^2 / 4 D^2 \Omega_b \rangle \qquad (28)$$

where d is the cross sectional diameter of the cloud, D is the cloud distance, and Ω_b is the solid angle of the beam. The averaged cross sectional diameter of the clouds is:

$$\begin{aligned} \langle d \rangle &= \langle 4 D^2 \Omega_b \eta_\nu / \pi \rangle^{1/2} \\ &\approx 4\text{-}6 \times 10^{-4}\ D \\ &\approx 4\text{-}6 \text{ pc} \end{aligned} \qquad (29)$$

for a 7.5 arcmin beam and a nominal source distance D of 10 kpc. Note that in the above estimate, if the thermal coupling between the dust and gas is weaker, the averaged beam filling factor and cloud cross section have to be

revised upward by about a factor of $1/\alpha$.

As a comparison, a similar analysis was made using the quoted brightness temperature of 6.6 K in the 1.2 arc min. beam ^{12}CO survey of Scoville and Solomon (1975). The average beam filling factor is $\langle \eta_v \rangle = 0.4$, corresponding to $\langle d \rangle = 2.5 \times 10^{-4}$ D.

The small beam filling factor inferred from the submillimeter and CO survey data indicates that the dust and gas is unlikely to be distributed uniformly across a 10 arc minute beam. It can also be argued that along a line of sight the distribution cannot be uniform. The minimum volume density of molecular hydrogen required to collisonally excite the J=1 to 0 line of ^{12}CO above the microwave background is estimated to be between 50 cm^{-3} (Leung and Lizst, 1976) and 300 cm^{-3} (Tucker, Kutner and Thaddeus, 1973). If the gas were uniformly distributed along a typical line-of-sight path length of 10 kpc (Cohen et al., 1980b), the derived volume density would be 1 cm^{-3}, which is less than the minimum density required to produce observable CO emission (based on a typical H_2 column density of about 4×10^{22} cm^{-2} from the ^{13}CO observation of Solomon, Scoville, and Sanders, 1979 or Equation 4 and the ^{12}CO data of Dame et al., 1980). This provides support for the idea that the gas and dust are clustered in clumps with

unit scale size of a few parsecs. On the assumption of spherical symmetry, with nominal cloud diameter of 5 pc (Equation 29), and a gas density of 300 cm^{-3}, a line of sight through the Galactic plane with a 7.5 arc minute beam would typically see approximately 10 clouds.

The above analysis provides a direct quantitative estimate of the average size of molecular clouds on a Galactic scale using complete sampling observations. An earlier estimate of cloud sizes by Burton and Gordon (1978) was based on a stochastic modeling approach using undersampled data. Their estimate of an average cloud diameter of 5-17 pc is consistent with the result of the present analysis.

C) Interstellar Mass-to-Light Ratio

With an average dust temperature of 21 ± 4 K, the total infrared intensity integrated over frequencies is twice the intensity in Channel 1 (Figure A3). The total infrared to CO intensity, averaged over the Galactic longitude and latitude range of this survey, is:

$$\langle I_{IR}/\int T(CO)\, dV\rangle = (2 \pm 1) \times \langle I(Ch.1)/\int T(CO)\, dV\rangle \quad (30)$$
$$= (10 \pm 5) \times 10^{-7} \text{ w m}^{-2} \text{ sr}^{-1}/\text{K km s}^{-1}$$

This observational result provides a means for estimating the average hydrogen mass to infrared luminosity along a line of sight (Equation 7):

$$\langle M_H/L_{IR}\rangle = 1.2 \times 10^{-7} \langle \int T(CO)\, dV/I_{IR}\rangle \; M_\odot/L_\odot$$
$$= 0.12 \pm 0.06 \; M_\odot/L_\odot \qquad (31)$$

and the infrared luminosity normalised to one hydrogen atom:

$$\langle L_{IR}{}^{H}\rangle = (2.5 \pm 1.3) \times 10^{-30} \text{ w/atom} \qquad (32)$$

Both of these two ratios are constant to within a factor of two in the longitude range $\ell = 8°$ to $44°$. In intrepreting these emissive properties, it is useful to note that the absolute value of these ratios is influenced by the assumed CO to H abundance. The relative profile or the scatter in the ratios, however, is independent of the many conversion uncertainties as long as the abundance ratios are constant.

6.3.2 COMPARISON WITH OTHER SURVEYS OF THE GALACTIC PLANE

In the last section, the longitude profile of the submillimeter emission was shown to be essentially equivalent to the resolution profile of molecular CO emission. This section presents a comparison of the submillimeter profile with several emission profile from surveys of other Galactic constituents including CO (Gordon and Burton, 1978), H166α (Lockman, 1976), HI (Westerhout 1976), extended low density (ELD) HII regions (Westerhout, 1958, Mathewson et al., 1962) and gamma rays (Kniffen et al. 1973) along the Galactic equator. These profiles are displayed together in Figure 6.12. It is well known that the Galactic radial distribution in the gaseous constituents are approximately similar to one another except for atomic hydrogen (e.g. see review by Burton, 1976). The present submillimeter survey further establishes the similarity of the distribution of the diffuse dust component with that of the molecular and ionized gaseous constituents in the interstellar medium.

The submillimeter survey has resolved the longitude profile into several bright emission structures with peak surface brightness at longitudes $\ell \approx 10°$, 12°, 18°, 24°, 30°, 35°, 37°, and 43°. These bright peak structures are most clearly discernible in the CO survey of Dame et al.,

(1980), and to a lesser extent in the surveys of Gordon and Burton (1976) and Scoville and Solomon (1975). The lesser degree of agreement with the two earlier CO surveys is not surprising because of the undersampling in these surveys. The H166α observation, likewise, is undersampled, but the peaks in the recombination line emission still appear to coincide with the bright submillimeter bands along the Galactic plane. The surveys of ELD HII regions and gamma rays (interaction of cosmic rays and interstellar nuclei), because of the much lower resolution, are in agreement with the submillimeter profile only in the very general sense that the emission profiles appear to attain a maximum near $\ell = 30°$ and then fall off rapidly at larger longitudes. The distribution of the 21-cm atomic hydrogen, however, bears very little noticeable correlation with that of the submillimeter emission.

Cohen et al. (1980b) recently provided evidence that molecular clouds are mainly confined near the spiral arms delineated by neutral hydrogen. Specifically, they identified CO spiral structures with three HI spiral arms in the first quadrant --- the 3 kpc, Scutum, and Sagittarius arms (Burton and Shane 1970; Shane, 1972; Lindblad et al., 1973). The present submillimeter survey does not provide the distance information necessary for identifying the spiral structures. However, it is interesting to note that

the longitude profile of the submillimeter emission shows prominent peak structures a few degrees wide in the line-of-sight directions at $\ell \approx 24°$, 30°, 35°, where spiral arms are identified (cf. Figure 2 and 3 of Cohen et al., 1980b and Figure 6.8 of this thesis).

The low spatial resolution for the ionized gas emission surveys (recombination line and continuum) precludes a more detailed correlation with the detailed structures of the submillimeter emission profile. Useful information on interstellar energetics may still be obtained from a comparison of the emission intensity. The integrated free-free continuum flux density from the ELD HII region shown in Figure 6.13 represents almost all the radio continuum flux at 1.4 GHz in the longitude range 8 and 44 degrees (Mezger 1978). This profile therefore provides a means of estimating the total luminosity of Lyc photons required to sustain the continuum emission in the Galaxy. As discussed in Section 6.2.4, the Infrared Excess Ratio is a quantity that relates the observed infrared luminosity to the Lyα luminosity available for heating the dust if each Lyc photon that ionizes the gas eventually degrades into a Lyα photon. The IRE ratio distribution along the galactic plane is given by:

$$IRE = 1.3 \times 10^{11} \int I(Ch.1)\, db/[S(1.4GHz)/\Delta l] \qquad (33)$$

where $\int$ I(Ch.1) db is in units of w m^{-2} deg^{-1} and S/Δl is in units of Jy deg^{-1} of longitude. Here I have assumed T_d = 21 K, so that I_{IR} = 2 x I(Ch.1), and an average electron temperature of 7000 K. A longitude profile of IRE is shown in Figure 6.13. The detailed structure in the IRE may be somewhat misleading, as the resolution of the free-free continuum profile is much lower than the submillimeter profile. The mean IRE, averaged over the longitude range, is about 10. This will be discussed further in the next section.

6.4 DISCUSSION

The observational results presented in the previous sections are summarized, and brought together to delineate a few crucial aspects of the submillimeter emission sources in the Galaxy. The results are separated into two groups according to whether the observations are sensitive to model parameters. The implications of these results on our understanding of the interstellar medium and galactic constituents are discussed.

A) Summary of Observational Results.

The observational results that are relatively insensitive to specific model parameters are the following:

1) Nine strong submillimeter emission peaks were identified for the first time.

2) Almost of the bright submillimeter emission peaks are spatially coincident with HII regions, and to a lesser degree with CO emission peaks.

3) The large-scale distribution of the submillimeter emission is observationally equivalent to that of velocity

integrated ^{12}CO emission. The longitude brightness profile shows structures as a result of column density variations. Bright submillimeter peaks are observed towards several directions, two of which may pass through the 3 Kpc and Scutum spiral arms.

4) The average submillimeter to CO surface brightness ratio between Galactic longitudes $\ell = 8°$ to $\ell = 44°$ is:

$$\langle I(Ch.1)/\int T(CO)\, dV \rangle = 4.8 \pm 1.4$$
$$\langle I(Ch.2)/\int T(CO)\, dV \rangle = 1.1 \pm 0.3$$
$$\langle I(Ch.3)/\int T(CO)\, dV \rangle = 0.6 \pm 0.3$$

in units of 10^{-7} w m^{-2} sr^{-1}/K km s^{-1}.

5) A small positive gradient in temperature with increasing longitude may be present from $\ell = 8°$ to $\ell = 32°$.

6) The beam filling factor for a 7.5 arcmin beam observation is estimated to be within the range of 0.03 to 0.07, assuming a close thermal coupling of dust and gas. The average cross section of dust and gas clouds on a Galactic scale is estimated to be about 5 pc.

The model-sensitive observational results are:

7) The average temperature of the diffuse dust clouds increases from about 17 K at ℓ = 8° to about 25 K at P = 32°. The average temperature over the entire Galactic longitude range is about 21 ± 4 K. A dust emissivity spectral index of n=2 is assumed.

8) The average dust-to-gas mass ratio in the first Galactic quadrant is estimated to be 100 ± 70, based on an assumed gas-to-CO ratio $N_H = 4.6 \times 10^{20} \int T(C))dV$ cm^{-2}, where the integrated CO intensity is in units of K km s^{-1}.

9) The ratio of interstellar extinction to gas column density derived from the submillimeter and ^{12}CO survey data is about 8×10^{-22} mag/atom cm^{-2} over a wide range of Galactic longitude, in close agreement with localized estimates based on star count and interstellar reddening methods.

10) The inferred mean ratio of hydrogen mass to infrared luminosity is about 0.06 $M_\odot/L_\odot$ for discrete emission peaks and 0.12 $M_\odot/L_\odot$ for the general interstellar medium, corresponding to a normalised infrared luminosity per hydrogen atom of L_{IR}^{H} of 5×10^{-30} w/atom and 2.5×10^{-30} w/atom. The r.m.s. scatter from this mean value is about

50% inside the regions observed.

11) The infrared excess ratios for the individual submillimeter peaks associated with HII regions are between 1 and 16. The general interstellar value is about 10. For those discrete source peaks, a negative gradient with galactocentric distance may be observed. There is no clearly identifiable gradient with longitude for the general interstellar IRE.

B) Dust Temperature and Luminosity Density.

The observed dust temperature is a key parameter that reflects the nature of the luminosity sources. It is of interest to compare the derived dust temperature with that expected if interstellar visible and ultraviolet radiation were the only heat source. Denoting the temperature the dust would reach in thermal equilibrium with interstellar visual and ultraviolet radiation field by T_{vis}, then radiative equilibrium requires:

$$4\pi a^2 \int \varepsilon_\nu \pi B_\nu(T_{vis})\, d\nu = \langle \pi a^2 \varepsilon_{vis} \rangle\, cU \qquad (34)$$

where a is the avarage dust grain radius, ε_ν is the dust grain emissivity at frequency ν, ε_{vis} is the average dust

grain emissivity at visual wavelengths, c is the speed of light, and U is the interstellar radiation field at visual and ultraviolet wavelengths. Using the nominal dust parameters in Equation (9), (10) and (11), and an interstellar radiation field $U = 7 \times 10^{-13}$ erg cm^{-3}, and $\epsilon_{vis} = 0.5$ (Allen, 1973), the solution of Equation (34) yields a dust temperature

$$T_{vis} = (6.7 \times 10^{-15} \epsilon_{vis} cU/4\pi K)^{1/6} \qquad (35)$$

$$= 19 \text{ K.}$$

Fazio and Stecker (1976), using different dust parameters, derived a value of T_{vis} of 15 K. Leung (1975) has estimated a temperature of 15-17 degree for silicate and ice-mantle grains. For a typical cloud of diameter 5-10 pc and gas density of 10^3 cm^{-3}, and an interstellar extinction-to-gas ratio $\langle A_V/N_H \rangle = 8 \times 10^{-22}$ mag/atom cm^{-2} (Sec. 6.3.1), the interstellar radiation may penetrate up to about 1 pc (A_V=1), sufficiently deep to illuminate more than half of the cloud material. The interior cloud temperature is slightly lower, so the value T_{vis} in equation (12) is a conservative upper limit to the averaged temperature along a line of sight through the cloud. The above analysis indicates that the interstellar radiation field can probably contribute a significant fraction of the energy for dust

heating, particularly near the region $\ell \approx 10°$. However, since the radiation field scales with the 6th power of the dust temperature, a luminosity density higher than the average interstellar radiation field is necessary to account for the observed averaged dust temperature of about 21 K, especially near the region around $\ell = 30°$ where the temperature appears to be closer to 25 K. Although the qualitative value of the additional luminosity density depends on specific model parameters, the basic trend in the luminosity density gradient is model independent.

In the above analysis, I have adopted a dust model with dust emissivity spectral index $n = 2$. The resulting dust temperature is probably close to a lower limit since it is likely that $2 \leq n \leq 1$ (see Section 6.3). If $n = 1$ is chosen instead, the derived dust temperature would be about 10 K higher, and the corresponding total infrared luminosity would be about 50% higher. The qualitative nature of the argument in the last paragraph, i.e., the average interstellar radiation is not sufficiently bright to heat the dust to the observed temperature, is still valid.

C) Models of the Diffuse Far-Infrared Emission.

A few models for the diffuse submillimeter emission of

the Galaxy have been proposed. The early prediction approach of Fazio and Stecker (1976), which assumed similar distributions of dust and molecular CO, is supported by the observational similarity of the submillimeter and ^{12}CO emission profiles. In this model, a nominal dust temperature of 10 K was adopted. The choice of this parameter was based on the assumption that the average dust temperature is slightly higher than the average molecular gas temperature of 7 K reported by Scoville and Solomon (1975). More recent ^{12}CO survey results indicate that the molecular gas temperature is probably closer to 15 K (Solomon, P. M., private communication), so that the corresponding dust temperature is expected to be higher than 10 K. If a revised dust temperature of 20-30 K is adopted in the modeling approach of Fazio and Stecker (1976), the predicted diffuse infrared flux level would be consistent with the observational results presented in this thesis.

Mezger (1978) and Drapatz (1979), on the other hand, both consider the infrared radiation from the energetics side. Mezger (1978) interprets the diffuse far infrared as arising from dust absorption of photons from O stars. He estimates that 20 % of all O stars in the Galaxy are embedded inside radio HII regions, while the remaining 80 % are outside and contribute to the ionization of an extended low density (ELD) HII region. From consideration of the

observed infrared excess ratio, he argues that the observed infrared flux can be adequately accounted for by dust absorption of: 1) all photons of O stars embedded in compact HII regions (20 % of L_{IR}), 2) 30 % of the Lyc photons and 50 % of nonionizing photons from O stars in the ELD HII regions (40 % of L_{IR}) and 3) the interstellar radiation field (40 % of L_{IR}). A key feature according to his interpretation is that dust grains in the ELD HII region absorb 5 to 10 times more energy than they would absorb in the neutral, general interstellar radiation field, resulting in a dust temperature of 30 to 50 % higher. This is consistent with the observationally derived dust temperature. However, the idea of an extended, low density, hotter dust emission region accounting for about half of the observed radiation appears not to be compatible with the observed brightness contrast in the submillimeter emission and the inferred clumpy distribution of dust and gas (Section 6.3.1). A more detailed emission profile of the ELD HII region is needed to provide stronger support for a correlation with the submillimeter profile.

Drapatz (1979) models the submillimeter emission based on his projected distribution of dust and early-type, medium-age, and late-type stars. His derived far-infrared intensity is in general agreement with the observational results of this survey. Considering the close spatial

association of the submillimeter emission peaks with HII emission centers, his model appears to underestimate the importance of dust heating in HII regions.

One major difficulty with these models is that the number of free parameters is much more than the number of observational parameters available, so that it is difficult to arrive at a set of relatively firm conclusion on the distribution and properties of the luminosity sources. In this respect, the present observational results provide much more spatial and spectral information that is useful for constructing improved models on the large scale infrared emission from the Galaxy.

TABLE 6.1

Observed and Derived Paramters for Selected Sub-mm Peaks

Sub-mm PEAK DESIGNATION	RA (1950)	DEC (1950)	PEAK FLUX CH.1	PEAK FLUX CH.2	PEAK FLUX CH.3	DUST TEMPERATURE n=1	DUST TEMPERATURE n=2	TOTAL FLUX n=1	TOTAL FLUX n=2	$\langle\tau\rangle$	M_d
			($\times 10^{-5}$ w m^{-2} sr^{-1})			(K)		($\times 10^{-5}$ w m^{-2} sr^{-1})		($\times 10^{-3}$)	($\times 10^{-3}$ gm cm^{-2})
[1]	[2]		[3]			[4]		[5]		[6]	[7]
G10.1-0.4	18^h 6^m 20^s	-20^d 22^m	9.27	1.89	0.82	35(32,39)	23(21,25)	36(30,45)	25(21,29)	6.5	1.0
G10.6-0.4	18 07 11	-20 0	6.82	1.53	1.01*	32(29,34)	21(20,22)	23(19,25)	15(14,17)	9.5	1.6
G12.8-0.2	18 11 12	-18 0	11.1	2.02	0.74	40(37,42)	25(24,26)	59(49,66)	36(34,39)	4.8	.74
G16.7-0.3	18 19 15	-14 37	4.56	0.96	0.56	34(29,39)	22(20,24)	15(12,17)	11(9,13)	4.8	.77
G16.9+0.9	18 15 31	-13 43	4.44	0.65	0.30	54(40,75)	28(24,34)	50(22,135)	17(13,30)	1.6	.24
G18.0+2.0	18 14 2	-12 19	2.89	0.43	0.15	53(36,78)	28(23,34)	29(12,96)	11(8,19)	.78	.12
G18.2-0.3	18 22 16	-13 13	6.01	1.00	0.58	45(38,53)	26(24,28)	43(27,64)	22(17,24)	3.5	.53
G18.9-0.1	18 22 47	-12 31	6.44	1.18	0.70	39(35,44)	24(22,26)	33(26,44)	20(16,23)	5.0	.76
G19.5-0.2	18 24 17	-12 4	6.39	0.91	0.44	56(45,71)	29(26,33)	82(46,163)	27(22,38)	2.1	.33
G20.6-0.2	18 26 18	-11 4	4.95	0.76	0.30	50(40,65)	28(24,32)	45(26,99)	20(15,26)	1.6	.24
G21.4-0.2	18 27 48	-10 21	3.85	0.87	0.46	32(27,37)	21(19,23)	13(9,18)	9(7,10)	4.3	.70
G23.4-0.2	18 31 59	- 8 31	9.35	1.28	0.68	61(50,75)	30(28,33)	154(85,280)	43(37,55)	3.1	.47
G24.5+0.1	18 32 50	- 7 27	7.16	1.17	0.53	46(40,53)	26(24,28)	55(38,76)	25(21,30)	3.2	.49
G24.8+0.1	18 33 20	- 7 11	7.55	1.28	0.61	43(38,50)	26(24,28)	47(34,69)	26(22,30)	3.7	.66
G25.4-0.1	18 35 9	- 6 43	6.20	1.17	0.61	38(34,43)	24(22,26)	28(22,38)	18(15,21)	4.4	.66
G28.3+0.0	18 40 10	- 4 11	5.81	1.17	0.71	36(32,40)	23(21,25)	25(19,30)	16(13,18)	5.6	.87
G28.7+3.4	18 29 22	- 2 18	3.28	0.65	0.24	36(29,45)	23(20,26)	14(9,23)	9(7,11)	1.9	.30
G29.9-0.1	18 43 28	- 2 53	9.27	1.64	1.14	41(38,44)	25(24,26)	51(42,61)	29(27,32)	7.5	1.1
G30.7-0.1	18 45 11	- 2 13	15.4	2.84	1.55	39(37,41)	24(23,25)	73(66,85)	45(41,48)	11.	1.7
G33.4+0.1	18 49 26	+ 0 25	3.95	0.91	0.53	30(26,35)	20(18,23)	11(9,16)	8(7,10)	5.5	.92
G34.2+0.3	18 50 14	1 10	8.20	1.52	1.03	39(36,43)	24(23,26)	39(30,51)	24(22,28)	7.4	1.1
G34.5+0.2	18 51 16	1 25	3.86	0.91	0.56	29(26,34)	20(18,22)	10(9,14)	8(7, 9)	5.8	.98
G35.1-1.6	18 59 38	1 13	2.63	0.41	0.18	48(30,82)	28(21,34)	21(7,106)	10(6,17)	.95	.15
G37.5-0.1	18 57 38	4 4	4.11	0.72	0.39	42(33,53)	25(22,28)	24(14,45)	13(10,16)	2.6	.39
G39.1-0.2	19 0 39	5 22	2.67	0.65	0.46	29(24,35)	20(17,23)	7(5,10)	5(4, 7)	4.7	.79
G42.4-0.2	19 6 37	8 9	3.12	0.72	0.48	30(25,36)	20(18,23)	8(7,13)	6(5, 8)	4.9	.84
G43.2+0.1	19 7 42	9 7	6.04	1.59	0.68	27(24,30)	19(17,21)	15(12,17)	12(10,13)	7.7	1.3

* Noise glitch in data

NOTE : [1], [2] Positional uncertainties are typically less than 0.1 arc degree.
[3] Measured with one 10 arc min beam centered on the peak, statistical uncertainties are typically about 3×10^{-6}, 1×10^{-6}, 7×10^{-7} w m^{-2} sr^{-1} for the three channels respectively. The spectral response curves of the three channels are shown in Figure 2.11.
[4] Dust temperature estimate for emissivity indices n = 1 and 2. The numbers in parenthesis are the lower and upper limit corresponding to a 1σ uncertainty.
[5] Total IR flux estimate using temperature in column [4]. Lower and upper 1σ limits are enclosed in parenthesis.
[6] Average optical depth derived from Channel 3 flux, $\langle\tau_3\rangle = I_3 / \int B_\nu(T_d)\, g_{\nu 3}\, d\nu$, assuming n = 2.
[7] Dust column density derived from Channel 3 flux, assuming n = 2.

TABLE 6.2

Identification with Previously Observed Far Infrared Sources

Sub-mm Peak Designation (This work)	Previous Identification [1]	References [2]
G10.1-0.4	HFE 49? G10.0-0.1?	a
G10.6-0.4	G10.5-0.3	b
G12.8-0.2	HFE 50?, G12.8-0.3	a, b
G16.7-0.3	G16.9-0.2?	b
G16.9+0.9	G17.0+0.7?	b
G18.0+2.0	-	
G18.2-0.3	-	
G18.9-0.1	G18.8+0.0	b
G19.5-0.2	-	
G20.6-0.2	G20.5+0.1?	b
G21.4-0.2	-	
G23.4-0.2	G23.2-0.2	b
G24.5+0.1	G24.2-0.0?	b
G24.8+0.1	-	
G25.4-0.1	G25.5-0.2	b
G28.3+0.0	G28.4-0.2?	
G28.7+3.4	W40?	c
G29.9-0.1	HFE 56, G29.9-0.0	a, b
G30.7-0.1	HFE 57, G30.8-0.0	a, b
G33.4+0.1	G33.8-0.0?	b
G34.2+0.3	-	
G34.5+0.2	-	
G35.1-1.6	-	
G37.5-0.1	G37.8-0.3?	b
G39.1-0.2	-	
G42.2-0.2	G42.5-0.0?	b
G43.2+0.1	HFE 58, G43.2-0.0	a, d

Remarks:
[1] Within 0.2 degree of previously identified sources, except when followed by a '?' which indicates that the quoted position is between 0.2 to 0.5 degree away from our peak position. Those sub-mm sources not identified are at least 0.5 degree away from previously known infrared sources.

[2] (a) Hoffmann et al., 1971; (b) Nishimura et al., 1980; (c) Maihara et al., 1979; and (d) Furniss et al., 1975.

TABLE 6.3

Characteristics of Previous Far Infrared Surveys

Surveys	λ (μm)	Beam (aromin)	Minimum Detectable Flux (Jy)	Region of Coverage
This work	110-2000[a] 230-2000 270-2000	10 x 10	350 270 190	see Fig. 3.3
Boisse et al.[b] (1980)	71-95 114-196	24	2500	$0° < \ell < 85°$
Campbell et al. (1980)	60-120 75-120	12	650 200	$76° < \ell < 90°$
Nishmura et al.[c] (1980)	100-300	30	10^4	$352° < \ell < 45$
Maihara et al. (1979)	100 lowpass	42 x 60	10^5	$340° < \ell < 33°$
Owens et al. (1979)	400-1000 1000-3300	96	2×10^4	1/4 Celestial Sphere
Furniss et al. (1975)	40-350	4	1300	$327° < \ell < 349$ HII regions
Hoffmann et al. (1971)	80-135	12	10^4	$350° < \ell < 85°$ HII regions

Remarks: a) The pass band was 160-2000 μm in the second flight of the instrument.
b) same instrument as Serra et al., (1978); Ryter and Puget, (1977); and Rouan et al., (1977).
c) same instrument as Low et al., (1977).

TABLE 6.4
Comparison with CO Observational Results

Sub-mm PEAK DESIGNATION	CO PEAK DESIGNATION	$\int T_{CO}\, dV$ (K km s^{-1})	M_H/M_d	$I_{IR}/\int T_{CO} dV$ (x10-6 w m^{-2} sr^{-1}/K km s^{-1})	M/L (⊙)
[1]	[2]	[3]	[4]	[5]	[6]
G10.1-0.4	-	-	-	-	-
G10.6-0.4	-	-	-	-	-
G12.8-0.2	G12.75-0.25	177	181	2.0	0.058
G16.7-0.3	G16.63-0.13	113	112	0.97	0.12
G16.9+0.9	-	49	155	3.5	0.033
G18.0+2.0	-	-	-	-	-
G18.2-0.3	G18.13-0.25	114	163	1.9	0.62
G18.9-0.1	-	81	81	2.5	0.47
G19.5-0.2	-	81	186	3.30	0.35
G20.6-0.2	-	65	176	3.1	0.38
G21.4-0.2	-	98	106	0.92	0.13
G23.4-0.2	G23.38-0.25	184	297	2.3	0.051
G24.5+0.1	G24.38+0.13	171	265	1.5	0.078
G24.8+0.1	-	114	131	2.3	0.051
G25.4-0.1	G25.50-0.13	100	115	1.8	0.073
G28.3+0.0	-	98	86	1.6	0.073
G28.7+3.4	-	-	-	-	-
G29.9-0.1	G30.00-0.13	142	95	2.0	0.059
G30.7-0.1	-	130	58	3.5	0.033
G33.4+0.1	G33.38+0.00	130	107	0.62	0.19
G34.2+0.3	-	114	77	2.1	0.057
G34.5+0.2	G34.50+0.13	105	81	0.76	0.15
G35.1-1.6	-	-	-	-	-
G37.5-0.1	G37.50+0.00	80	156	1.6	0.073
G39.1-0.2	-	52	50	0.96	0.12
G42.2-0.2	G42.38-0.25	60	54	1.0	0.12
G43.2+0.1	G43.25+0.00	58	33	2.1	0.056

Note : [1] Positional uncertainties are typically less than 0.1 degree.
[2],[3] Peak Designations and integrated line intensities from CO survey maps of Dame, Cohen & Thaddeus (1980), with a 7.5 arc min beam and a sampling interval of one beam width in Galactic longitude and latitude.
[4] Hydrogen-to-Dust mass ratio, $M_H = M(HI + H_2)$, and assuming hydrogen column density $N_H = 4.6 \times 10^{20} \int T_{CO}\, dV \;\; cm^{-2}$
[5] Total infrared flux to integrated CO line intersity ratio, assuming dust emissivity index n=2.
[6] Hydrogen mass-to-IR luminosity ratio

TABLE 6.5

Comparison with 5-GHz Observational Results

Sub-mm PEAK DESIGNATION	5 GHz OBSERVED PEAK POSITION	PARAMETERS FLUX (Jy)	SIZE (')	IRE	D_S (kpc)	R	OTHER NAME
[1]	[2]	[3]	[4]	[5]	[6]		
G10.1-0.4	G10.16-0.35	43	3.5	3.0	5.1	5.1	W31
G10.6-0.4	G10.62-0.38	8	3.2	10.5	5.1	5.1	
G12.8-0.2	G12.81-0.20	34	2.8	5.7	4.5	5.7	W33
G16.7-0.3	G16.62-0.32	4	-	16.4	-	-	
G16.9+0.9	G16.94+0.95	32	5.6	1.0	2.7	7.5	M16
G18.0+2.0	G18.9 +1.9	4	7	7.5	-	-	
G18.2-0.3	G18.14-0.29	12	4.0	5.7	4.6	5.8	RCW166
G18.9-0.1	G18.87-0.18	-	-	large	-	-	
G19.5-0.2	G19.60-0.24	10	2.9	12.2	4.0	6.4	
G20.6-0.2	G20.70-0.09	12	4.5	5.9	13.8	5.7	
G21.4-0.2	-	-	-	large	-	-	
G23.4-0.2	G23.42-0.21	12	3.8	15.2	7.5	4.3	W41
G24.5+0.1	G24.48+0.21	6	-	12.1	-	-	W42 ?
G24.8+0.1	G24.81+0.10	10	4.0	10.1	7.7	4.4	W42 ?
G25.4-0.1	G25.38-0.18	20	3.7	4.5	13.4	6.1	3C385
G28.3+0.0	-	8	5.0	4.8	-	-	
G28.7+3.4	G28.8 +3.5	28	6	1.6	0.1	10	W40
G29.9-0.1	G29.94-0.04	18	4.5	7.7	7.3	5.2	
G30.7-0.1	G30.78-0.03	74	4.1	2.6	7.0	5.4	W43
G33.4+0.1	-	-	-	large	-	-	
G34.2+0.3	G34.30+0.14	14	2.7	9.5	3.8	7.2	NRAO584
G34.5+0.2	-	0.1	-	large	-	-	
G35.1-1.6	G35.2 -1.7	14	-	4.3	3.3	7.6	W48
G37.5-0.1	G37.53-0.11	8	5.0	5.3	11.9	7.3	W47
G39.1-0.2	-	8	-	3.4	-	-	3C396SNR?
G42.4-0.2	G42.43-0.26	4	2.7	3.9	-	-	
G43.2+0.1	G43.17+0.00	48	3.3	1.4	13.8	9.4	W49

Note : [1] Positional uncertainties are typically less than 0.1 degree
[2], [4] Source Designations and size from 5 GHz survey maps of Altenhoff *et al.* (1978), with beam size = 2'.6 and positional uncertainty = 0'.3. For sources with b >1°, the positions are from Altenhoff *et al.*, (1970).
[3] 5 GHz flux measured with an 11' beam from Altenhoff *et al.* (1970).
[5] Infrared Excess IRE = $L_{IR} / N_c' h\nu_a$, see Section 6.3.
[6] Distance from Wilson *et al.* (1972), Wilson (1974), Churchwell *et al.* (1978) or Reifenstein *et al.* (1970).

TABLE 6.6
Spectral Type and Luminosity Estimate

SUB-mm PEAK DESIGNATION	SPECTRAL TYPE SP(IRE)	L(SP) (O)	L(IR) (O)	REMARK
G10.1-0.4	<O4	$>1.3\times10^{6}$	1.6×10^{6}	1
G10.6-0.4	O9	4.6×10^{4}	9.8×10^{5}	1
G12.8-0.2	O7	1.0×10^{5}	1.8×10^{6}	1
G16.7-0.3	B0	2.5×10^{4}	-	
G16.9+0.9	<O4	$>1.3\times10^{6}$	3.1×10^{5}	3
G18.0+2.0	O8	6.5×10^{4}	-	
G18.2-0.3	O7	1.0×10^{5}	1.2×10^{6}	1
G18.9-0.1	<O4	$>1.3\times10^{6}$	-	
G19.5-0.2	O9	4.6×10^{4}	1.1×10^{6}	1
G20.6-0.2	O7	1.0×10^{4}	-	
G21.4-0.2	<O4	$>1.3\times10^{6}$	-	
G23.4-0.2	B0	2.5×10^{4}	6.1×10^{6}	1
G24.5+0.1	O9	4.6×10^{4}	-	
G24.8+0.1	O9	4.6×10^{4}	3.8×10^{6}	1
G25.4-0.1	O6	2.5×10^{5}	8.1×10^{6}	1
G28.3+0.0	O6	2.5×10^{5}	-	
G28.7+3.4	<O4	$>1.3\times10^{6}$	2.3×10^{2}	3
G29.9-0.1	O9	4.6×10^{4}	3.9×10^{6}	1
G30.7-0.1	<O4	$>1.3\times10^{6}$	5.5×10^{6}	
G33.4+0.1	<O4	$>1.3\times10^{6}$	-	
G34.2+0.3	O9	4.6×10^{4}	8.7×10^{5}	1
G34.5+0.2	<O4	$>1.3\times10^{6}$	-	
G35.1-1.6	O6	2.5×10^{5}	2.7×10^{5}	2
G37.5-0.1	O6	2.5×10^{5}	4.6×10^{6}	1
G39.1-0.2	O4	1.3×10^{6}	-	
G42.2-0.2	O5	6.8×10^{5}	-	
G43.2+0.1	<O4	$>1.3\times10^{6}$	5.7×10^{6}	

Remarks: 1) $L_{IR} > L(SP)$
2) $L_{IR} \approx L(SP)$
3) $L_{IR} < L(SP)$

FIGURE CAPTIONS

Figure 6.1 Contour maps of the submillimeter wave emission from the Galactic plane in the three wavelength bands with cut-on wavelengths at 110 μm (top, Channel 1), 230 μm (middle, Channel 2) and 270 μm (bottom, Channel 3). The contour levels are in data units of 2, 4, 8, 12, 16, 20, 24, 28, and 32 for Ch. 1, and 1, 2, 3, 4, 5, 6, 7 for Ch. 2 and Ch. 3, where each data unit represents a surface brightness of 4.0×10^{-6}, 2.7×10^{-6}, and 2.0×10^{-6} w m^{-2} sr^{-1} for the three channels respectively. The typical statistical uncertainty associated with the contour levels is 3×10^{-6}, 1×10^{-6}, and 7×10^{-7} w m^{-2} sr^{-1} for the three channels respectively.

Figure 6.2 The submillimeter surface brightness plotted against $\int T(^{12}CO)\, dV$ at the emission peak positions listed in Table 6.1.

Figure 6.3 The total infrared surface brightness plotted against $\int T(12CO)\, dV$ at the emission peak positions.

Figure 6.4 The ratio of the stellar luminosity to Lyα luminosity as a function of spectral type. The data is obtained from the tables of Panagia (1973).

Figure 6.5 The infrared excess ratio at the emission peak positions as a function of galacto-centric distance.

Figure 6.6 The longitudinal emission profile in the three channels, obtained by integrating the surface brightness over the entire latitude range. The typical uncertainty in the profile is approximately 20, 7, and

5×10^{-10} w m^{-2} deg^{-1} in the three channels respectively. The uncertainty is slightly higher at high longitudes where the emission is weaker.

Figure 6.7 The Ch. 1/ Ch.2 flux ratio and dust temperature profile as a function of longiude. The uncertainty in the flux ratio is about ± 1, and somewhat higher at high longitudes where the submillimeter emission is weaker.

Figure 6.8 A comparison of the Ch. 1 submillimeter emission profile with the $\int T(^{12}CO)\, dV$ intensity profile. Both profiles are integrated over the same latitude range of ± 1 degree. The ordinate at the right margin denotes the submillimeter surface brightness in units of 10^{-9} w m^{-2} deg^{-1}, while the ordinate at the left margin denotes the CO intensity in units of 10 K km s^{-1} deg. The CO data are from Dame et al., (1980).

Figure 6.9 The Ch. 1 submillimeter to CO surface brightness ratio and a histogram showing the distribution of the brightness ratio. The ratios are in units of 10^{-7} w m^{-1} sr^{-1}/K km s^{-1}.

Figure 6.10 The gas-to-dust mass ratio profile.

Figure 6.11 The 7.5 arc minute beam filling factor as a function of longitude obtained by a comparison of the dust and CO antenna temperature.

Figure 6.12 Comparison of the submillimeter emission profile with those of other galactic constituents.

Figure 6.13 The infrared excess ratio profile.

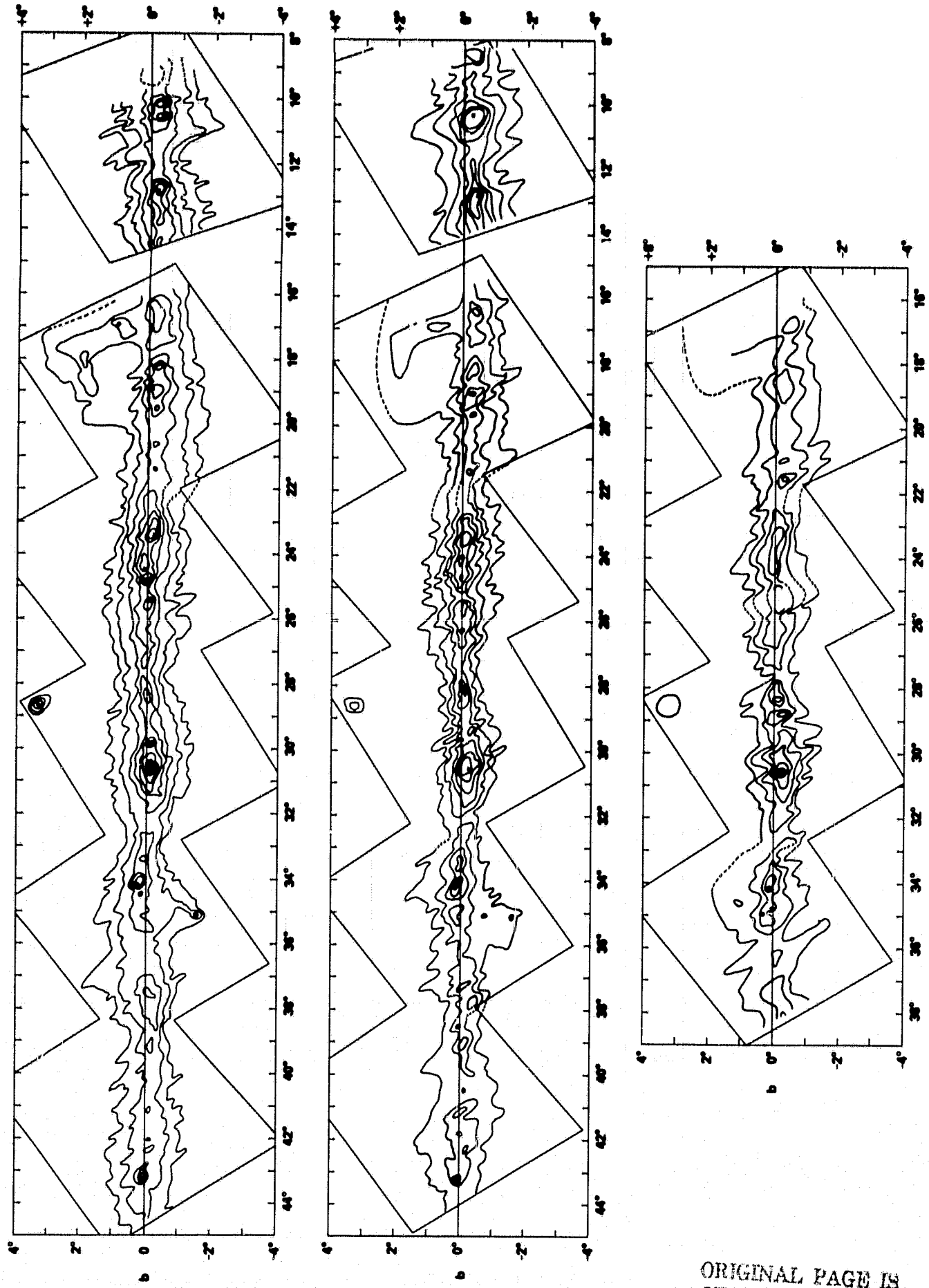

FIGURE 6.1

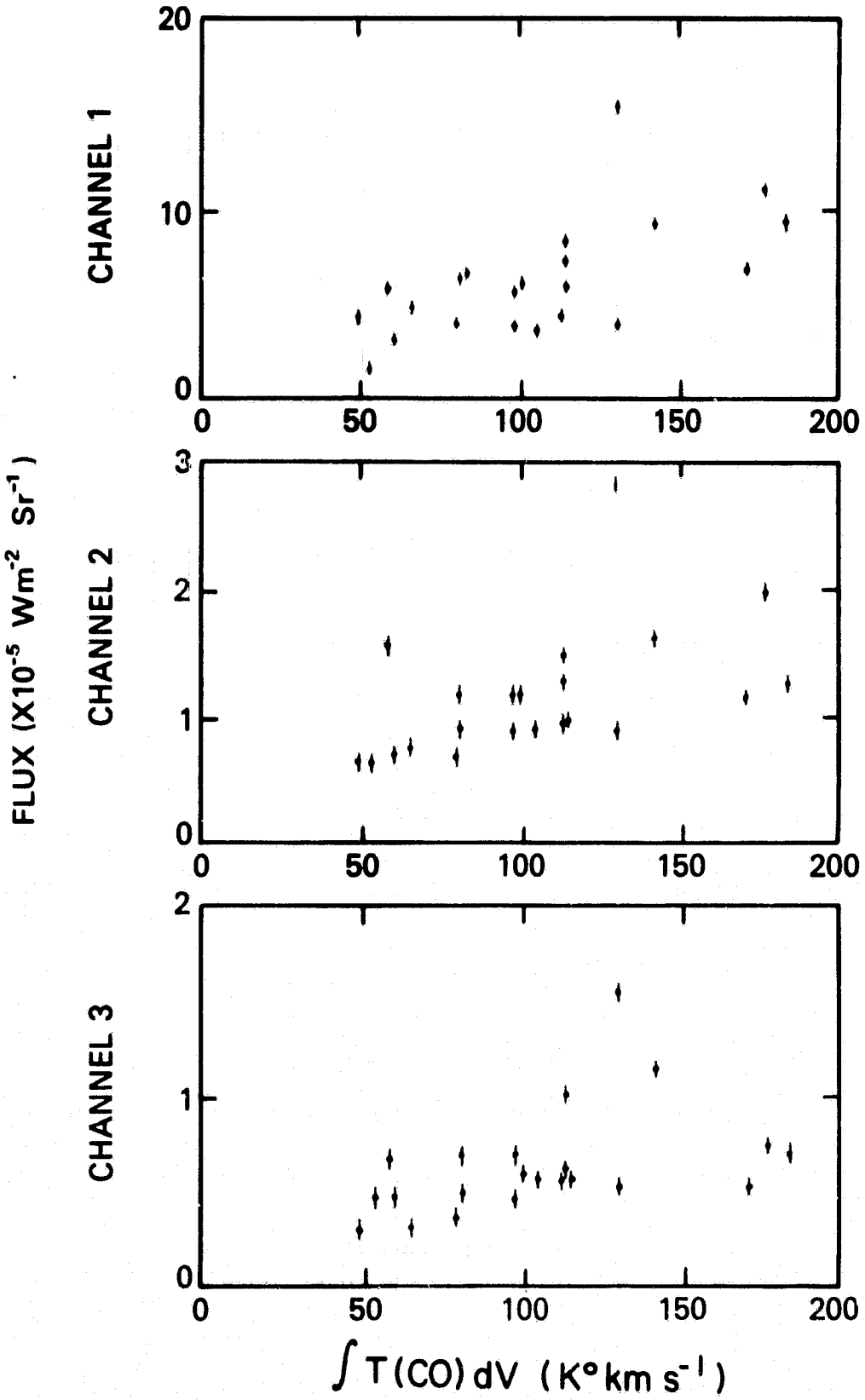
CHANNEL 1
CHANNEL 2
CHANNEL 3
FLUX (X10⁻⁵ Wm⁻² Sr⁻¹)
∫ T(CO) dV (K° km s⁻¹)
0
50
100
150
200
10
20
1
2
3

FIGURE 6.2

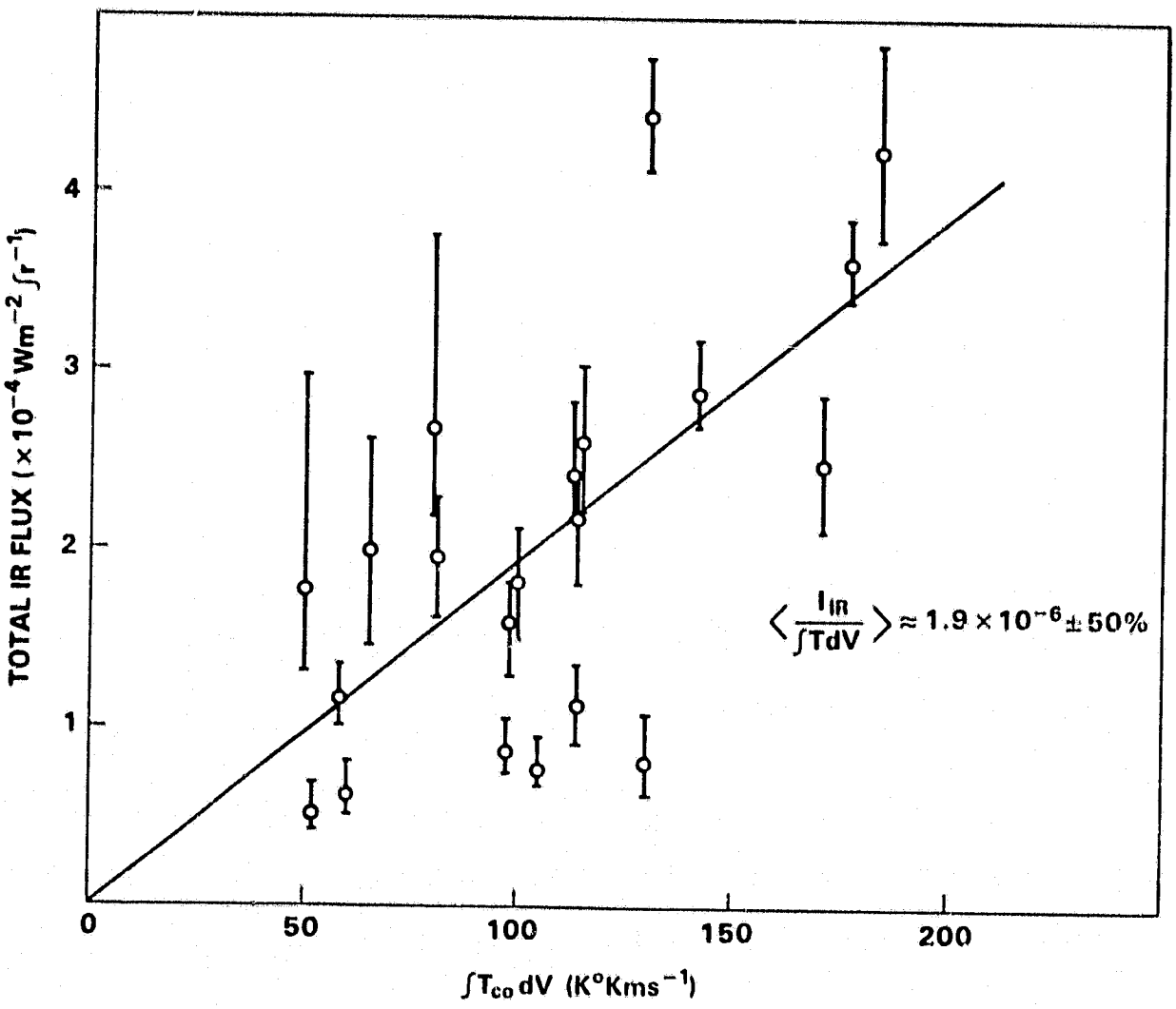
TOTAL IR FLUX ($\times 10^{-4} Wm^{-2} sr^{-1}$)
4
3
2
1
0
50
100
150
200
$\int T_{co}\, dV$ ($K°Kms^{-1}$)
$\left\langle \frac{I_{IR}}{\int T dV} \right\rangle \approx 1.9 \times 10^{-6} \pm 50\%$

FIGURE 6.3

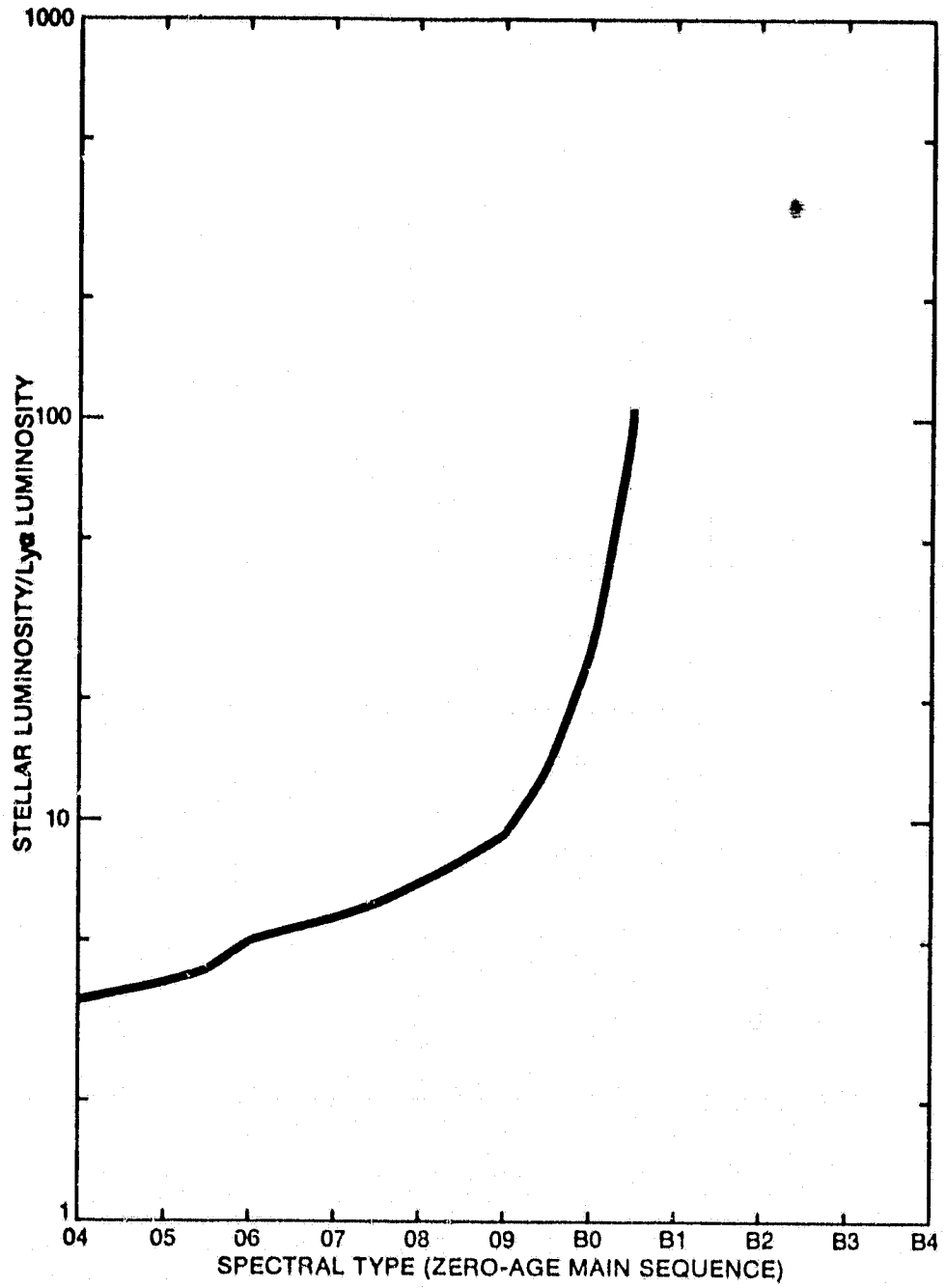
1000
100
10
1
STELLAR LUMINOSITY/Lyα LUMINOSITY
04
05
06
07
08
09
B0
B1
B2
B3
B4
SPECTRAL TYPE (ZERO-AGE MAIN SEQUENCE)

FIGURE 6.4

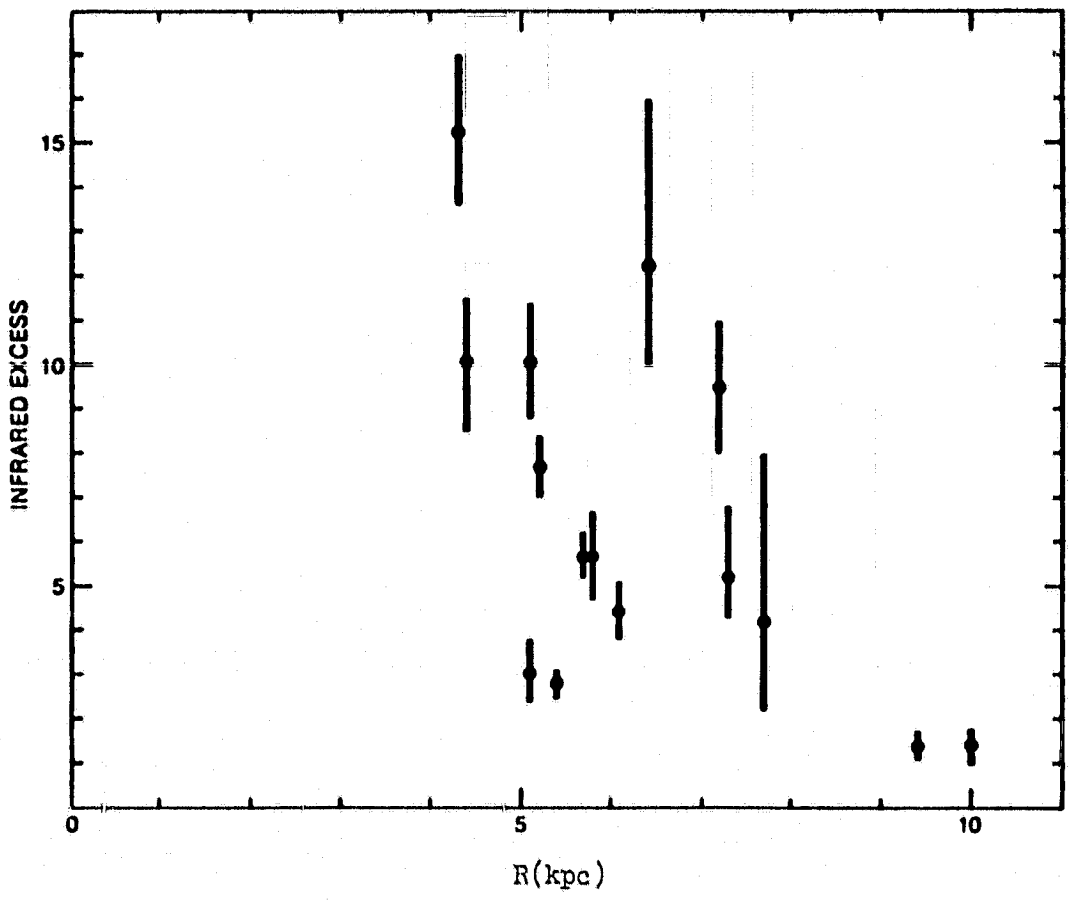

FIGURE 6.5

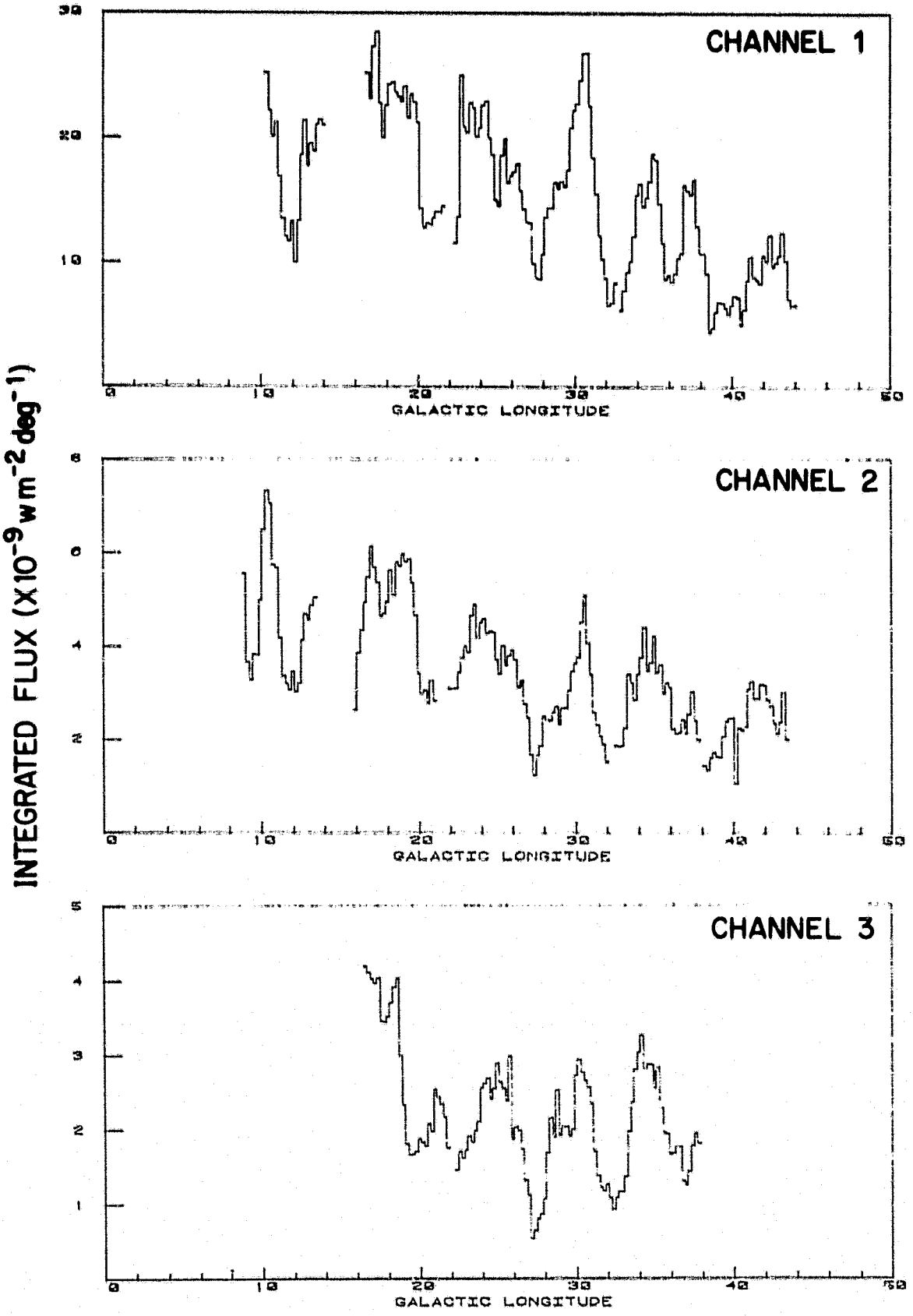
CHANNEL 1
CHANNEL 2
CHANNEL 3
INTEGRATED FLUX (X10^{-9} w m^{-2} deg^{-1})
GALACTIC LONGITUDE
GALACTIC LONGITUDE
GALACTIC LONGITUDE

FIGURE 6.6

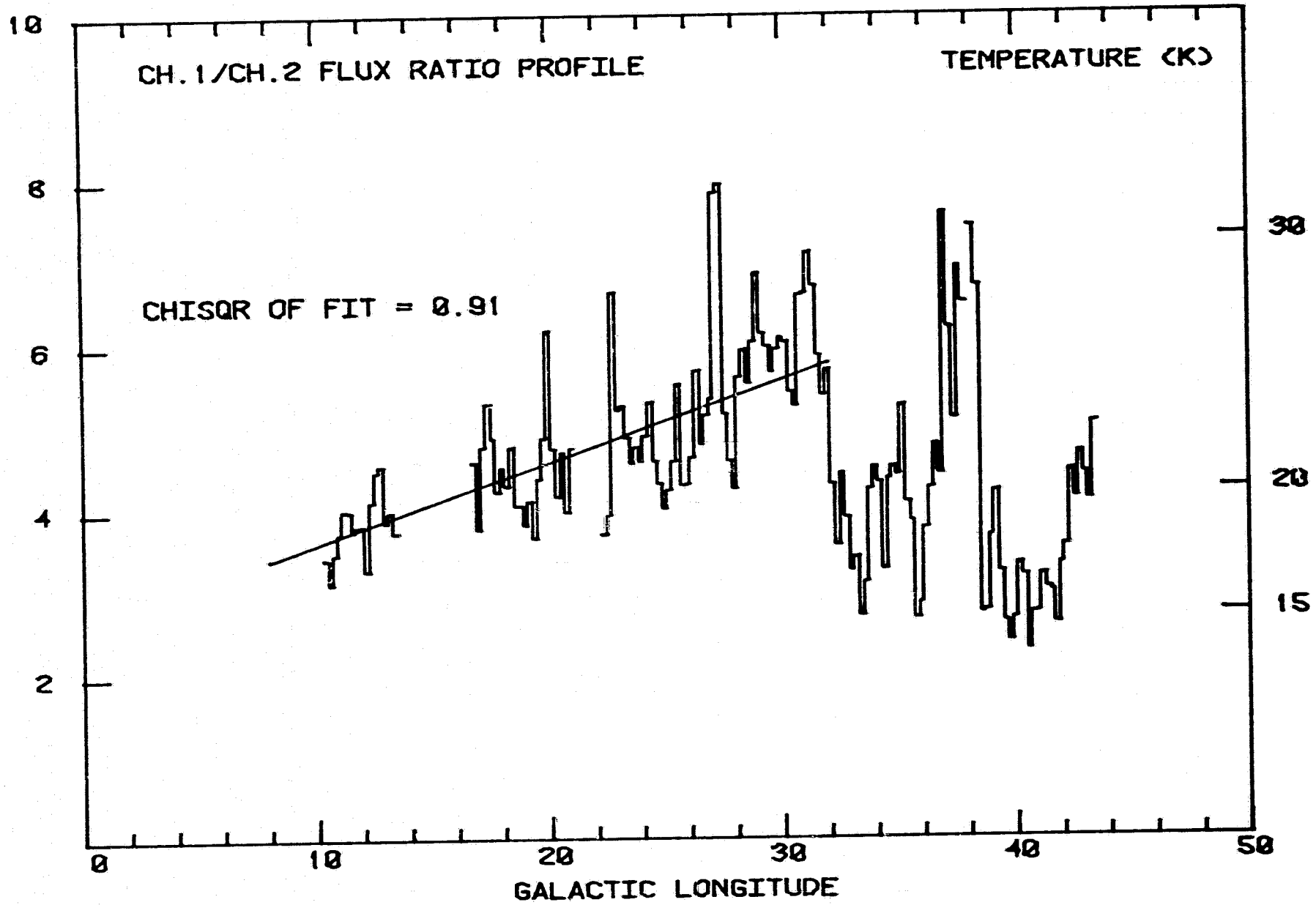
CH.1/CH.2 FLUX RATIO PROFILE
TEMPERATURE (K)
CHISQR OF FIT = 0.91
10
8
6
4
2
30
20
15
0
10
20
30
40
50
GALACTIC LONGITUDE

FIGURE 6.7

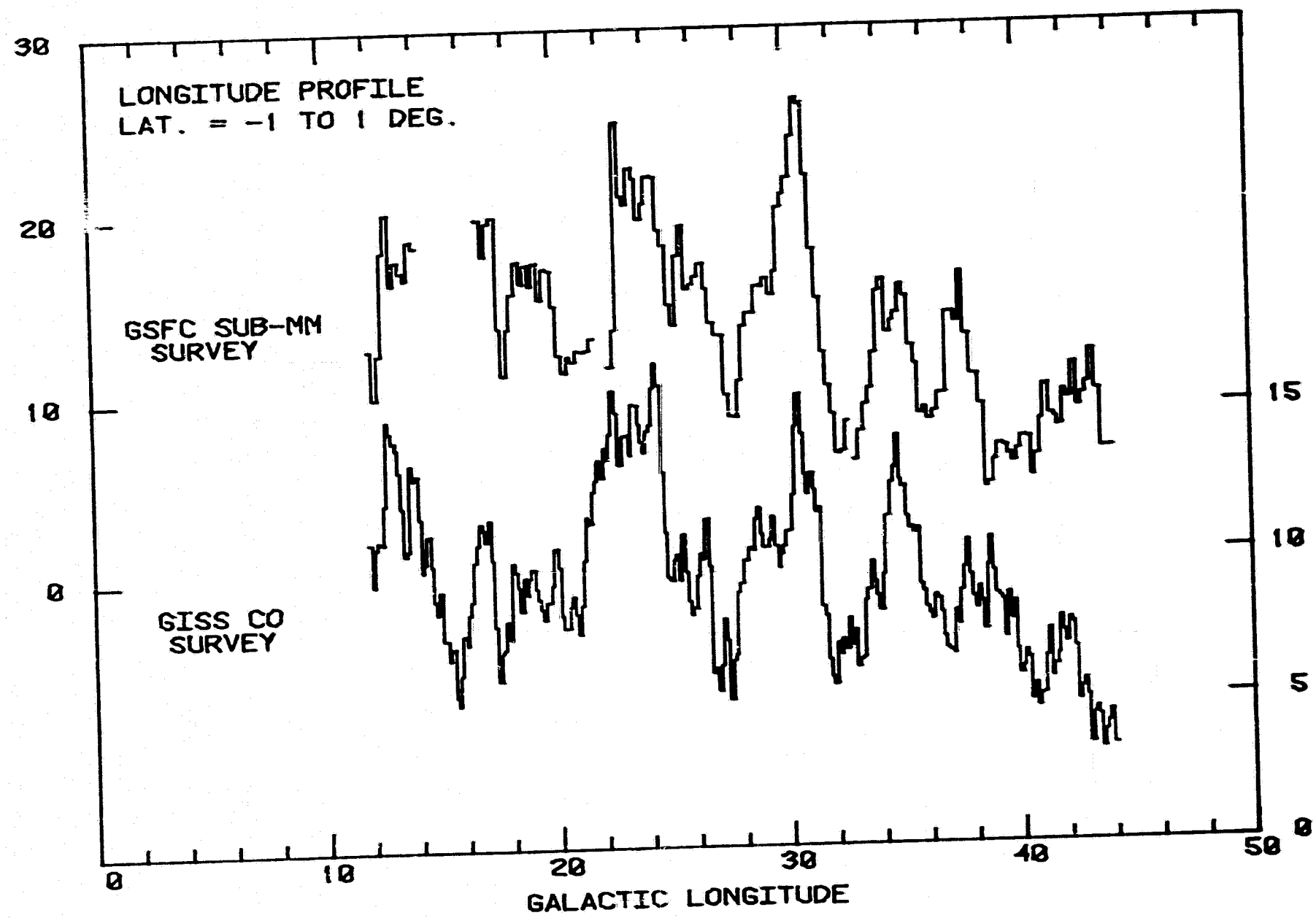
LONGITUDE PROFILE
LAT. = -1 TO 1 DEG.
GSFC SUB-MM SURVEY
GISS CO SURVEY
30
20
10
0
15
10
5
0
0
10
20
30
40
50
GALACTIC LONGITUDE

FIGURE 6.8

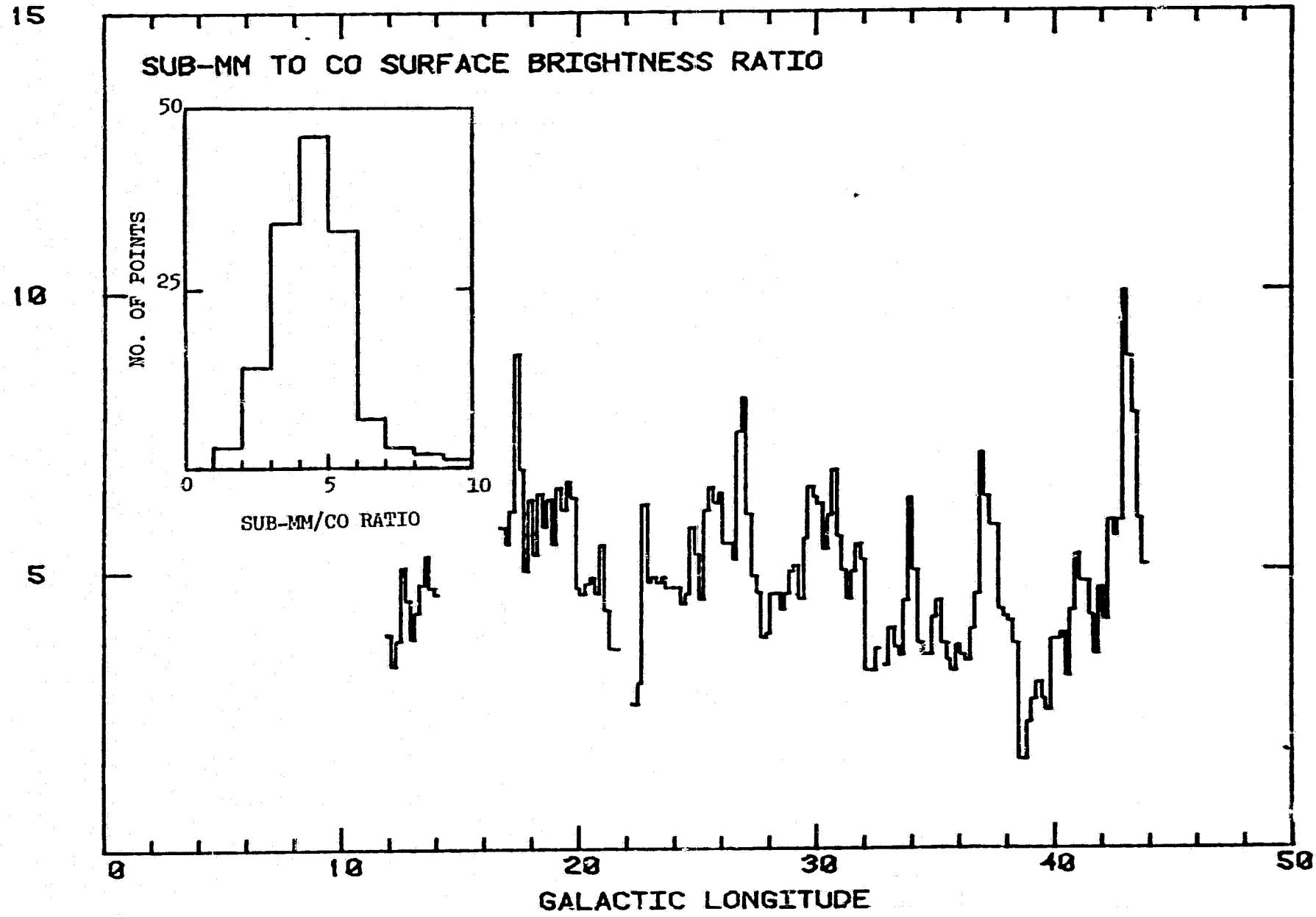
SUB-MM TO CO SURFACE BRIGHTNESS RATIO
NO. OF POINTS
50
25
0
5
10
SUB-MM/CO RATIO
15
10
5
0
10
20
30
40
50
GALACTIC LONGITUDE

FIGURE 6.9

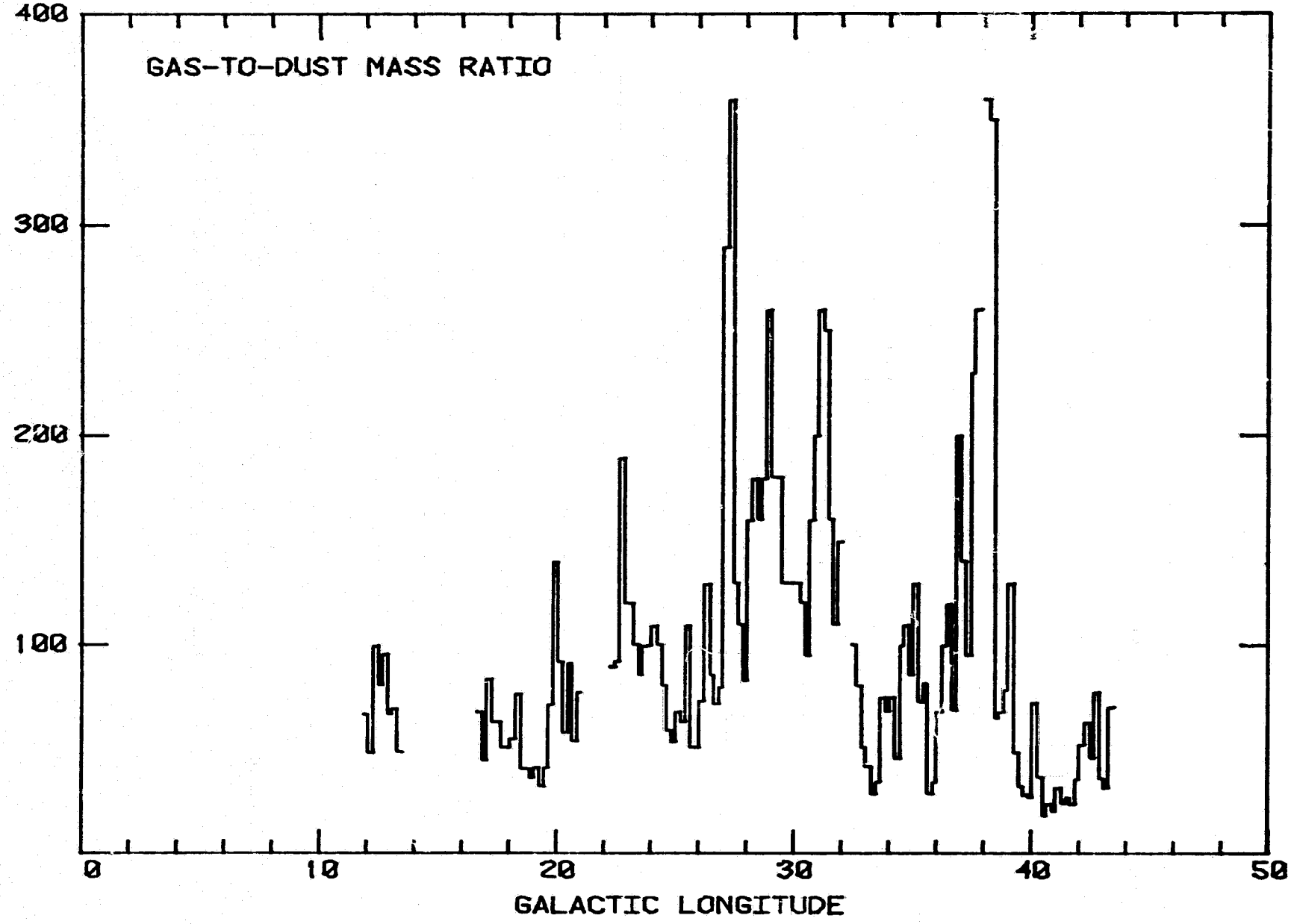
GAS-TO-DUST MASS RATIO
400
300
200
100
0
10
20
30
40
50
GALACTIC LONGITUDE

FIGURE 6.10

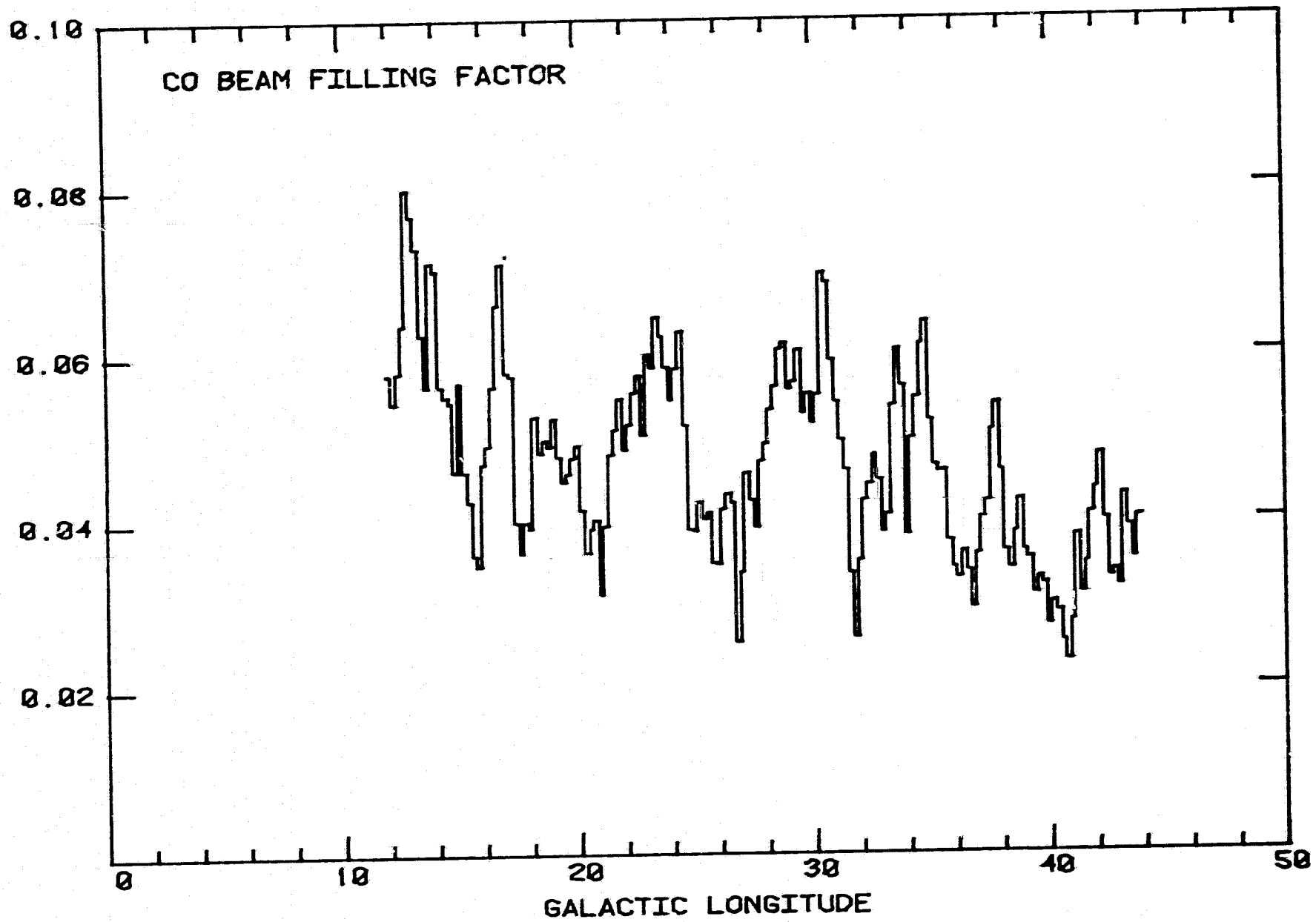
0.10
CO BEAM FILLING FACTOR
0.08
0.06
0.04
0.02
0
10
20
30
40
50
GALACTIC LONGITUDE

FIGURE 6.11

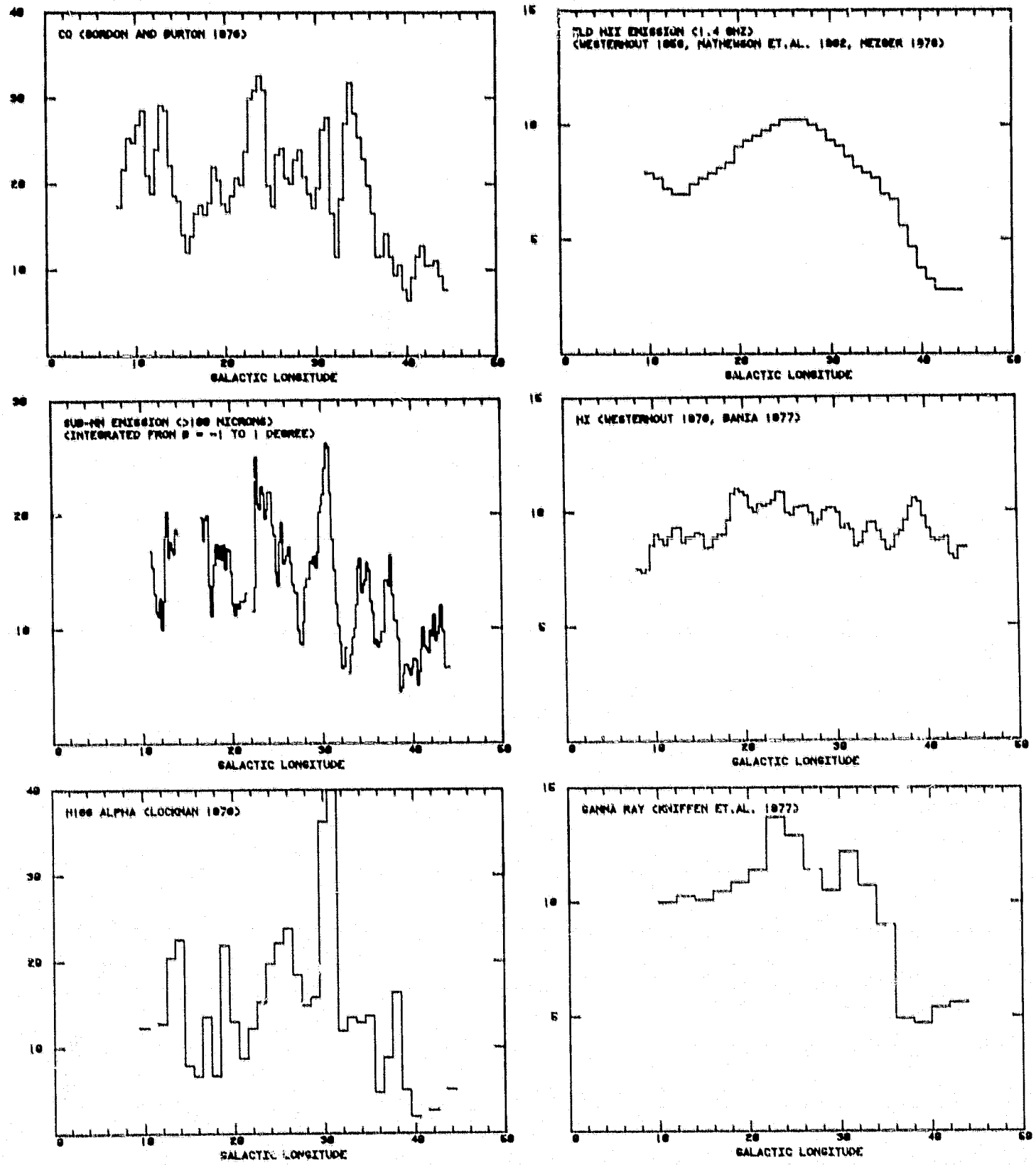
CO (BORDON AND BURTON 1976)
GALACTIC LONGITUDE
GALACTIC LONGITUDE
SUB-MM EMISSION (>100 MICRONS)
INTEGRATED FROM B = -1 TO 1 DEGREE)
GALACTIC LONGITUDE
HI (WESTERHOUT 1970, BANIA 1977)
GALACTIC LONGITUDE
H166 ALPHA (LOCKMAN 1976)
GALACTIC LONGITUDE
GAMMA RAY (HOFFEN ET.AL. 1977)
GALACTIC LONGITUDE

FIGURE 6.12

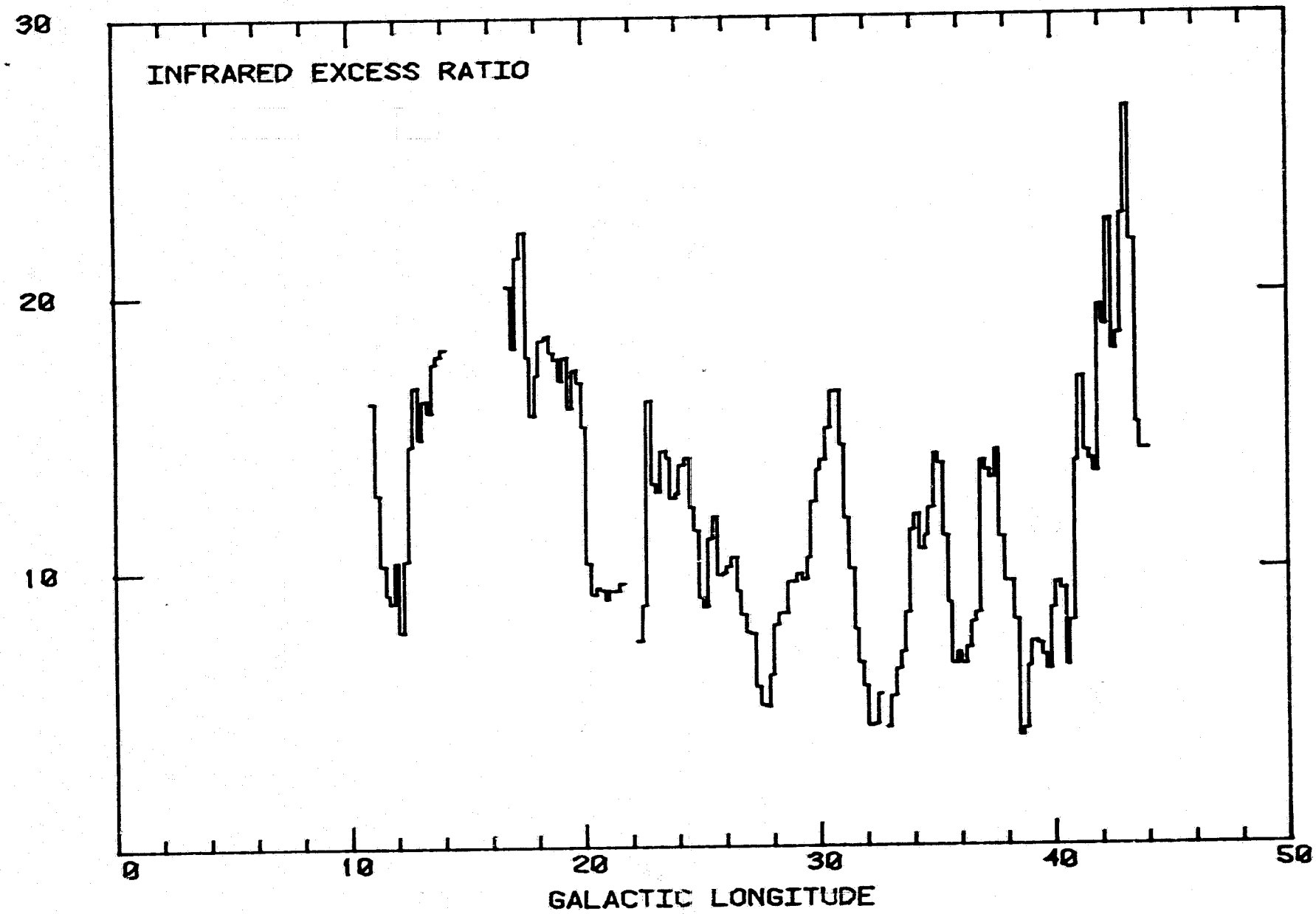
30
INFRARED EXCESS RATIO
20
10
0
10
20
30
40
50
GALACTIC LONGITUDE

FIGURE 6.13

CONCLUSION

The development of the Submillimeter Wave Sky Survey Observatory was discussed. The first two flights of this Observatory returned a large volume of scientific data. Preliminary analysis of a segment of the observational data covering the Galactic plane region from $\ell = 8°$ to $44°$ was presented. The results have contributed new information on the distribution and physical conditions of dust clouds on a Galactic scale. The large scale submillimeter emission profile was found to be almost observationally equivalent to that of the ^{12}CO $J = 1-0$ emission integrated over all velocities, indicating a close association of dust and molecular gas. A small positive gradient in the dust temperature from $\ell = 8°$ to $\ell = 32°$ may be present. This gradient suggests an order-of-magnitude increase in the average interstellar radiation density toward $\ell = 30°$ if the dust emissive properties are uniform over this longitude range. Clearly a more detailed overall picture of the Galaxy at submillimeter wavelenghts will emerge when the survey is completed.

APPENDIX A DERIVATION OF DUST EMISSION PROPERTIES

In a simple model of a dust cloud with dust grains at equilibrium temperature T_d, and spectral optical depth τ_ν, the thermal blackbody radiance emitted in our wavelength bands from the dust cloud is :

$$I = \int B_\nu(T_d)\, g_\nu\, (1-e^{-\tau\nu})\, d\nu \qquad (A1)$$

where $B_\nu(T_d)$ is the Planck function, g_ν is the spectral response of the instrument normalized to its peak. The optical depth, τ_ν, is related to the dust density and emissivity by :

$$\tau_\nu = \pi a^2\, \epsilon_\nu\, N_d \qquad (A2)$$

$$= 3/4\, (M_d/a\rho_d)\, \epsilon_\nu \qquad (A3)$$

where N_d is the dust grain column density, πa^2 is the dust grain cross sectional area, ϵ_ν is the dust grain emissivity, M_d is the dust mass column density and ρ_d is the dust grain mass density.

At submillimeter wavelengths, most dust clouds are optically thin, so that $1-\epsilon^{-\tau\nu} \approx \tau_\nu$. This is justified a posteriori by the derived optical depths, as well as by

the observed range of optical depth in other dust clouds at a wavelength of 1.0 mm (cf. Westbrook et al., 1976, Hildebrand et al., 1978, Cheung et al., 1978, 1980). The observed source spectrum can often be approximated by a greybody spectrum with a power-law frequency-dependent emissivity, $\epsilon_\nu \propto K\nu^n$, where K is a constant characteristic of the dust grain composition and n is the emissivity index, usually with value between 1 and 2. This observed range of spectral index n is consistent with theoretical calculations of dust grain emissivity (Aannestad 1975; Leung 1975). Using equations (A1) and (A3), the incident flux is given by

$$I = (3/4)\ (M_d/a\rho_d)\ K \int \nu^n\ B_\nu(T_d)\ g_\nu\ d\nu \qquad (A4)$$

and the average optical depth is

$$\langle\tau\rangle = I \Big/ \int B_\nu(T_d)\ g_\nu\ d\nu. \qquad (A5)$$

With a three-wavelength-channel photometer, the ratios of the incident fluxes in the different channels are :

$$I_1/I_2 = \int \nu^n\ B_\nu(T_d)\ g_{\nu 1}\ d\nu \Big/ \int \nu^n\ B_\nu(T_d)\ g_{\nu 2}\ d\nu \qquad (A6)$$

$$I_2/I_3 = \int \nu^n\ B\nu(T_d)\ g_{\nu 2}\ d\nu \Big/ \int \nu^n\ B_\nu(T_d)\ g_{\nu 3}\ d\nu \qquad (A7)$$

These ratios I_1/I_2 and I_2/I_3 are functions of the dust

temperature T_d and the spectral emissivity index n only, and are independent of the dust parameters a, ρ_d, M_d, and K. I have modelled these flux ratios as a function of T_d and n, using both an idealized spectral response and the measured spectral response of the photometer.

For the idealized case, the normalised spectral response is :

$$g_{\nu x} = 0 \quad \nu > \nu_x$$
$$= 1 \quad \nu \leq \nu_x$$

with cut-on frequencies ν_x at 3×10^{12} Hz, 2×10^{12} Hz, and 1×10^{12} Hz for the three channels respectively. The flux ratios are plotted against each other in a color-color diagram in Figure A1, which indicates that the photometer with these three bands provides a satisfactory means for determining the value of T_d and n. Unfortunately, the actual measured spectral response in Channel 2 of the photometer has a cut-on wavelength much too close to that of Channel 3 due to a manufacturing error which was not discovered until after the flight. The resulting color-color diagram (Figure A2), derived from the measured spectrum, does not provide significant discrimination for determining simultaneously the parameters T_d and n. This error was remedied for the second flight on August 1980. One can, however, still assume a value of n in order to

estimate T_d. The flux ratios as a function of the temperature T_d and emissivity index n are shown in Figure A3, for the cases n = 0, 1, and 2.

I have chosen to derive the value of T_d for the sources in Table 6.1 using the two cases of the emissivity index n=1 and n = 2. The results, shown in Table 6.1, then represent a range of probable dust temperature. For n = 1, T_d = 30 to 50 kelvin; and for n =2, T_d = 20 to 30 kelvin. The uncertainty of the dust temperature for each case of n is in general only a few degrees. The upper and lower 1σ limits for the temperature estimate are shown in parenthesis in Table 6.1.

Using the derived dust temperature T_d, the expected total emission over all frequencies is related to the flux received in one channel by

$$I_{total} / I = \int \nu^n B_\nu(T_d)\, d\nu \,/\, \int \nu^n B_\nu(T_d)\, g_\nu\, d\nu \qquad (A8)$$

This ratio is a function of T_d and n only and is independent of other dust parameters. The flux in Channel 1, the channel with the shortest cut-on wavelength at 100 μm, was used for estimating the total infrared flux. A graph showing the I_{total} / I as a function of T_d and n is plotted in Figure A3.

The dust mass column density, M_d, expressed in terms of T_d and the measured flux I, is given by :

$$M_d = (4/3)\ (a\rho_d/K)\ \ (I\ /\ \int \nu^n\ B_\nu(T_d)\ g_\nu\ d\nu) \qquad (A9)$$

Note that in the above analysis, I have used a single set of dust grain parameters. In reality, it is almost certain that a mixture of dust grains with a distribution of sizes and emissive properties must be present in the interstellar medium. The grain materials are generally thought to include graphite, iron, and other materials with or without mantles of ice and other C,N,O compounds. Several attempts have been made to estimate the dust emissive properties for different types of grain material (e.g. Purcell, 1969; Werner and Salpeter, 1969; Knacke and Thompson, 1973; Aanestad, 1975; Leung, 1975). Their results could at best provide an order of magnitude estimate on the quantity $a\rho_d/K\nu^n$. The present observations do not provide the details for or warrant separate considerations of the different grain types. On the assumption that dust clouds are composed of similar types and mix of dust grain materials, it is sufficient to treat the dust mixture by the choice of a single set of mixture-averaged parameters. With this restriction in mind, I have adopted the following nominal values for the dust grain parameters:

$$\kappa_\nu = K\nu^2 \qquad \text{(A10)}$$

$$K/a = 1 \times 10^{-23} \ \text{cm}^{-1}\ \text{Hz}^{-2} \qquad \text{(A11)}$$

$$\rho_d = 1 \ \text{gm cm}^{-3}. \qquad \text{(A12)}$$

The same set of values was previously used in 1.0-mm continuum observations of molecular clouds (Westbrook et al., 1976; Elias et al., 1978 ; Cheung et al., 1978, 1980) so that direct comparisons with those results may be made. The value of K/a adopted here is a factor of 4 higher than that adopted by Hildebrand et al., (1978), with the same assumed value of n = 2.

Using the nominal values in equations (A10), (A11), and (A12), the dust column density may be expressed as :

$$M_d \approx 1.2 \times 10^{23} \ I \ / \int \nu^2 B_\nu(T_d)\ g_\nu \ d\nu \quad (\text{gm cm}^{-2}) \qquad \text{(A13)}$$

It is noteworthy that for the dust temperature range between 20-30 K, $x=h\nu/kT$ is of the order unity even in the longest wavelength channel, so that the full integral in equation (A13), rather than the Rayleigh-Jeans approximation, has to be evaluated. Under this condition, the derived dust column density is a sensitive function of temperature T_d. A graph showing the value of the integral function $\int \nu^2 B_\nu(T_d)\ g_{\nu 3}\ d\nu$ versus T_d is shown in Figure A3. For the range of dust temperature listed in Table 6.1 for n = 2, $T_d \approx$ 20-30 K, the

dust column density varies as $T_d^{-2.5}$. An uncertainty of ± 5 degree in dust temperature translates into an uncertainity in M_d of about 50 %. The dust column densities, derived from the Channel 3 fluxes for the emission peaks, are listed in Table 6.1.

FIGURE CAPTIONS

Figure A1: A color-color diagram for thermal sources with emission spectra of the form $I_\nu \propto \nu^n B_\nu (T)$, where $B_\nu (T)$ is the Planck function for temperature T. Both the ordinates and abscissa show the ratios of the intensities in the submillimeter bands with idealized long-wave pass characteristics. The solid curves shows lines of constant n and T.

Figure A2: Same as Figure A1, except that the ratios are calculated with the measured spectral response of the photometer. The lines of constant n and T are judged to be too close to permit simultaneous determination of both n and T.

Figure A3: a) Ratios of total infrared intensities to the intensities in Channel 1 as a function of temperature for thermal sources with the same form of emission spectra as in Figure A1, for the cases n = 0, 1, and 2.

b) The modeled ratios of intensities in Channel 1 and Channel 2 as a function of source temperature for n = 0, 1, and 2.

c) The modeled ratios of intensities in Channel 1 and Channel 3 as a function of source temperature for n = 0, 1, and 2.

d) The submillimeter intensities in Channel 3 as a function of source temperature for n = 2. This modeled intensity curve is used for determining the dust column density along a line of sight.

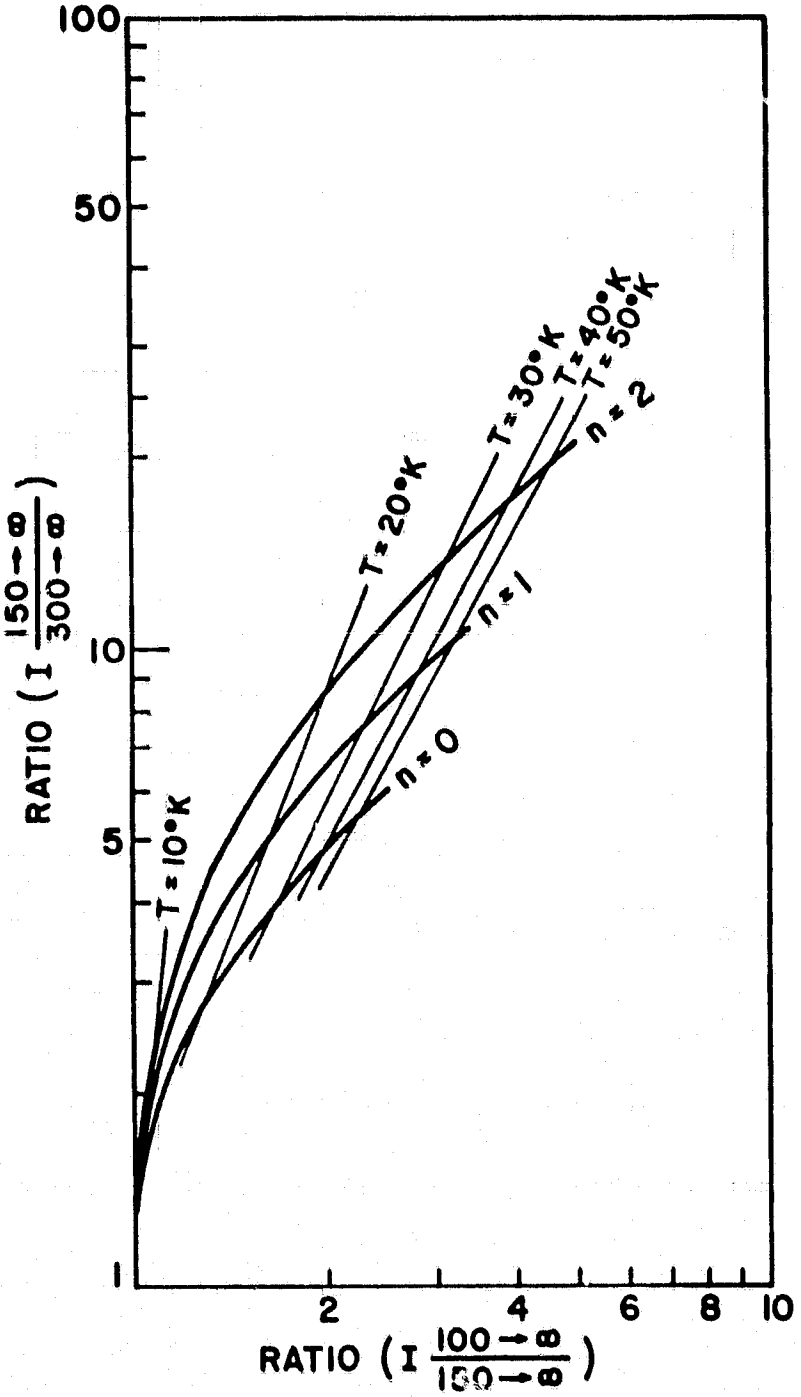
100
50
10
5
1
2
4
6
8
10
RATIO ($I\frac{150\rightarrow 8}{300\rightarrow 8}$)
RATIO ($I\frac{100\rightarrow 8}{150\rightarrow 8}$)
T=10°K
T=20°K
T=30°K
T=40°K
T=50°K
n=0
n=1
n=2

FIGURE A1

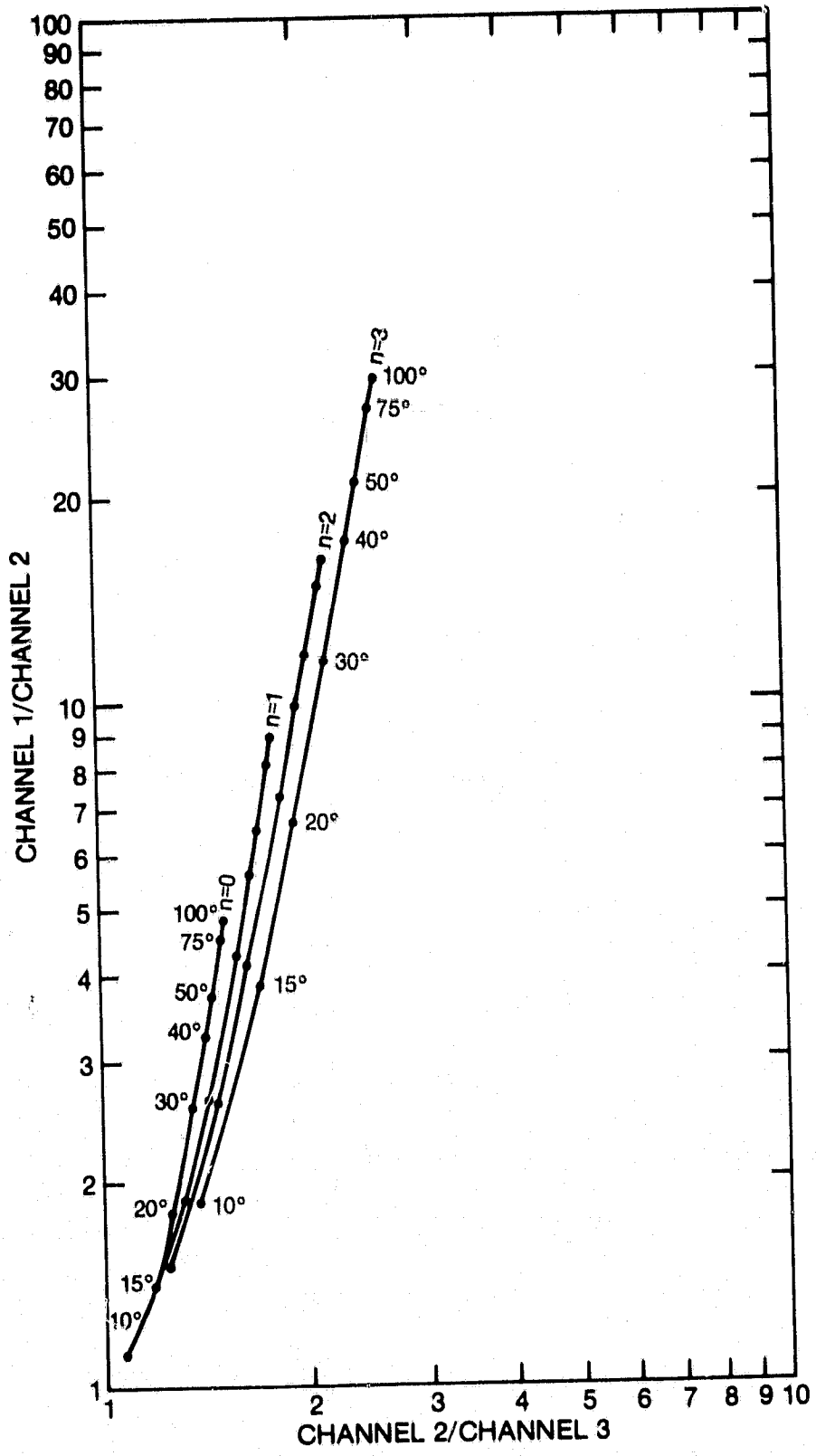
CHANNEL 1/CHANNEL 2
CHANNEL 2/CHANNEL 3
100
90
80
70
60
50
40
30
20
10
9
8
7
6
5
4
3
2
1
1
2
3
4
5
6
7
8
9
10
n=2
100°
75°
50°
40°
30°
20°
15°
n=1
100°
75°
50°
40°
30°
20°
10°
n=0
100°
75°
50°
40°
30°
20°
15°
10°

FIGURE A2

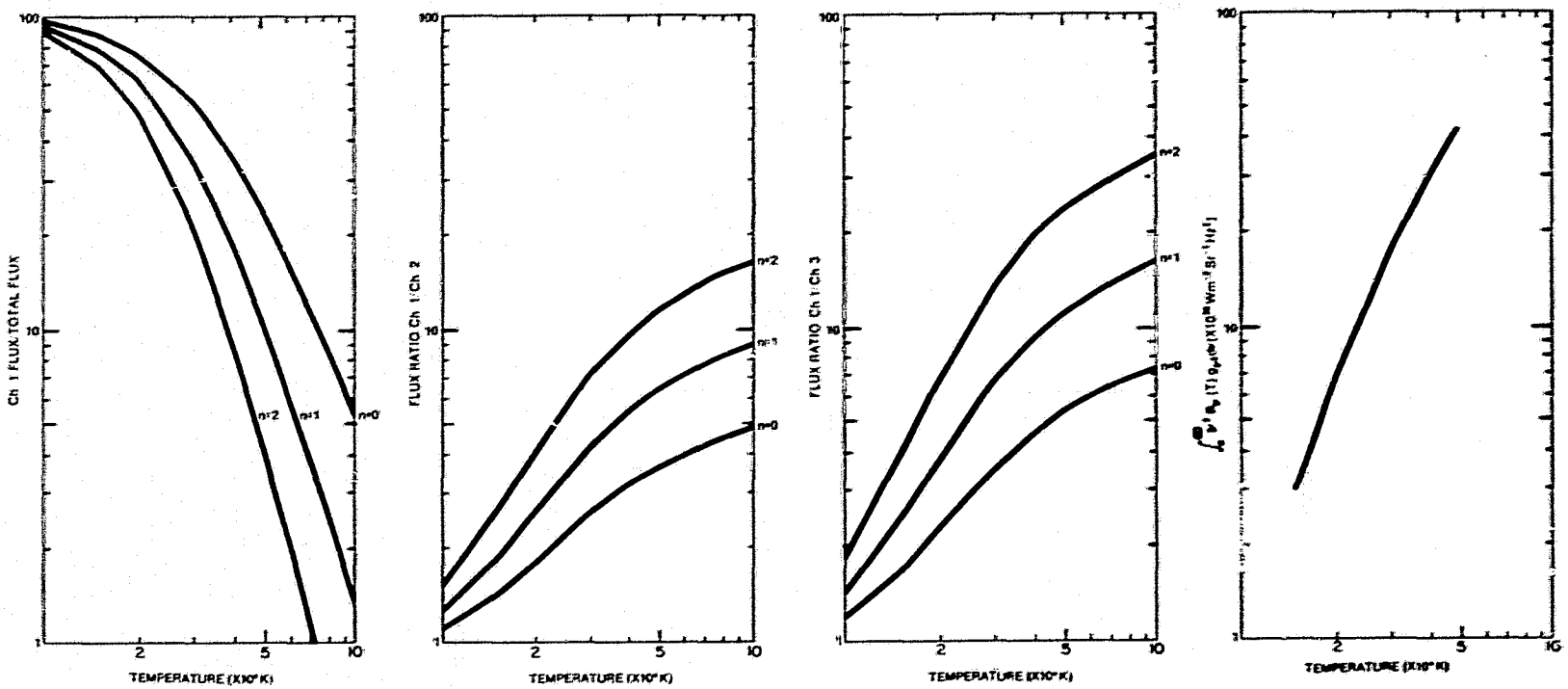
Ch 1 FLUX/TOTAL FLUX
TEMPERATURE (X10³ K)
n=2
n=1
n=0
FLUX RATIO Ch 1/Ch 2
TEMPERATURE (X10³ K)
FLUX RATIO Ch 1/Ch 3
TEMPERATURE (X10³ K)
TEMPERATURE (X10³ K)

FIGURE A3

APPENDIX B EVALUATION OF INTEGRALS OF PLANCK'S FUNCTION

In modelling the thermal emission using the submillimeter observational data, the integrals of various forms of Planck's function are frequently needed. In this section, I present a few numerical expressions, formulae, and tables that are useful for analysis pertinent to our submillimeter survey. I denote Planck's function by $B_\nu(T)$ in units of w m^{-2} sr^{-1} Hz^{-1} and the normalized spectral response of our photometer by g_ν.

$$x = h\nu/kT \tag{B1}$$

$$D_n = \int x^n/(e^x-1)\, g(x)\, dx \tag{B2}$$

$$\int B_\nu(T)\, g_\nu\, d\nu = 2.250 \times 10^1 \times (T/300)^4 \times D_3 \tag{B3}$$

$$\int \nu\, B_\nu(T)\, g_\nu\, d\nu = 1.406 \times 10^{14} \times (T/300)^5 \times D_4 \tag{B4}$$

$$\int \nu^2\, B_\nu(T)\, g_\nu\, d\nu = 8.791 \times 10^{26} \times (T/300)^6 \times D_5 \tag{B5}$$

$$\begin{aligned} \langle\nu\rangle &= \int \nu\, B_\nu(T)\, g_\nu\, d\nu \,/\, \int B_\nu(T)\, g\nu \\ &= 6.249 \times 10^{12} \times (T/300) \times D_4 \,/\, D_3 \end{aligned} \tag{B6}$$

$$\begin{aligned} \langle\Delta\nu\rangle &= \int B_\nu(T)\, g_\nu\, d\nu \,/\, B_\nu \\ &= 6.249 \times 10^{12} \times (T/300) \times D_3 \,/(x^3/(e^x-1)) \end{aligned} \tag{B7}$$

To compute the integral D_n, the Gauss-Legendre Quadrature may be used :

$$
\begin{aligned}
Dn(a) &= \int_0^\infty x^n/(e^x-1)\ g(x)\ dx \\
&= \int_0^a x^n/(e^x-1)\ g(x)\ dx \\
&= a/2 \int_{-1}^{1} (a/2(y+1))^n/(e^{a/2(y+1)}-1)\ g(a/2(y+1))\ dy \\
&\approx a/2 \sum f(y_i)\ g'(y_i) \qquad\qquad (B8)
\end{aligned}
$$

where $a = hc/kT\lambda_a$, $\lambda_a < \lambda_{cut-on}$, and y_i denotes the ith node in the quadrature, $f(yi) = (a/2(y_i+1)^n/(e^{a/2(y_i+1)}-1)$, and $g'(y_i) = g(a/2(y_i+1))$. For our submillimeter photometer, the values of a for the three channels are given by :

$$
a = \begin{cases} 1.60 \times 10^2 / T & \\ 9.60 \times 10^1 / T & \text{for } \lambda_a \\ 7.20 \times 10^1 / T & \end{cases} \qquad \begin{matrix} 90\ \mu m \\ 150\ \mu m \\ 200\ \mu m \end{matrix}
$$

Note that for a low pass system, the choice of λ_a is immaterial as long as $\lambda_a < \lambda_{cut-on}$. Using this particular set of λ_a, $g'(y_i) = t(\lambda_i)$ = normalised transmission at wavelength λ_i, where $\lambda_i = 2\lambda_a / (1+y_i)$.

For the filter transmission functions g_ν that are shown in Figure 2.11, I find N = 6 provides a satisfactory answers even for a as large as 5. With N=6, the values of λ_i, the nodes and the weighs for the Gauss-Legendre Quadrature are given as follows:

y_i	w_i	λ_i (μm) Ch.1	Ch.2	Ch3.
0.23862	0.46791	145	242	323
-0.23862	0.46791	236	394	525
0.66121	0.36076	108	181	241
-0.66121	0.36076	531	886	1181
0.93247	0.17132	93	155	207
-0.93247	0.17132	2665	4442	5923

The value of the integral D_n may then be evaluated accurately with only a few steps with a programmable calculator or a microcomputer. For larger values of a or for higher accuracy, a few more terms in the sum would suffice. A listing of the various function $D_n(a)$ and their ratios for the three submillimeter channels evaluated with N=10 is shown in Table B1 and Table B2 respectively.

Table B1

Convolution Products of Spectral Response and $x^n/(e^x-1)$
Flight #1

	T(K)	a	D_3	D_4	D_5	D_6
CHANNEL	1					
	5.	28.8000	6.488	24.82	121.4	716.4
	10.	14.4000	6.245	23.00	107.0	596.3
	15.	9.6000	5.678	19.65	84.72	429.0
	20.	7.2000	4.952	15.70	60.43	265.6
	30.	4.8000	3.455	8.854	26.45	87.14
	40.	3.6000	2.322	4.850	11.55	29.85
	50.	2.8800	1.580	2.758	5.419	11.46
	75.	1.9200	0.6825	0.8349	1.132	1.638
	100.	1.4400	0.3463	0.3246	0.3351	0.3675
	125.	1.1520	0.1977	0.1500	0.1249	0.1102
	150.	0.9600	0.1229	0.7826E-01	0.5458E-01	0.4028E-01
	175.	0.8229	0.8137E-01	0.4465E-01	0.2678E-01	0.1698E-01
	300.	0.4800	0.1829E-01	0.5923E-02	0.2089E-02	0.7773E-03
	600.	0.2400	0.2488E-02	0.4061E-03	0.7199E-04	0.1344E-04
CHANNEL	2					
	5.	19.2020	6.468	24.58	118.5	682.0
	10.	9.6010	5.567	18.23	71.61	319.8
	15.	6.4007	4.005	10.58	32.48	110.7
	20.	4.8005	2.741	5.927	14.65	39.77
	30.	3.2003	1.334	2.079	3.647	6.947
	40.	2.4002	0.7208	0.8717	1.178	1.721
	50.	1.9202	0.4272	0.4212	0.4622	0.5467
	75.	1.2801	0.1533	0.1031	0.7681E-01	0.6145E-01
	100.	0.9601	0.7101E-01	0.3621E-01	0.2040E-01	0.1232E-01
	125.	0.7681	0.3843E-01	0.1577E-01	0.7142E-02	0.3465E-02
	150.	0.6401	0.2307E-01	0.7922E-02	0.2998E-02	0.1215E-02
	175.	0.5486	0.1491E-01	0.4401E-02	0.1431E-02	0.4978E-03
	300.	0.3200	0.3156E-02	0.5471E-03	0.1043E-03	0.2125E-04
	600.	0.1600	0.4125E-03	0.3591E-04	0.3434E-05	0.3509E-06
CHANNEL	3					
	5.	14.4020	6.442	24.31	115.6	651.5
	10.	7.2010	5.163	15.84	57.15	230.1
	15.	4.8007	3.394	8.055	21.81	64.62
	20.	3.6005	2.175	4.131	8.833	20.51
	30.	2.4003	0.9794	1.314	1.960	3.152
	40.	1.8003	0.5076	0.5238	0.5981	0.7338
	50.	1.4402	0.2935	0.2457	0.2270	0.2249
	75.	0.9601	0.1019	0.5789E-01	0.3814E-01	0.2415E-01
	100.	0.7201	0.4647E-01	0.1996E-01	0.9406E-02	0.4739E-02
	125.	0.5761	0.2492E-01	0.8601E-02	0.3255E-02	0.1316E-02
	150.	0.4801	0.1486E-01	0.4289E-02	0.1356E-02	0.4578E-03
	175.	0.4115	0.9566E-02	0.2371E-02	0.6435E-03	0.1865E-03
	300.	0.2400	0.2003E-02	0.2911E-03	0.4628E-04	0.7851E-05
	600.	0.1200	0.2599E-03	0.1895E-04	0.1511E-05	0.1284E-06

Table B2
Ratios of Convolution Products
Flight # 1

T(K)	R_1	R_2	R_3	R_4
Channel 1 : Channel 2				
5.	1.0031	1.0095	1.0245	1.0504
10.	1.1217	1.2617	1.4938	1.8646
15.	1.4177	1.8578	2.6085	3.8733
20.	1.8062	2.6487	4.1240	6.6787
30.	2.5888	4.2582	7.2513	12.5438
40.	3.2214	5.5636	9.8005	17.3472
50.	3.6987	6.5475	11.7224	20.9704
75.	4.4528	8.0971	14.7441	26.6601
100.	4.8763	8.9634	16.4286	29.8251
125.	5.1430	9.5073	17.4835	31.8039
150.	5.3253	9.8781	18.2017	33.1493
175.	5.4574	10.1464	18.7207	34.1205
300.	5.7935	10.8270	20.0345	36.5754
600.	6.0324	11.3091	20.9627	38.3061
Channel 2 : Channel 3				
5.	1.0041	1.0111	1.0245	1.0468
10.	1.0782	1.1506	1.2529	1.3895
15.	1.1800	1.3133	1.4894	1.7139
20.	1.2606	1.4347	1.6588	1.9395
30.	1.3625	1.5827	1.8607	2.2039
40.	1.4199	1.6641	1.9700	2.3454
50.	1.4556	1.7142	2.0367	2.4312
75.	1.5039	1.7812	2.1252	2.5445
100.	1.5281	1.8144	2.1688	2.6000
125.	1.5425	1.8341	2.1945	2.6326
150.	1.5520	1.8471	2.2115	2.6542
175.	1.5588	1.8563	2.2235	2.6694
300.	1.5756	1.8791	2.2531	2.7068
600.	1.5872	1.8948	2.2734	2.7324
Channel 1 : Channel 3				
5.	1.0072	1.0207	1.0496	1.0996
10.	1.2094	1.4518	1.8716	2.5909
15.	1.6729	2.4399	3.8850	6.6383
20.	2.2770	3.8000	6.8409	12.9532
30.	3.5272	6.7395	13.4926	27.6446
40.	4.5740	9.2586	19.3072	40.6855
50.	5.3838	11.2238	23.8750	50.9825
75.	6.6967	14.4227	31.3347	67.8366
100.	7.4513	16.2632	35.6299	77.5439
125.	7.9328	17.4370	38.3679	83.7284
150.	8.2648	18.2456	40.2528	87.9833
175.	8.5068	18.8347	41.6254	91.0802
300.	9.1280	20.3447	45.1398	99.0019
600.	9.5745	21.4279	47.6572	104.6685

REFERENCES

Aannestad, P. A., 1975, Ap. J., 200, 30.

Aannestad, P. A. and Purcell, E. M., 1973, Ann. Rev. of Astr. Ap., 11, 309.

Allen, C. W., 1973, Astrophysical Quantities (University of London Press).

Altenhoff, W. J., Downes, D., Goad, L., Maxwell, A., Reinhart, R., 1970, Astr. Ap. Suppl., 1, 319.

Altenhoff, W. J., Downes, D., Pauls, T., and Schraml, J., 1978, Astr. Ap. Suppl., 35, 23.

Armstrong, K., Harper, D. A., and Low, F. J., 1972, Ap. J., 178, L89.

Armstrong, K. R. and Low, F. J., 1973, Appl. Optics, 12, 2007.

Barlow, M. J. and Silk, J. J., 1976, Ap. J., 207, 131

Barraclough, D. R., Harwood, J. M., Leaton, B. R., and Malin, S. R. C., 1975, Roy. Astron. Soc., 43, 654.

Bohlin, R. C., Savage, B. D., Drake, J. F., 1978, Ap. J., 224, 132.

Born, M. and Wolf, E., 1970, Principles of Optics (Pergamon Press).

Boisse, P., Gispert, R., Coron, N., Wijnbergen, J., Serra, G., Ryter, C., and Puget, J. L., 1980, preprint.

Burton, W. B., and Shane, D. E., 1970, IAU Sym. No. 38, The Spiral Structure of our Galaxy, ed. W. Becker and G. Contopoulos (Dordrecht:Reidel), p.397.

Burton, W. B., 1976, Annual Review of Astron. Astrophys., 14, 277.

Burton, W. B., and Gordon, M. A., 1978, Astr. Ap., 63, 7.

Campbell, M. F., Hoffmann, W. F., Thronson, H. A., Harvey, P. M., 1980, Ap. J., 238, 122.

Cheung, L. H., Frogel, J. A., Gezari, D. Y., and Hauser, M. G., 1978, Ap. J., 226, L149.

Cheung, L. H., Frogel, J. A., Gezari, D. Y., and Hauser, M. G., 1980, Ap. J., 240, in press.

Churchwell, E., Mezger, P. G., and Huchtmeier, W., 1974, Astr. Ap., 32, 283.

Churchwell, E., Smith, L. F., Mathis, J., Mezger, P. G., and Huchtmeier, W., 1978, Astr. Ap., 70, 719.

Cohen, R. S., Dame, T. M., and Thaddeus, P., 1980a, B.A.A.S., 12, No.2, 482.

Cohen, R. S., Cong, H., Dame, T. M., and Thaddeus, P., 1980b, Ap. J., 239, L53.

Cohen, S. A., 1976, Nature, 261, 215.

Dame, T. M., Cohen, R. S., and Thaddeus, P., 1980, B.A.A.S., 12, No.2, 483.

Dickman, R. L., 1976, Ph. D. Thesis, Columbia University.

Drapatz, S., 1979, Astr. Ap., 75, 26.

Elias, J. H., Ennis, D. J., Gezari, D. Y., Hauser, M. G., Houck, J. R., Lo, K. Y., Matthews, K., Nadeau, D., Neugebauer, G., Werner, M. W., and Westbrook, W. E., 1978, Ap. J., 220, 25.

Emerson, J. P., Jennings, R. E., 1978, Astr. Ap., 69, 129.

Fazio, G. G., and Stecker, F. W., 1976, Ap. J., 207, L49.

Federman, S. R., Glassgold, A. E., and Kwan, J., 1979, Ap. J., 227, 466.

Furniss, I., Jennings, R. E., Moorwood, A. F. M., 1975, Ap. J., 202, 400.

Gatley, I., Becklin, E. E., Sellgren, K., and Werner, M. W., 1979, Ap. J., 233, 575.

Goldreich, P., and Kwan, J., 1974, Ap. J., 189, 441.

Goodman, F. D., 1978, Ap. J., 226, 87.

Gordon, M. A. and Burton, W. B., 1976, Ap. J., 208, 346.

Hanel, R. A., Conrath, B. J., Herath, L. W., Kunde, V. G., and Pirraglia, J. A., 1980, preprint.

Harper, D. A., Low, F. J., 1971, Ap. J., 165, L9.

Harper, D. A., Hildebrand, R. H., Stiening, R., and Winston, R., 1976, Appl. Optics., 15, 53.

Harper, D. A., Hildebrand, R. H., Keene, J., Lowenstein, R., Whitcomb, S. E., 1980, pre-published data.

Hart, L., and Pedler, A., 1976, M.N.R.A.S., 176, 547.

Harvey, P. M., Campbell, M. F., and Hoffmann, W. F., 1978, Ap. J., 219, 891.

Hauser, M. G., and Notarys, H., 1975, B.A.A.S., 7, 409.

Hazen, N. L., Coyle, L. M., and Diamond, S. M., 1974, Center for Astrophyics preprint No. 66.

Hildebrand, R. H., Whitcomb, S. E., Winston, R., Steining, R. F., Harper, D. A., and Moseley, S. H., 1977, Ap. J., 216, 698.

Hoffmann, W. F., 1972, Infrared Detection Technique for Space Research, ed. Manno, V., and Ring, J., pp. 41, (D. Reidel Co).

Hoffmann, W. F., Frederick, C. L., and Emery, R. J., 1971, Ap. J., 170, L89.

Hollenbach, D. J. and Salpeter, E. E., 1971, Ap. J., 163, 155.

Hollenbach, D. J., Werner, M. W., and Salpeter, 1971, Ap. J., 163, 165.

Jones, R. T., 1954 ,J. Opt. Soc. Ameri., 44, 630.

Knacke, R. F., and Thomson, R. K., 1973, P.A.S.P., 85, 341.

Kniffen, D. A., Fichtel, C. E., and Thompson, D. J., 1977, Ap. J., 215, 765.

Leung, C. M., and Lizst, H. S., 1976, Ap. J., 208, 732.

Leung, C. M., 1975, Ap. J., 199, 340.

Leung, C. M., 1976, Ap. J., 209, 75.

Lindblad, P. O., Grape, K., Sandqvist, Aa, and Schober, J., 1973, Astr. Ap., 24, 309.

Lockman, F. J., 1976, Ap. J., 209, 429.

Low, F. J., 1961, Opt. Soc. Am., 51, 1300.

Low, F. J., Kurtz, R. F., Poteet, W. M., and Nishimura, T., 1977, Ap. J., 214, L115.

Maihara, T., Oda, N., and Okuda, A., 1979, Ap. J., 227, L129.

Mathewson, D. S., Healy, J. R., Rome, J. M., 1962, Aust. J. Phys., 15, 369.

Mezger, P. G. and Henderson, A. P., 1967, Ap. J., 147, 471.

Mezger, P. G., Smith, L. F., and Churchwell, E., 1974, Astr. Ap., 32, 269.

Mezger, P. G., 1978, Astr. Ap., 70, 565.

Morris, M., and Lo, K. Y., 1978, Ap. J., 223, 803.

Nishimura, T., Low, F. J., and Kurtz, R. F., 1980, Ap. J., 239, L101.

Olthof, H., 1974, Astr. Ap., 33, 471.

Owens, D. K., Muehlner, D. J., and Weiss, R., 1979, Ap. J., 231, 702.

Panagia, N., 1973, A. J., 78, 929.

Panagia, N., and Smith, L. F., 1978, Astr. Ap., 62, 277.

Pipher, J. L., 1973, IAU Symp. 52, Interstellar Dust and Related Topics, ed. J. Greenberg and H. Van de Hulst (D. Reidel), p. 559.

Purcell, E. M., 1969, Ap. J., 158, 433.

Reifenstein III, E. C., Wilson, T. L., Burke, B. F., Mezger, P. G., and Altenhoff, W. J. 1970, Astr. Ap., 4, 357.

Richard, L. J., Palmer, P., Turner, B. E., Morris, M. and Zuckerman, B., 1977, Ap. J., 214, 390.

Rouan, D., Lena, P. J., Puget, J. L., and deBoer, K., Wijnbergen, J. J., 1977, Ap. J., 213, L35.

Ryter , C. E. and Puget, J. L., 1977, Ap. J., 215, 775.

Savage, B. D., Bohlin, R. C., Drake, J. F., Budich, W., 1977, Ap. J., 216, 291.

Serra, G., Puget, J. L., Ryter, C. E., and Wijnbergen, J. J., 1978, Ap. J., 222, L21.

Scoville, N. Z., and Solomon, P. M., 1974, Ap. J., 187, L67.

Scoville, N. Z., and Kwan, J., 1976, Ap. J., 206, 718.

Scoville, N. Z. and Solomon, P. M., 1975, Ap. J., 199, L105.

Shane, D. E., 1972, Astr. Ap., 16, 118.

Shaver, P. A., and Goss, W. M., 1970, Aust J. Phys. Suppl., 14, 133.

Silverberg, R. F., Hauser, M. G., Mather, J. C., Gezari, D. Y., Kelsall, T., and L. H. Cheung, 1979, SPIE Proc., 172, 149.

Simon, T., 1976, A. J., 81, 135.

Smith, R. G., Jones, F. E., and Chasmer, R. P., 1958, The Detection and Measurement of Infrared Radiation (Oxford University Press).

Solomon, P. M., Scoville, N. Z., and Sanders, D. B., 1979, Ap. J., 232, L89.

Stark, A. A., and Blitz, L., 1978, Ap. J., 225, L15.

Stecker, F. W., Solomon, P. M., Scoville, N. Z., and Ryter, C. E., 1975, Ap. J., 201, 90.

Stier, M. T., 1979, Ph. D. Thesis, Harvard University.

Telesco, C. M., and Harper, D. A., 1980, Ap. J., 235, 392.

Thronson, H. A. and Harper, D. A., 1979, Ap. J., 230, 133.

Traub, W. A., and Stier, M. T., 1976, Appl. Optics, 15, 364.

Tucker, K. D., Kutner, M. L., and Thaddeus, P., 1973, Ap. J., 186, L13.

Werner, M. W., and Salpeter, E. E., 1969, M.N.R.A.S., 145, 249.

Werner, M. W., Gatley, I., Harper, D. A., Becklin, E. E., Lowenstein, R. F., Telesco, C. M., and Thronson, H. A., 1976, Ap. J., 204, 420.

Westbrook, W. E., Werner, M. W., Elias, J. H., Gezari, D. Y., Hauser, M. G., Lo, K. Y., and Neugebauer, G., 1976, Ap. J., 209, 94.

Westerhout, G., 1958, Bull. Astron. Inst. Neth., 14, 215.

Westerhout, G., 1976, Maryland-Bonn Galactic 21-cm Line Survey, University of Maryland.

Wilson, T. L., 1972, Astr. Ap., 19, 354.

Wilson, T. L., 1974, Astr. Ap., 31, 83.

Wright, E. L., 1976, Ap. J., 210, 250.

Zuckerman, B., Evans, N. J., 1974, Ap. J., 192, L149.